2010

Observational studies of the structure, content and environment of intermediate and high-mass star-forming regions

Kim Daniel Arvidsson
Iowa State University

Observational studies of the structure, content and environment of intermediate and high-mass star-forming regions

by

Kim Arvidsson

A dissertation submitted to the graduate faculty

in partial fulfillment of the requirements for the degree of

DOCTOR OF PHILOSOPHY

Major: Astrophysics

Program of Study Committee:
Charles Kerton, Major Professor
Steven Kawaler
Lee Anne Willson
Craig Ogilvie
Xiaoqing Wu

Iowa State University

Ames, Iowa

2010

TABLE OF CONTENTS

LIST OF TABLES

LIST OF FIGURES

ACKNOWLEDGEMENTS

I thank my advisor Charles Kerton for everything he has done. His guidance, enthusiasm, support and patience have truly been invaluable. I wish to thank my collaborators Michael Alexander, Chip Kobulnicky, Brian Uzpen and Tyler Foster for all their contributions. I would also like to thank the Department of Physics & Astronomy at Iowa State University for all the support through my graduate studies.

ABSTRACT

This thesis describes observational studies of star-forming regions and their influence on the interstellar medium. First, in an effort to understand the factors that govern the transition from low- to high-mass star formation, a sample of intermediate-mass star-forming regions (IM SFRs) is identified for the first time. IM SFRs constitute embedded clusters where stars up to — but not exceeding — ~ 8 $M_\odot$ are being produced. They are at an early evolutionary stage akin to compact H II regions, but they lack the massive ionizing central star(s). *IRAS* colors, *Spitzer Space Telescope* mid-IR images, millimeter continuum and ^{13}CO maps were used to compile a sample of 50 IM SFRs in the inner Galaxy. The photodissociation regions that demarcate IM SFRs have typical diameters of ~ 1 pc and luminosities of $\sim 10^4$ $L_\odot$, making them an order of magnitude less luminous than (ultra)compact H II regions. IM SFRs coincide with molecular clumps of mass $\sim 10^3$ $M_\odot$ which, in turn, lie within larger molecular clouds spanning the lower end of the giant molecular cloud mass range, $10^4 - 10^5$ $M_\odot$. The IR luminosity and associated molecular mass of IM SFRs are correlated, consistent with the known luminosity–mass relationship of compact H II regions. Peak mass column densities within IM SFRs are $\sim 0.1 - 0.5$ g cm^{-2}, a factor of several lower than ultra-compact H II regions, supporting the proposition that there is a threshold for massive star formation at ~ 1 g cm^{-2}.

Second, an investigation into the enormous H II region CTB 102 was carried out for the first time. Through a combination of new radio recombination line observations and available archival data, analysis shows that the filamentary structure surrounding the

central region is physically associated with the central region. The first ever distance estimate for this H II region is provided, 4.3 kpc. The overall morphology and size of CTB 102 indicates that it is likely a large H II region combined with a wind-blown interstellar bubble/chimney structure, powerful enough to disrupt the interstellar medium and clear out a $\sim 100 - 130$ pc region. The size and structure of CTB 102 makes it comparable to the W4 superbubble in the Perseus arm, one of the largest H II regions in the Galaxy.

Third, three halo H II regions, KR 7, KR 81 and KR 120, have been investigated using SCUBA 850 μm observations and molecular line observations as possible sites of triggered star formation. They were found to each have one dominant 850 μm source, corresponding to cold, dense material, located in the interface region between the H II region and the surrounding molecular material. They were also found to be less populated with sub-mm sources than the previously studied H II region of similar size, KR 140. The peak mass column density toward the sub-mm sources were found to be $0.1 - 0.3$ g cm^{-2}, comparable to IM SFRs. The masses found, 51, 27 and 21 M$_{\odot}$ fall within the range of masses previously found for KR 140. The same is true for the sizes found, 0.6, 0.4 and 0.2 pc. A possible embedded cluster of young stellar objects (YSOs) was found within the dominant sub-mm source of KR 120, consistent with earlier studies. This is likely a site for ongoing star formation. Candidates for embedded YSOs within the sub-mm sources were also found for KR 7, while sources toward KR 81 can be explained as either foreground or background objects.

CHAPTER 1. INTRODUCTION

Stars are invariably observed to form in molecular clouds. Within molecular clouds, stars appear to form from the densest structures within the molecular clouds, so-called "cores". Being formed in such dense environments, the process of stellar birth is hidden from astronomical observatories operating in the visual (optical) regime of the electromagnetic spectrum. This is because dust and dense gas surrounding the sites of star formation very efficiently absorbs and scatters visual light emitted in the process. However, by conducting observations in the infrared, sub-mm and radio regimes of the spectrum, these elusive objects can be studied.

Starting from a pre-existing molecular cloud, cold, dense molecular cores or filaments form within parts of the molecular cloud called "clumps". The cores have characteristic densities of 10^5 cm^{-3} and temperatures of 10–15 K. Several competing models exist for the formation mechanism of these cores, involving turbulence, shocks and magnetic fields (see Zinnecker & Yorke, 2007). Within the cores, gravitational collapse sets in and the densest parts collapse until the gas becomes optically thick which increases the gas pressure and proto-stellar objects form. The proto-stellar objects continue to accrete material (often through the formation of disks), causing the proto-stellar objects to grow in mass and contract as they evolve toward the main sequence. Eventually, hydrogen-burning temperatures and densities are reached. The natal cloud is disrupted by stars that are in the process of forming or by newly formed stars through winds, outflows and radiation.

Star formation is a process that spans many orders of magnitude in length, mass, density and many other important physical parameters. Particularly, high-mass star formation, i.e., the formation of stars where the most massive star formed is considered a high-mass star ($M > 8$ M$_\odot$) appears to require some fundamentally different conditions and physical processes compared to low-mass star formation, i.e., the formation of stars where the most massive star formed is a low-mass star ($M < 2$ M$_\odot$). This affects all the before mentioned general steps in the star formation process. Consider a spherical, homogeneous and isolated cloud of density n and temperature T with no macroscopic motions. It is unstable if its mass M is greater than the critical Jeans mass M_J (Lequeux, 2005, eq. 14.15)

$$M > M_J \approx 1.4 \left(\frac{T}{10\ \mathrm{K}}\right)^{3/2} \left(\frac{n}{10^4\ \mathrm{cm}^{-3}}\right)^{-1/2} \mathrm{M}_\odot \tag{1.1}$$

where the numerical factor is very approximate. During an isothermal gravitational collapse, as n increases, M_J decreases, which leads to fragmentation of the cloud into smaller collapsing sub-clouds. Such fragmentation favors the formation of low-mass stars. Though this is an idealized picture, it illustrates one of the issues regarding massive star formation through accretion. It has previously been considered difficult for high-mass stars to form through accretion, since the intense radiation pressure from their central source halts the inflow of material. Furthermore, high-mass stars tend to form in dense clusters within Giant Molecular Clouds (GMCs; $10^4 - 10^6$ M$_\odot$), the most massive molecular structures in the Galaxy. Low-mass star formation takes place in relative isolation, in less dense environments and within less massive molecular clouds. This is the motivation for the idea of high-mass stars forming through merging of lower-mass stars. Recently however, observations of dense disks in two high-mass stellar systems adds to the mounting observational evidence that the accretion model is the more favored model for high-mass star formation (Whitney, 2005), but the origin of high-mass stars is still

an unsolved question in astrophysics (Zinnecker & Yorke, 2007; McKee & Ostriker, 2007; Lada & Lada, 2003; Shu et al., 1987).

Figure 1.1 shows the massive star-forming region W5, spanning about 600 pc (2000 light years). This star-forming complex illustrates the idea of "triggered" star formation (Elmegreen, 1998). Massive young stars compress cooler surrounding gas into dense knots which then gravitationally contract and form new stars. Several generations of massive stars can be present at different evolutionary stages at the same time. Stars of all masses, not only high-mass stars, form in W5 and other high-mass star forming regions, but high-mass stars dominate the influence on the surrounding material. The full star formation picture for W5 is very complex due to the interactions and feedbacks. In contrast, Figure 1.2 shows part of the ρ Ophiuchi cloud complex, one of the closest star-forming regions. The view spans about 1.5 pc (5 light years). Several newly formed low-mass stars can be seen in the image, while high-mass stars are absent. Large-scale triggered star formation is not observed for this region.

Given the obscured nature of star-forming regions, observation at wavelengths longer than optical wavelengths is needed to observe not only different modes of star formation, but also different evolutionary stages. Figure 1.1 and Figure 1.2 show examples of infrared observations. In that wavelength regime, thermal emission from intrinsically very red objects and thermal and line dust emission dominates. Going to longer wavelengths, in the sub-mm and mm wavelength regime, thermal emission from very cold and dense dust can be seen. At even longer wavelengths, in the radio band, thermal bremsstrahlung and recombination lines from hot ionized gas, as well as line emission from molecules, are observed.

This thesis is about observational studies of star-forming regions and their impact

on the interstellar medium in our own Galaxy. The Milky Way offers unparalleled opportunities to study the birth of stars in great detail. In Chapter 2, *Bridging the gap – a sample of intermediate-mass star-forming regions in the inner Galaxy*, the first high resolution study of intermediate-mass star-forming regions is described. Intermediate-mass star-forming regions are regions that fall between the cases shown in Figure 1.1 and Figure 1.2. Chapter 2 has been modified from a manuscript accepted for publication in The Astronomical Journal. Chapter 3, *CTB 102 – an enormous Galactic H II region*, describes the first detailed study of the H II region CTB 102, showing it to be one of the largest H II regions in the Galaxy. Chapter 3 has been modified from an article published in The Astrophysical Journal. Chapter 4, *Sub-mm and molecular views of Galactic halo H II regions*, focuses on sites of possibly triggered star formation around small Galactic H II regions. Chapter 4 has been modified from a manuscript intended for submission to The Astronomical Journal. Chapter 5 summarizes the thesis and describes future research directions.

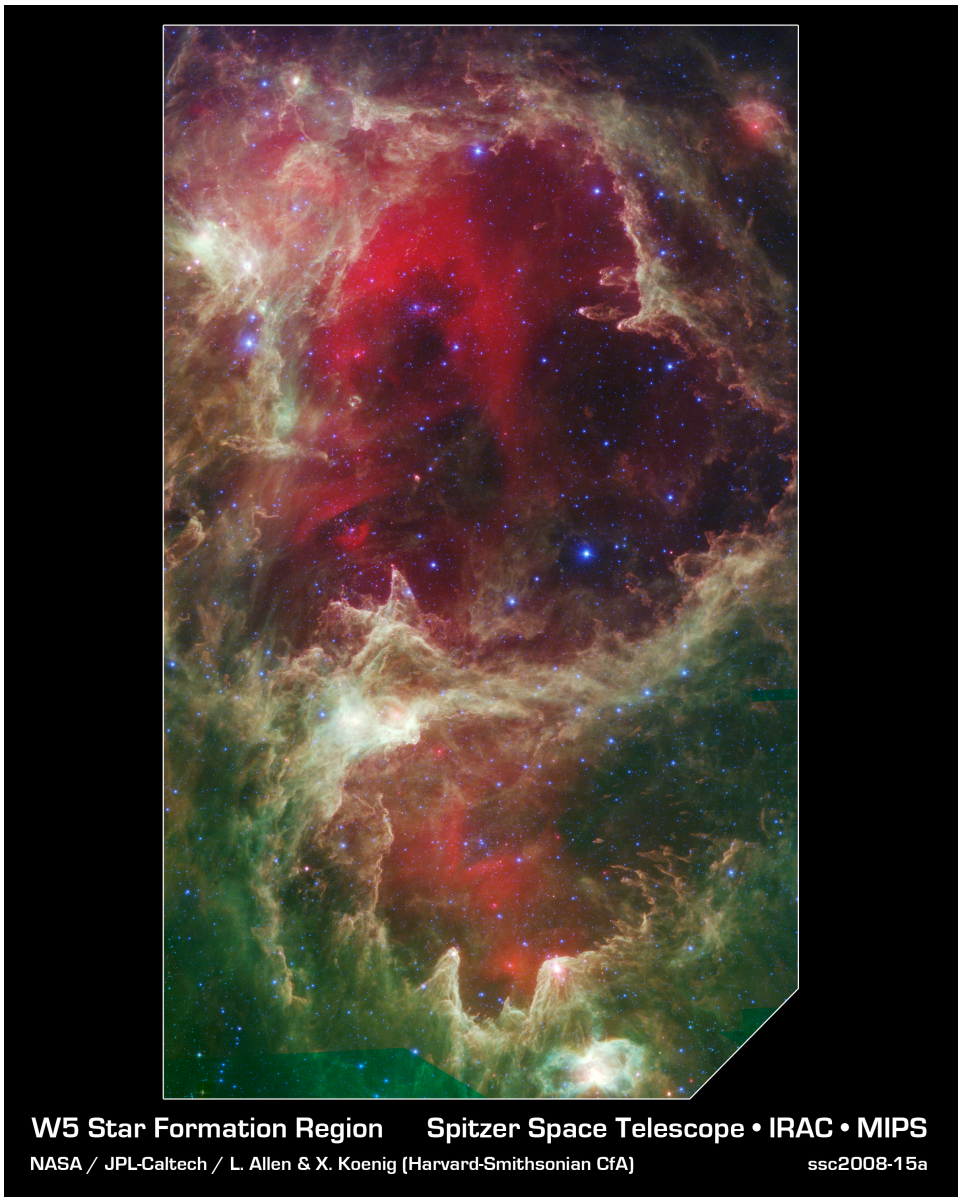

Figure 1.1 The massive star-forming region W5. Credit: Lori Allen, Xavier Koenig (Harvard-Smithsonian CfA) et al., JPL-Caltech, NASA.

Figure 1.2 Newly formed low-mass stars in the ρ Ophiuchi cloud complex. Credit: NASA JPL-Caltech, Harvard-Smithsonian CfA.

CHAPTER 2. BRIDGING THE GAP – A SAMPLE OF INTERMEDIATE-MASS STAR-FORMING REGIONS IN THE INNER GALAXY

2.1 Introduction

It has become clear that high-mass star formation cannot be viewed simply as a scaled-up version of the low-mass star formation paradigm (Zinnecker & Yorke, 2007). High-mass ($M > 8$ M$_\odot$) and low-mass ($M < 2$ M$_\odot$) star formation seem to require some fundamentally different conditions and physical processes that probably involve differences in turbulence and magnetic fields within their formative clouds as much as differences in cloud mass and density (Krumholz & McKee, 2005).

Stars forming in the 2 to 8 M$_\odot$ range (intermediate-mass; IM) are especially interesting as they straddle the boundary between the low- and high-mass paradigms and can provide a window into the processes that control or enable the transition from low- to high-mass star formation. Is it simply a question of an enhanced reservoir of material that promotes the formation of a more massive star, or is star formation shut off in some cases because of disruption of the parent molecular cloud? Is there evidence for induced or triggered star formation in the interstellar medium (ISM) surrounding IM star-forming regions (IM SFRs) as around massive SFRs (Deharveng et al., 2005)? How common are bipolar outflows? What is the ISM environment of these regions? Are IM

SFRs found in locations where high-mass star formation is also occurring or in relative isolation? What are the typical masses of IM star-forming clouds? What are the typical sizes and luminosities of IM SFRs?

Extensive studies of these IM SFRs, i.e., SFRs where the most massive star is IM, have not been possible in the past due to difficulties in clearly identifying the regions and the lack of angular resolution to investigate them in detail. The aim of this study, the first high-resolution study of IM SFRs, is to determine some basic properties of a carefully selected sample of IM SFRs. The candidate selection and classification criteria are presented in Section 2.2. In Section 2.3, CO features corresponding to the candidates are identified and a particularly interesting sub-sample of the candidates are discussed. The photometry and spectral energy distribution is examined in Section 2.4, and the molecular material is discussed in Section 2.5. The IM SFR sample is compared to Ultra-Compact H II (UCH II) regions in Section 2.6. Finally, a discussion is presented in Section 2.7 and conclusions are given in Section 2.8.

2.2 Infrared Analysis

2.2.1 Defining a Sample of Candidate IM SFRs

Kerton (2002), using 21 cm H I emission, identified a sample of IM SFRs and determined that they occupy a distinct region of the *IRAS* color-color diagram, see Figure 2.1 and Figure 12 in Kerton (2002). They are separate from H II regions, and quite distinct from T Tauri and Herbig AeBe stars (Barnes & Myers, 1993; Weintraub, 1990): $-0.18 < \log(F_\nu(25)/F_\nu(12)) < 0.40$, $0.96 < \log(F_\nu(60)/F_\nu(25)) < 1.56$ and $0.29 < \log(F_\nu(100)/F_\nu(60)) < 0.69$. These distinct colors arise from the combined effect of lowered dust temperatures surrounding IM stars and increased survivability of 12

μm-emitting grains in the less harsh radiation environment (Giard et al., 1994).

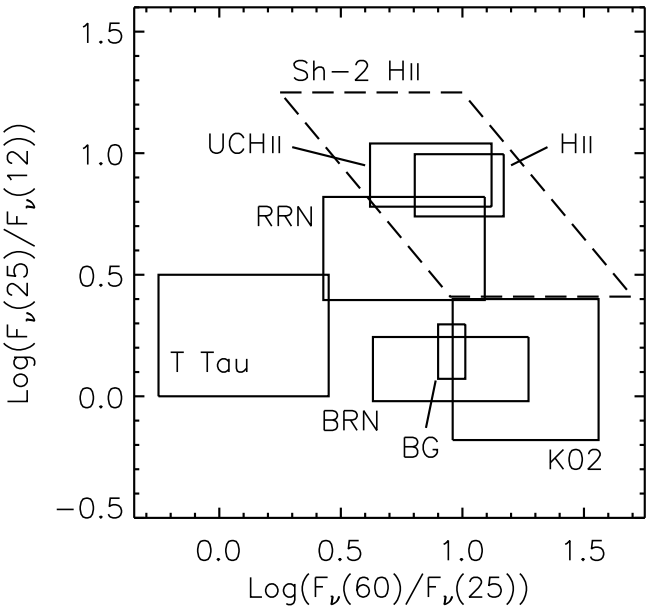

Figure 2.1 *IRAS* color-color diagram, indicating the extent of various astronomical objects adapted from Figure 13 in Kerton (2002). The box marked K02 corresponds to the color constraints in Section 2.2.1. The other boxes show: (Sh–2 H II) a majority of the H II regions compiled by Hughes & MacLeod (1989); (UCH II) ultra-compact H II regions from Wood & Churchwell (1989b); (H II) H II regions; (RRN) red reflection nebulae; (BRN) blue reflection nebulae; (BG) blue galaxies; (T Tau) T Tauri stars (all from Walker et al., 1989).

The *IRAS* Point Source Catalog v2.1 (PSC) was queried with the above color criteria. In all cases, the *IRAS* flux density quality was required to be marked as either high ($F_{\rm qual} = 3$) or moderate ($F_{\rm qual} = 2$). Table 2.1 lists the results of this query over several regions of interest. Over the entire sky there are 984 sources meeting these criteria. In the region within 1 degree ($|b| < 1^\circ$) of the Galactic plane where most star formation takes place, there are 360 sources. In this study, the focus is on the 70 sources at Galactic longitudes between $14^\circ < \ell < 55\overset{\circ}{.}7$ where complementary data from sev-

eral multiwavelength Galactic surveys are available, namely the The Boston University Five College Radio Astronomy Observatory (BU-FCRAO) Galactic Ring Survey (GRS; Jackson et al., 2006) in ^{13}CO, the mid-IR Galactic Legacy Infrared Mid-Plane Survey Extraordinaire (GLIMPSE; Benjamin et al., 2003), the Multiband Infrared Photometer for *Spitzer* Galactic survey (MIPSGAL; Carey et al., 2005) and the Bolocam Galactic Plane Survey (BGPS; Aguirre et al., 2009). Out of the 70 *IRAS* sources, 66 fall within the fully covered GRS field ($18° < \ell < 55.^{\circ}7$), and 4 objects fall within the partially covered part of the GRS ($14° < \ell < 18°$).

Table 2.1 Number of *IRAS* point sources for various regions satisfying the color criteria from Kerton (2002).

Region	Number of sources
All sky	984
Galactic plane ($\|b\| < 1°$)	360
GLIMPSE ($10° < \|\ell\| < 65°$, $\|b\| < 1°$)	178
GRS ($18° < \ell < 55.^{\circ}7$, $\|b\| < 1°$)	70

Use of the *IRAS* PSC to define the baseline sample of IM SFRs likely results in a small bias against very nearby sources which would have angular sizes larger than the *IRAS* beam. The *IRAS* PSC contains objects with angular sizes of less than $0.5'$, $0.5'$, $1'$, and $2'$ in the scan direction for 12, 25, 60 and 100 μm respectively. As will be shown in Section 2.3.2, IM SFRs have a typical diameter of ~ 1 pc. A 1 pc diameter source is larger than $2'$ in angular size for a distance < 1720 pc. There is an *IRAS* Small Scale Structure Catalog (SSSC) which contains information on structures up to $8'$ in angular extent. A search of this catalog over the whole sky for the same color criteria (but without the flux density quality criteria) returned 25 sources. Most of them are outside of the GLIMPSE/GRS region and all but one have an associated *IRAS* point source. Thus, close IM SFRs could be missed by using the *IRAS* PSC, but a large population is likely not missing since that volume is small compared to the covered volume.

2.2.2 Infrared Morphological Classification with *Spitzer*

The 70 selected *IRAS* sources were investigated using images from the *Spitzer* GLIMPSE and MIPSGAL legacy surveys. The GLIMPSE images have $\sim 2''$ resolution and 5σ sensitivities of 0.2, 0.2, 0.4, and 0.4 mJy in the Infrared Array Camera (IRAC; Fazio et al., 2004) wavebands centered near 3.6, 4.5, 5.8, and 8.0 μm. For this study, the available $6''$ resolution (5σ sensitivity of 1.7 mJy) Multiband Infrared Photometer for *Spitzer* (MIPS; Rieke et al., 2004) 24 μm images from the MIPSGAL survey were used. These images provide a vast improvement in angular resolution over the arcminute-scale *IRAS* images previously available.

Based on the GLIMPSE and MIPSGAL images, the 70 sources were classified by eye into three broad classes: "Blobs/Shells", "Filamentary" and "Star-like". Blobs/Shells are characterized by apparent circular or elliptical morphology, predominantly in the 8.0 and 24 μm bands. Blobs are typically circular (or elliptical) regions of extended emission having similar morphologies at 8.0 and 24 μm, while shells are usually ring-shaped 8.0 μm features that spatially coincide with 24 μm extended emission. Filamentary objects usually are emitting regions that occupy a small part of a larger filamentary structure, like a bead on a string, see Figure 2.2 for an example of filamentary morphology. This class also includes emitting regions located where filaments intersect. Finally, objects were classified as star-like where the emission appear to come from one or more point sources in all bands. No extended emission is evident for these objects, see Figure 2.3 for an example. These star-like objects are not likely IM SFRs. A point source diameter of $2''$ or less corresponds to a physical size of < 0.02 pc at a distance of 2 kpc, and a such physical size is much less than the expected size of IM SFRs.

Out of the 70 surveyed *IRAS* objects, 49 (70%) were classified as blobs/shells, 11 (16%) as filamentary and 10 (14%) as star-like. Figure 2.4 shows their distribution in *IRAS* color-color space and the three groups show no grouping or preferential location. The *IRAS* names and positions for the filamentary and star-like objects are listed in Table 2.2. The 49 blobs/shells were investigated in more detail, as their morphology is most consistent with the expected morphology of an IM SFR. Table 2.3 lists the *IRAS* names, positions (ℓ and b), angular diameters (θ) in arcminutes, velocity associations and widths ($V_{\rm LSR}$ and ΔV, discussed in Section 2.3), calculated near and far distances ($d_{\rm near}$ and $d_{\rm far}$), adopted distances, flags noting what distance was adopted, and the calculated diameter in pc of the blobs and shells. Table 2.3 contains 50 entries because one of them, *IRAS* 19012+0505, has been divided into two sources (North and South), that have slightly different velocity associations.

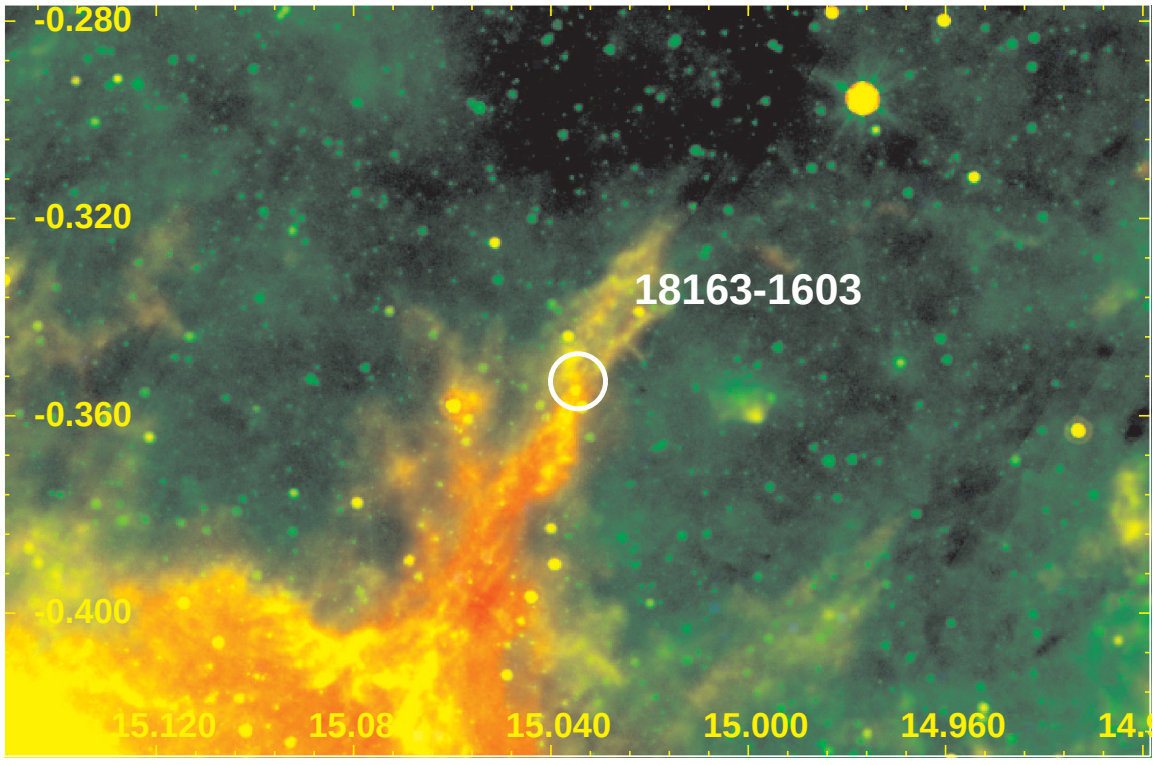

Figure 2.2 *IRAS* 18163-1603, an object classified as a filament.

Table 2.2 Filamentary and star-like objects.

IRAS name	ℓ (°)	b (°)	Class[a]
18163-1603	15.03450	−0.35301	F
18169-1338	17.23340	0.68040	F
18227-1218	19.07937	0.06120	F
18257-1226	19.30243	−0.65138	S
18279-1039	21.12765	−0.28842	F
18317-0926	22.63746	−0.54983	S
18328-0900	23.14221	−0.58687	S
18318-0741	24.20073	0.25168	S
18416-0518	27.43590	−0.81472	S
18465-0018	32.44363	0.39727	S
18559+0308	36.58437	−0.09614	S
18571+0326	36.99180	−0.22897	F
18550+0358	37.22322	0.47883	F
18588+0350	37.54749	−0.40816	S
19040+0616	40.30611	−0.43082	F
19079+0919	43.45117	0.11756	F
19137+1013	44.92225	−0.71903	F
19150+1116	45.98566	−0.50465	S
19152+1209	46.80001	−0.12841	F
19273+1637	52.11558	−0.57587	S
19300+1852	54.38650	−0.03721	F

[a]Filamentary objects are denoted with a "F", star-like objects with a "S".

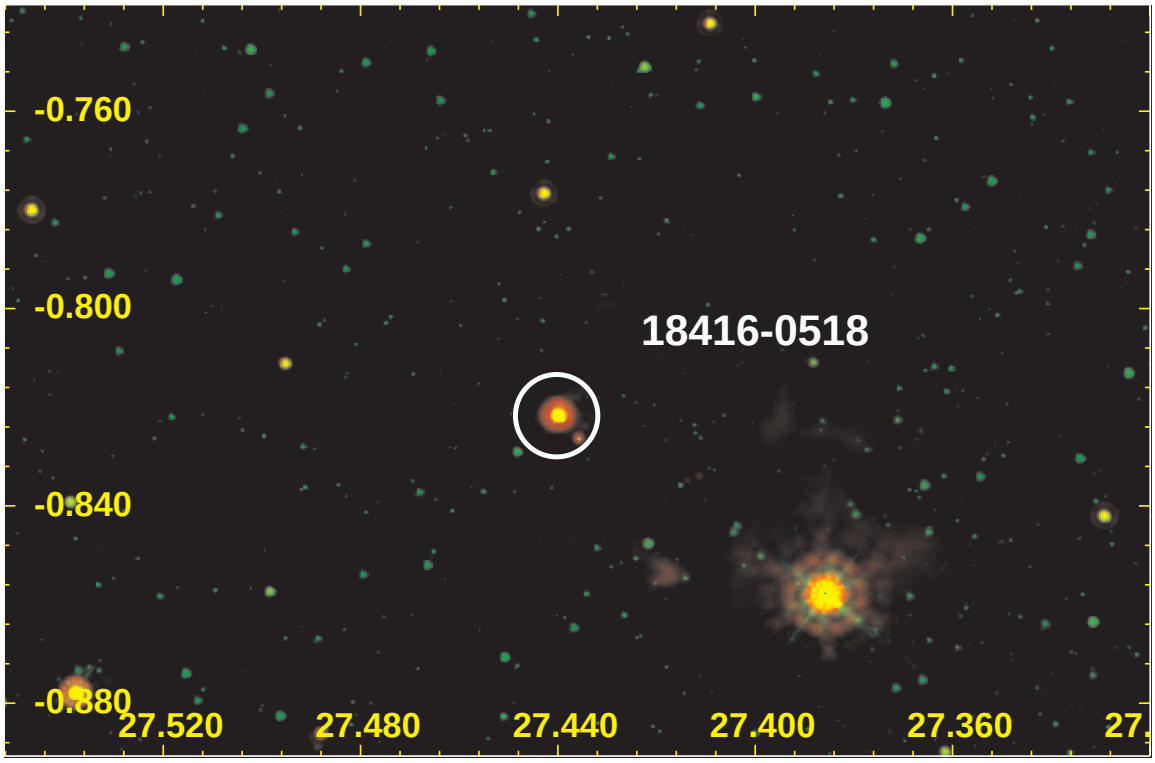

Figure 2.3 *IRAS* 18416-0518, an object classified as star-like.

2.3 Molecular Counterparts and Distances

2.3.1 CO Associations

The GRS ^{13}CO spectral data cubes were visually examined toward the regions of interest, the 49 objects classified as "Blobs/Shells". This ^{13}CO molecular line survey has a spectral resolution of 0.2 km s^{-1}, an angular resolution of 46″, and a sensitivity of $\leq$ 0.4 K. Molecular features similar in morphology to the mid-IR blobs and shells were searched for. The majority, 41 objects, have unambiguous ^{13}CO associations, i.e., either a single ^{13}CO spectral peak matches the candidate IM SFR, or if multiple peaks appear along the line of sight, the ^{13}CO morphology for a particular peak can be matched to the mid-IR feature. The width of the morphologically matched feature in each GRS

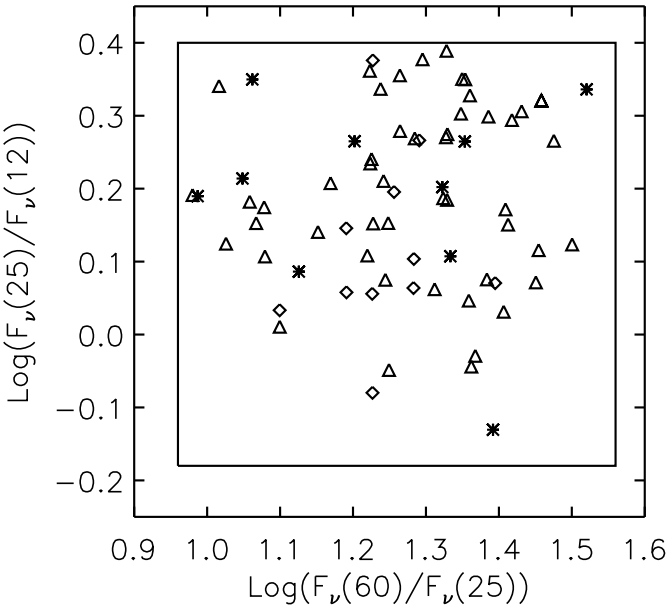

Figure 2.4 Enlarged portion of the *IRAS* color-color diagram. The drawn box corresponds to K02 in Figure 2.1, with the *IRAS* colors of the 70 objects plotted. Triangles correspond to "Blobs/Shells", diamonds to "Filamentary" and stars to "Star-like" objects. The three classes of objects show no grouping or preferential location in the *IRAS* color-color diagram.

Table 2.3 Properties of the objects classified as blobs or shells.

IRAS name	ℓ ($^\circ$)	b ($^\circ$)	θ ($'$)	$V_{\rm LSR}$ (km s^{-1})	ΔV (km s^{-1})	$d_{\rm near}$ (kpc)	$d_{\rm far}$ (kpc)	Adopted (kpc)	Flag	Diameter (pc)	$L_{\rm IR}$ (10^3 L$_\odot$)	$M_{\rm LTE}$ (M$_\odot$)
18131-1606	14.63111	0.30075	1.0	26.1	8.2	2.9	13.6	2.9	N	0.8	10.7	500
18180-1342	17.31025	0.40066	2.0	19.7	3.7	2.0	14.2	2.0	N	1.2	4.9	40
18241-1320	18.32426	−0.73709	0.6	43.3	4.4	3.7	12.5	3.7	N	0.6	1.2	800
18224-1228	18.88269	0.05205	1.5	49.9	9.3	4.0	12.1	4.0	N	1.7	36.5	6100
18253-1210	19.50327	−0.44381	1.0	63.1	5.0	4.6	11.4	4.6	N	1.3	6.0	2800
18322-0956	22.25764	−0.87999	0.6	41.0	2.6	3.2	12.5	3.2	N	0.6	4.6	200
18308-0741	24.09699	0.45326	1.8	94.7	8.2	5.9	9.6	···	U	3.1/5.0	27.7/73.3	4300/11500
18370-0607	26.19714	−0.18673	0.6	108.3	4.5	7.6	7.6	7.6	T	1.3	15.0	1700
18367-0529	26.71852	0.17412	0.5	···	···	···	···	···	A	···	···	···
18362-0517	26.83021	0.38216	2.2	···	···	···	···	···	A	···	···	···
18412-0440	27.96505	−0.44254	0.8	45.6	7.8	3.1	11.9	3.1	N	0.7	2.4	2300
18411-0312	29.24142	0.25972	0.5	···	···	···	···	···	A	···	···	···
18433-0327	29.28703	−0.33671	0.5	···	···	···	···	···	A	···	···	···
18441-0118	31.27801	0.48597	1.5	89.2	14.4	5.8	8.8	···	U	2.5/3.8	5.7/13.2	2100/4900
18463-0052	31.91297	0.19629	1.0	107.9	7.3	7.2	7.2	7.2	T	2.1	29.0	1600
18502-0018	32.86081	−0.41053	0.4	48.0	9.2	3.2	11.1	11.1	F	1.3	110.3	2600
18504+0025	33.53779	−0.12907	0.5	···	···	···	···	···	A	···	···	···
18537+0145	35.09790	−0.24120	0.5	51.6	7.6	3.4	10.6	···	U	0.5/1.5	4.4/42.9	100/900
18527+0203	35.26396	0.12033	1.0	···	···	···	···	···	A	···	···	···
18564+0145	35.41394	−0.84999	0.7	36.7	6.2	2.4	11.4	2.4	N	0.5	0.7	1000
19014+0451	38.75274	−0.52447	0.5	66.2	7.8	4.5	8.7	···	U	0.7/1.3	4.9/18.5	200/800
19012+0505-N	38.92659	−0.37007	1.8	39.8	6.7	2.6	10.6	2.6	N	1.4	10.7	700
19012+0505-S	38.92659	−0.37007	3.0	41.3	6.7	2.7	10.5	2.7	N	2.4	9.0	1400
19023+0545	39.64763	−0.29262	0.6	25.8	4.8	1.8	11.3	11.3	F	2.0	26.6	200
19023+0601	39.87238	−0.17333	1.3	57.3	12.4	3.8	9.2	3.8	N	1.4	8.0	200
19027+0656	40.74324	0.15801	0.5	16.9	8.8	1.3	11.6	11.6	F	1.7	17.1	3100
19060+0657	41.14428	−0.56201	2.2	···	···	···	···	···	A	···	···	···
19072+0649	41.14722	−0.88475	0.5	66.5	6.0	4.9	7.9	···	U	0.7/1.1	2.1/5.5	700/1700
19049+0712	41.22959	−0.19367	1.0	59.4	6.3	4.1	8.7	4.1	N	1.2	10.2	400
19062+0758	42.05222	−0.11977	1.2	70.3	6.9	5.6	7.1	5.6	N	2.0	3.8	1600
19105+0852	43.35147	−0.66408	0.6	58.0	6.3	4.2	8.2	···	U	0.7/1.4	3.3/12.5	500/1800
19056+0947	43.59957	0.85377	0.8	···	···	···	···	···	No CO	···	···	···
19139+1045	45.40416	−0.51347	1.1	60.9	11.1	4.9	7.0	4.9	N	1.6	9.2	300
19138+1055	45.53808	−0.39856	0.7	57.7	13.3	4.5	7.4	···	U	0.9/1.5	3.0/8.0	1000/2600
19157+1319	47.87449	0.31098	0.4	63.5	5.5	5.7	5.7	5.7	T	0.7	4.5	1400
19207+1329	48.60178	−0.66833	0.5	52.6	11.8	4.4	6.9	···	U	0.6/1.0	2.9/7.2	500/1200
19207+1348	48.87743	−0.51817	0.6	57.3	5.0	5.6	5.6	5.6	T	1.0	33.4	4300
19156+1441	49.07458	0.98102	0.4	53.1	4.7	4.5	6.6	···	U	0.5/0.8	0.8/1.7	300/600
19193+1443	49.53260	0.20918	0.5	63.1	5.5	5.5	5.5	5.5	T	0.8	4.2	600
19233+1413	49.54016	−0.88136	0.5	43.3	8.0	3.3	7.7	···	U	0.5/1.1	2.9/16.1	600/3200
19205+1447	49.72280	−0.01595	0.6	48.2	10.4	3.9	7.1	···	U	0.7/1.2	13.4/44.5	2000/6700
19221+1456	50.03463	−0.28204	1.8	61.8	10.4	5.5	5.5	5.5	T	2.9	16.3	1300
19214+1556	50.84320	0.33493	0.7	40.5	8.4	3.2	7.6	···	U	0.7/1.5	2.7/15.3	1000/5400
19255+1531	50.93431	−0.72378	0.6	38.6	5.1	3.0	7.7	···	U	0.5/1.3	2.2/14.3	300/1800
19256+1705	52.33394	0.00598	0.5	12.0	5.4	1.1	9.3	9.3	F	1.4	9.7	600
19248+1730	52.60285	0.37402	0.7	41.2	10.1	3.5	6.8	···	U	0.7/1.4	1.9/7.0	100/500
19247+1829	53.44999	0.87096	0.4	−2.6	4.4	0.3	9.9	9.9	F	1.2	6.9	1300
19260+1821	53.48407	0.52532	0.4	49.9	6.7	5.1	5.1	5.1	T	0.6	2.1	2000
19266+1926	54.51342	0.92616	0.6	32.4	7.1	2.7	7.1	···	U	0.5/1.2	2.5/17.5	400/2500
19330+1956	55.66724	−0.13004	0.5	31.6	5.6	2.8	6.9	6.9	F	1.0	10.2	900

^{13}CO spectrum defines a velocity range that were used to construct the zeroth-moment map from the GRS spectral cubes. As a check of the morphological association between ^{13}CO and the candidate IM SFR, the candidate was required to be spatially associated with a local maximum in the GRS zeroth-moment map. Of the remaining eight objects, seven have several possible associations in the data cube, resulting in an ambiguous radial velocity. These are labeled with the flag "A" in Table 2.3. The single remaining candidate, *IRAS* 19056+0947, was found to have no ^{13}CO association at all within a radius of 0.°3. This object is labeled with the flag "No CO" and could be a reflection nebula, a known contaminant (see Figure 2.1).

Figure 2.5 shows a compilation of the basic data for the candidate IM SFR *IRAS* 18131-1606. The top left panel is an UKIRT Infrared Deep Sky Survey (UKIDSS; Warren et al., 2007) K-band image. The top right panel is an RGB composite of *Spitzer* MIPS 24 μm (red), *Spitzer* IRAC 8.0 μm (green), and BGPS 1.1 mm continuum (blue) images. *Spitzer* 8.0 μm reveals the presence of polycyclic aromatic hydrocarbons (PAHs) and *Spitzer* 24 μm indicates the presence of hot dust. The BGPS is a 1.1 mm continuum survey of the Galactic plane with an effective resolution of 33″ and a non-uniform 1σ noise level in the range of 30 to 60 mJy beam^{-1}. The BGPS shows thermal dust emission from cold, dense material. The guiding circle shown has the same position in both panels and is the same angular size (in this case the aperture radius is 54″, from Table 2.4) as the aperture used to do photometry (Section 2.4). The contour levels in both top panels show integrated ^{13}CO intensity in the zeroth-moment map, in steps of 10%, from 90% to 10% of the peak (in this case $I_{\rm peak}$ = 28.5 K km s^{-1}, from Table 2.5). The bottom right panel shows the spatially averaged GRS 1-D ^{13}CO spectrum, where the shaded area corresponds to the velocity range used to make the zeroth-moment map (ΔV from Table 2.3). The bottom left panel shows the spectral energy distribution (SED, described further in Section 2.4) between 3.6–100 μm, where *Spitzer* IRAC and

MIPS 24 μm flux densities are displayed as diamonds, and *IRAS* PSC flux densities are displayed as squares.

2.3.2 Distances and Sizes

The LSR velocity ($V_{\rm LSR}$) of each candidate IM SFR was estimated by measuring the peak of the ^{13}CO feature in a 1-D spectrum produced by averaging the GRS cube of each candidate IM SFR over the area of the mid-IR feature, typically a region covering 4–16 GRS pixels (1 GRS pixel = $22'' \times 22''$). The results are shown in Table 2.3. Once the velocities were known, corresponding near and far kinematic distances were obtained. The Galactic rotation curve from Clemens (1985), assuming $R_0 = 8.5$ kpc, $V_0 = 220$ km s^{-1} was used to obtain the kinematic distances. The more recent rotation curve of Levine et al. (2008) yielded very similar distances for the same R_0 and V_0. Exceptions were when $\ell \geq 45^\circ$ and $V_{\rm LSR} \leq 50$ km s^{-1}, then the differences between the distances obtained with the two different rotation curves can be 0.3 kpc or more.

The angular diameters were determined by eye using the 8 and 24 μm images. Typically the diameter roughly corresponds to where the mid-IR surface brightness falls to $5\% - 25\%$ of the peak surface brightness. However, the varying background levels and irregular shapes make a quantitative angular size estimate imprecise. This technique has an estimated uncertainty of $\sim 20\%$. The angular diameter of *all* 50 blobs and shells are found in the range from $0.3'$ to $3.0'$, with a median angular diameter of $0.7'$ and an average of $0.9'$.

The available kinematic distances from the ^{13}CO associations are used to convert the angular diameters into (near and far) physical diameters, given in Table 2.3. To attempt to break the near/far distance ambiguity, eight objects among the blobs/shells that are

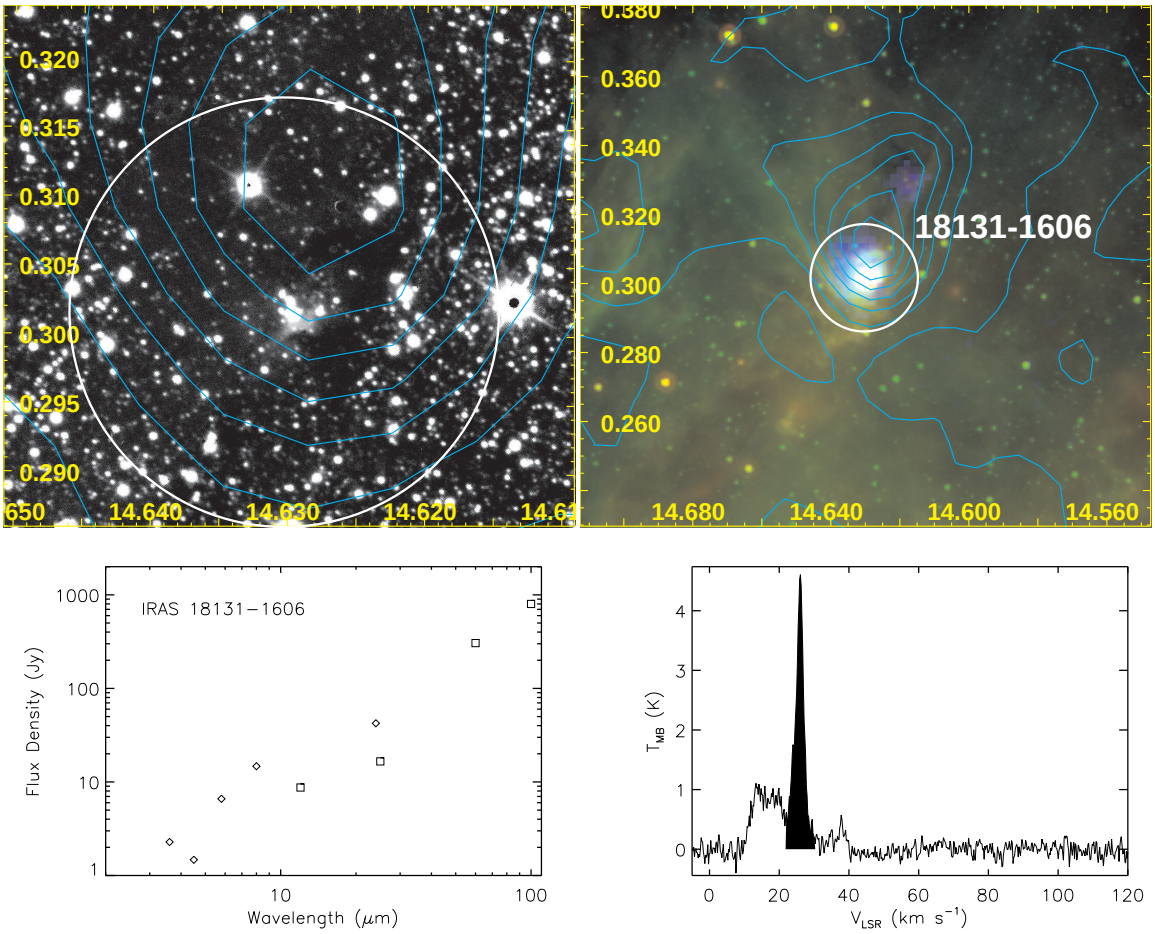

Figure 2.5 Four views of *IRAS* 18131-1606. (Top left) UKIDSS K-band image. (Top right) RGB composite of *Spitzer* MIPS 24 μm (red), *Spitzer* IRAC 8.0 μm (green), and BGPS 1.1 mm continuum (blue) images. The guiding circle shown in the two top panels has the same position and angular size and corresponds to the aperture radius of 54″ in Table 2.4. The contour levels in both top panels show integrated ^{13}CO intensity in the zeroth–moment map, in steps of 10%, from 90% to 10% of the peak (in this case $I_{\rm peak}$ = 28.5 K km s^{-1}, from Table 2.5). (Bottom left) Spectral energy distribution between 3.6–100 μm. *Spitzer* IRAC and MIPS 24 μm flux densities are displayed as diamonds. *IRAS* PSC flux densities are displayed as squares. (Bottom right) The spatially averaged GRS 1-D CO spectrum, where the shaded area corresponds to the velocity range used to make the zeroth-moment map (ΔV from Table 2.3). *IRAS* 18131-1606 falls within the partially covered GRS area. It is a 1′ blob at 8.0 and 24 μm, with a possible clustering of 2.2 μm point sources at the center. The blob is spatially associated with the source G014.634+00.308 from the BGPS source catalog (Rosolowsky et al., 2010). This BGPS source is clearly seen in blue.

highly likely to be located at the near distance were considered. Seven of them are clearly associated with ^{13}CO features that morphologically resemble local minima and/or dark lanes in the *Spitzer* 8.0 μm images. One of them (*IRAS* 18412-0440) is clearly associated with an infrared dark cloud (IRDC) as described in Simon et al. (2006). These are likely to be associated with molecular clouds at the near distance, seen in silhouette against the more distant diffuse Galactic emission. The eighth near object (*IRAS* 18180-1342) is on the outskirts of the molecular cloud associated with the Eagle Nebula (M16, NGC 6611). The Eagle Nebula has a photometric distance of 1.8 ± 0.5 kpc (Bonatto et al., 2006), putting *IRAS* 18180-1342 at the near distance. Multipanel images of these eight objects are shown as Figure 2.5 and Figures 2.7 to 2.13. Using the angular diameters and kinematic distances for these eight near objects, angular sizes were converted into physical diameters. Figure 2.6 shows a histogram of the distribution in physical diameter. The diameters range from 0.5 to 1.7 pc with most objects having a diameter less than 1 pc. The median value (solid line) is 0.8 pc and the average value (dashed line) is 0.9 pc. If instead these objects are considered to be at the far distance, the diameters would range from 2.2 to 8.3 with a median value of 3.0 pc and an average value of 3.8 pc. The diameter of ~ 1 pc for IM SFRs is consistent with various dusty and dust-free models for Photo Dissociation Regions (PDRs) (Diaz-Miller et al., 1998; Kerton, 2002).

The small range in physical size among the near distance objects, and the consistency with PDR models, enables assigning a likely distance to objects that cannot be determined to be at the near distance from clouds/dark lanes or association with sources with known distances. This "Standard Ruler" approach assigns objects to the near distance if they have near distance diameters ≥ 0.5 pc *and* far distance diameters > 2.0 pc. These 14 objects were designated with "N" in Table 2.3. Objects with near distance diameters < 0.5 pc *and* far distance diameters ≤ 2.0 pc were assigned to be at the far distance. These six objects were designated with "F". Objects at or above tangent point velocities

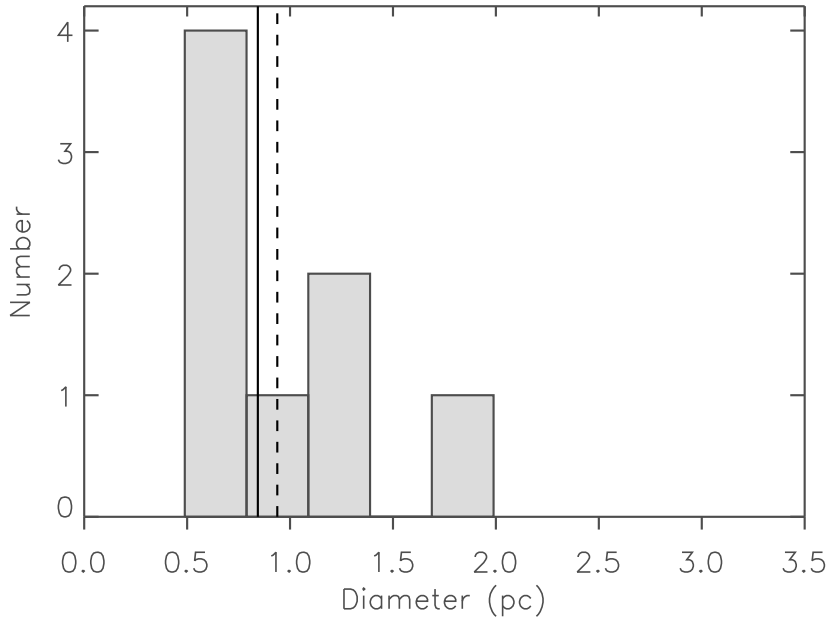

Figure 2.6 Histogram of diameters for the eight near IM SFRs. The solid line represents the median size (0.8 pc) while the dashed line represents the average size (0.9 pc). The bin size is 0.3 pc.

were assigned the tangent point distance and the corresponding diameter. These seven objects were designated with "T". *IRAS* 19012+0505-S was assigned to be near, due to its apparent connection to *IRAS* 19012+0505-N. Fifteen objects remain unassigned. Thirteen of them have both near and far diameters between 0.5 and 2.0 pc, and two objects have near and far diameters that exceed 2.0 pc. These objects were designated "U". Figure 2.14 shows the distribution of physical diameters for the 27 IM SFRs that have assigned distances in Table 2.3 (near, far, and tangent). The diameters range from 0.5 to 2.9 pc, with both median (solid line) and average (dashed line) values being 1.3 pc. If all the unassigned objects are assumed to be at the near distance, the median diameter drops to 1.0 pc, and the average drops to 1.2 pc. If instead all the unassigned objects were assumed to be at the far distance, the median diameter remains at 1.3 pc, and the average increases to 1.4 pc. Regardless of the choice of distances for the

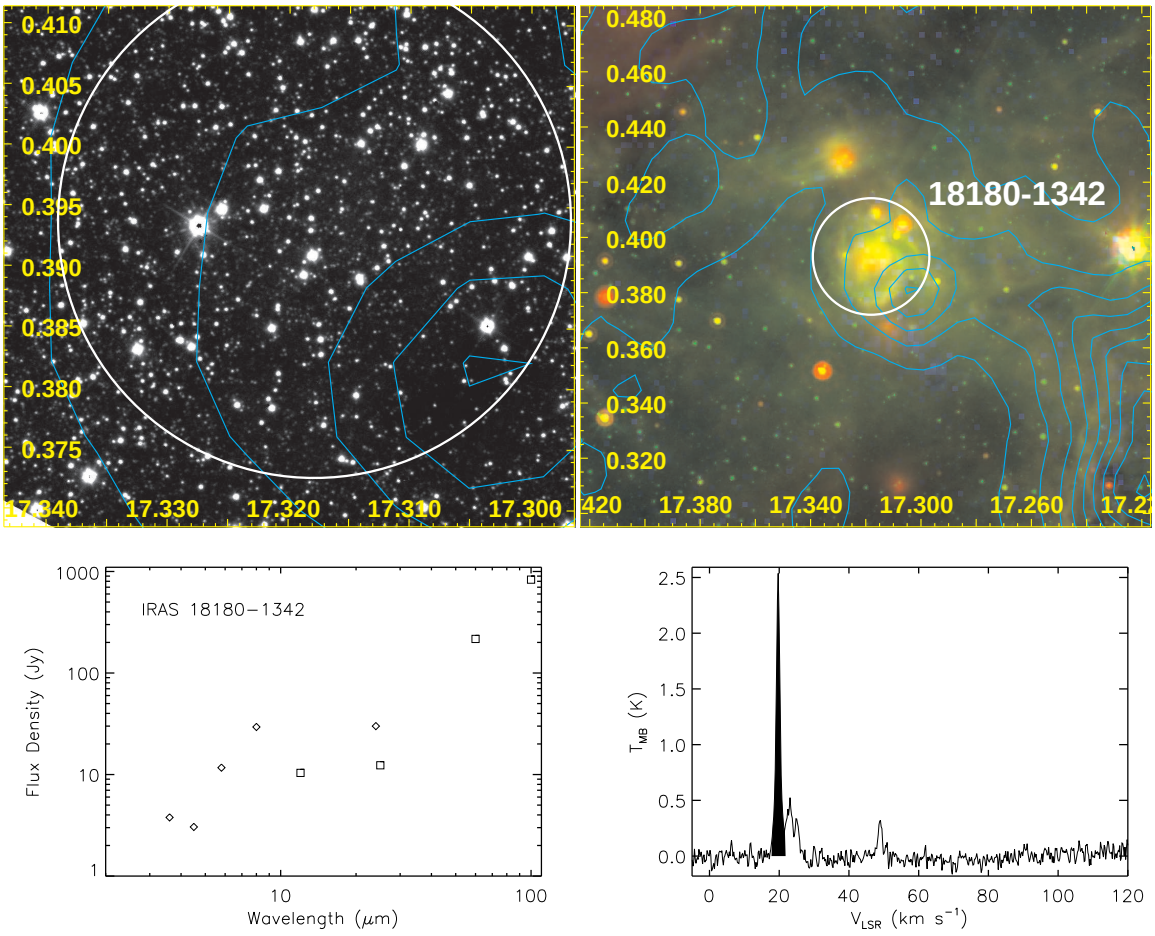

Figure 2.7 Four views of *IRAS* 18180-1342, like Figure 2.5. The guiding circle has a radius of 76″. This object also falls within the partially covered GRS area. The blob has an angular diameter of 2′, the largest apparent diameter of the near objects, but given its kinematic 2.0 kpc distance, it has a physical diameter of 1.2 pc.

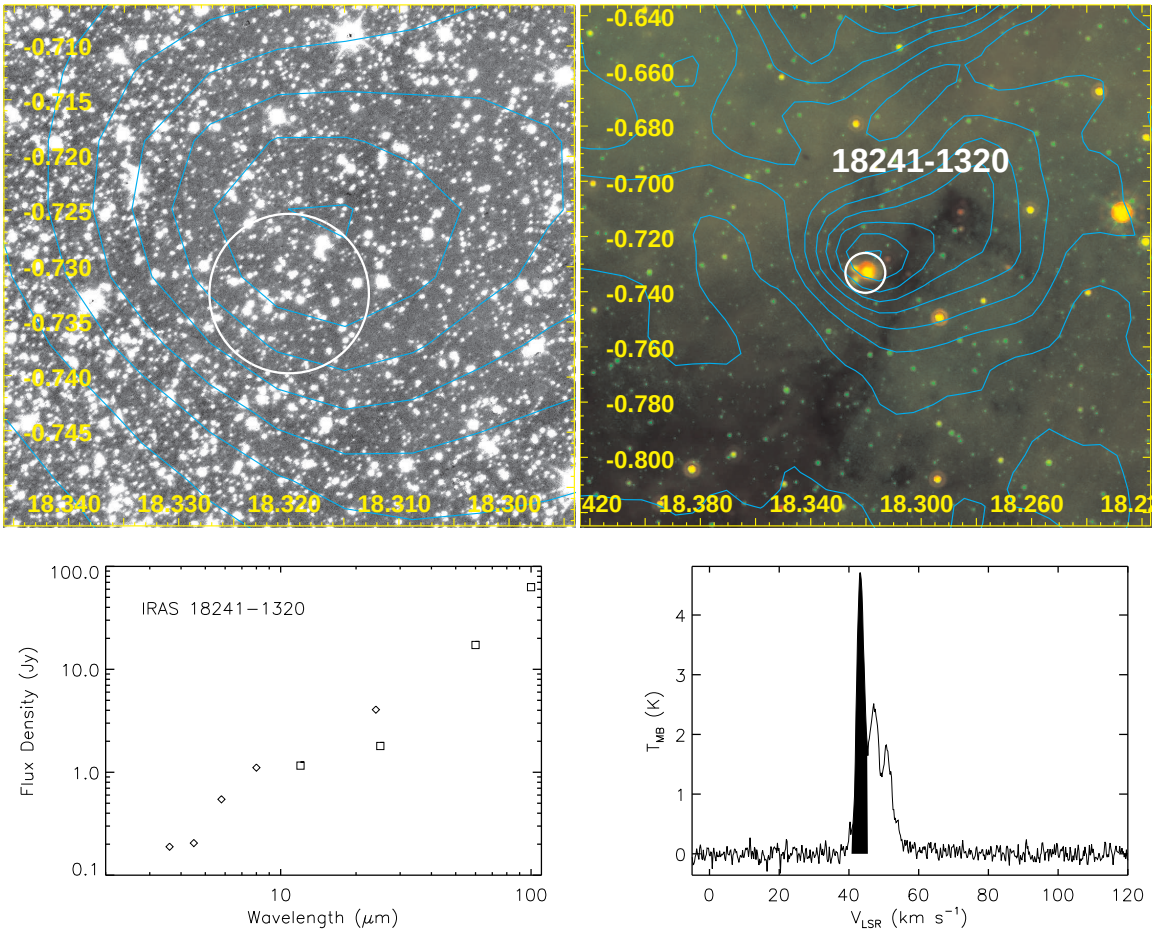

Figure 2.8 Four views of *IRAS* 18241-1320, like Figure 2.5. The guiding circle has a radius of 26″. It is a rather small blob of physical diameter 0.6 pc without any obvious clustering of stellar objects at the center of the blob. The blob is very likely, from spatial and velocity considerations, to be associated with the "clump" c7 in the cloud GRSMC G018.39-00.41 (Rathborne et al., 2009).

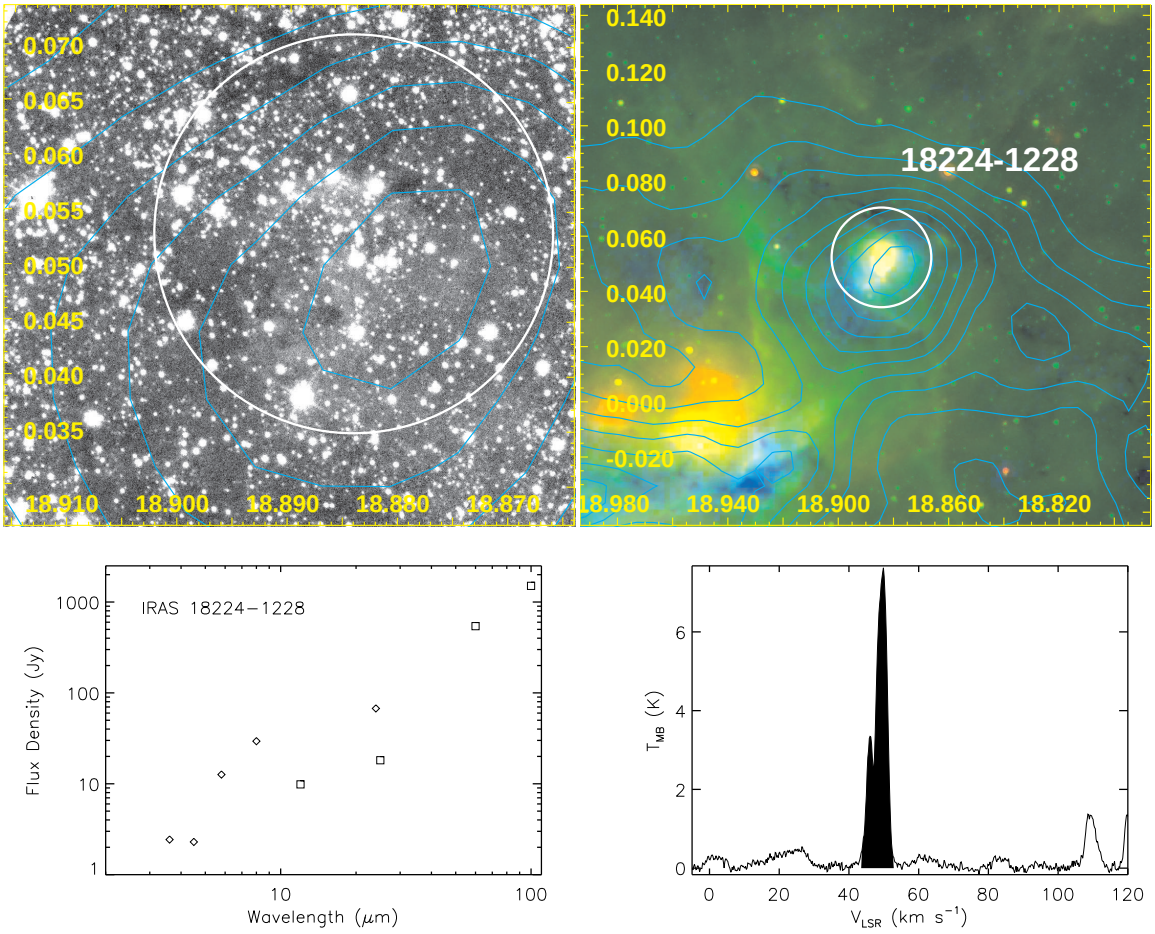

Figure 2.9 Four views of *IRAS* 18224-1228, like Figure 2.5. The guiding circle has a radius of 65″. The largest (1.7 pc) and the most luminous ($2.7 \times 10^4 L_\odot$) of the near objects sits on the outskirts of the W39 complex. This blob is probably associated with "clump" c1 (another possibility is c2) in the cloud GRSMC G018.89+00.04. Looking at the position of the blob compared to BGPS, an association with BGPS G018.890+00.045 is likely (another possibility is BGPS G018.879+00.053).

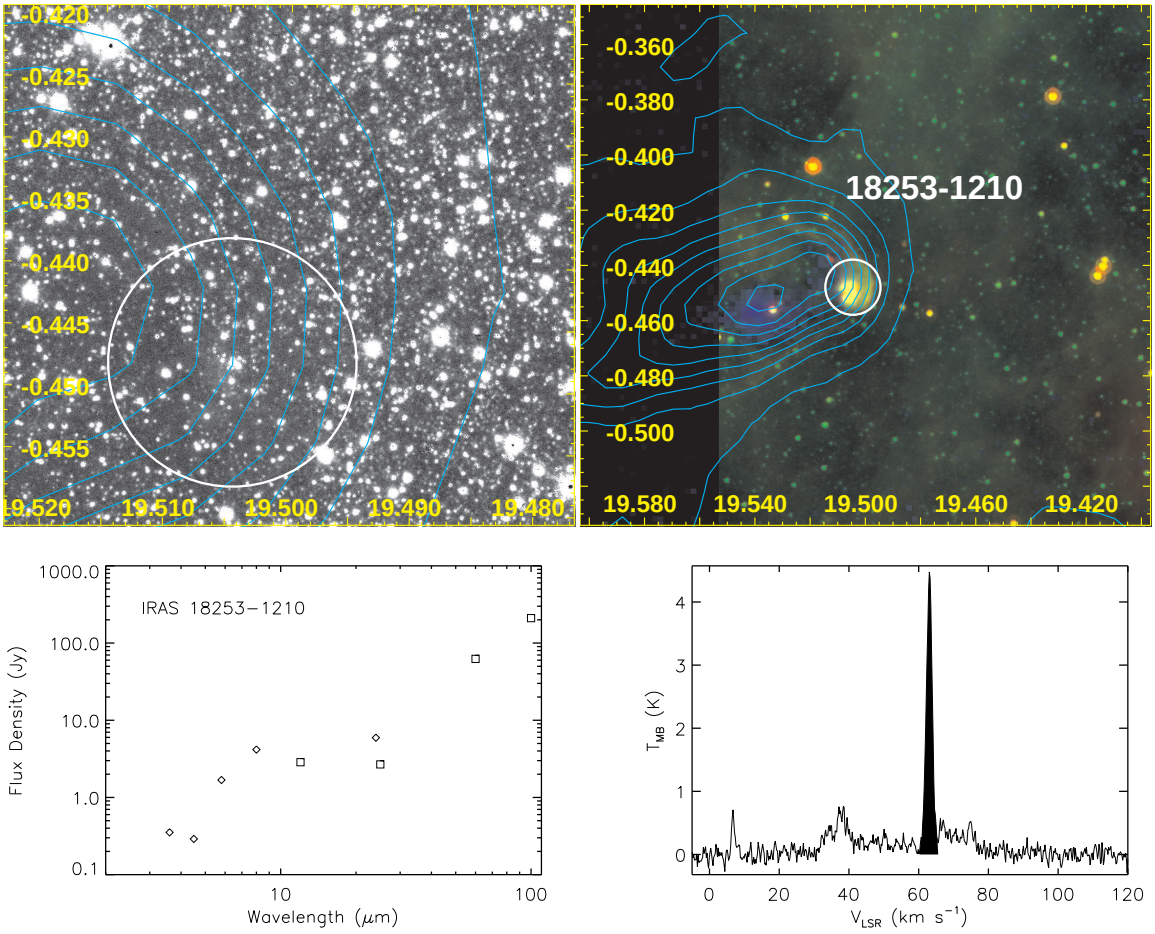

Figure 2.10 Four views of *IRAS* 18253-1210, like Figure 2.5. The guiding circle has a radius of 36″. This 1′ blob has a bow-shock like appearance. The molecular material indicated by the contours is associated with "clump" c1 in the cloud GRSMC G019.54-00.46. The *IRAS* blob is spatially associated with BGPS G019.507-00.447, while the position of maximum CO column density is spatially associated with BGPS G019.542-00.457.

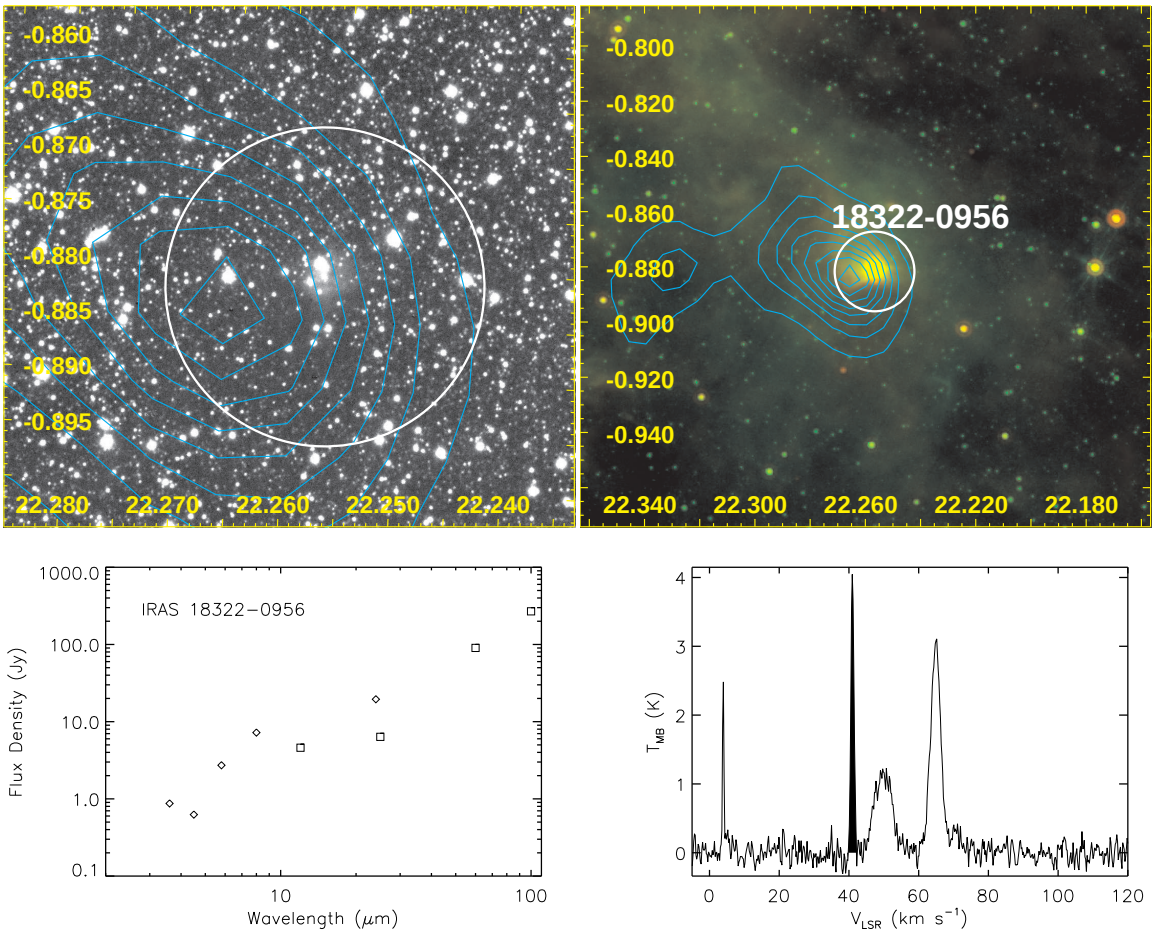

Figure 2.11 Four views of *IRAS* 18322-0956, like Figure 2.5. The guiding circle has a radius of 52″. This is an isolated 0.6′ blob, sitting on the edge of molecular material at 41.0 km s^{-1}. It is possible that this source could be at a velocity of $\sim$ 65 km s^{-1}, which would increase its physical diameter estimate by a factor of 1.4 and its luminosity estimate by a factor of 2.0.

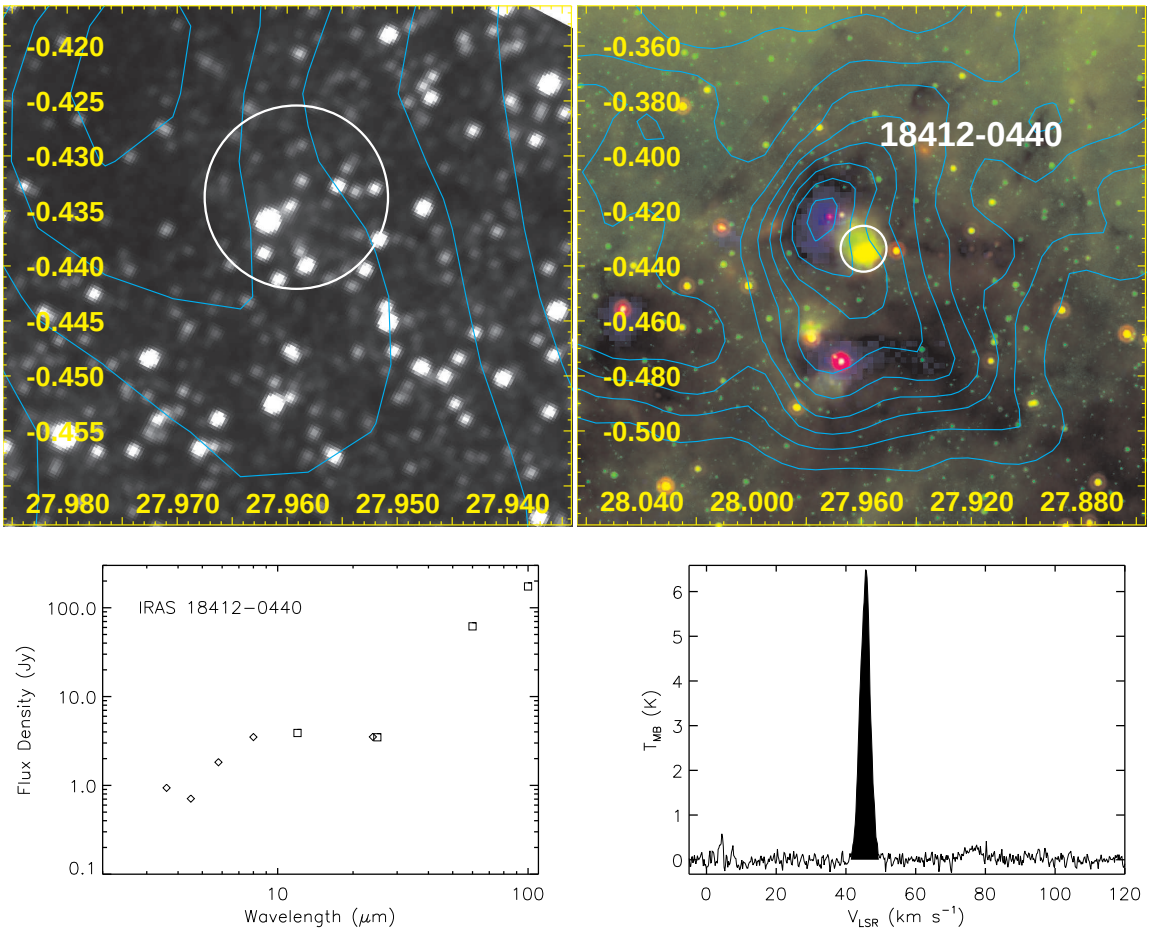

Figure 2.12 Four views of *IRAS* 18412-0440, like Figure 2.5. The guiding circle has a radius of 35″. It is a 0.8′ blob, clearly associated with IRDC G027.94-00.47 from Simon et al. (2006), which is seen to the left of the blob. Further associations are the "clump" c2 in GRSMC G027.99-0.46 and BGPS G027.972-00.422.

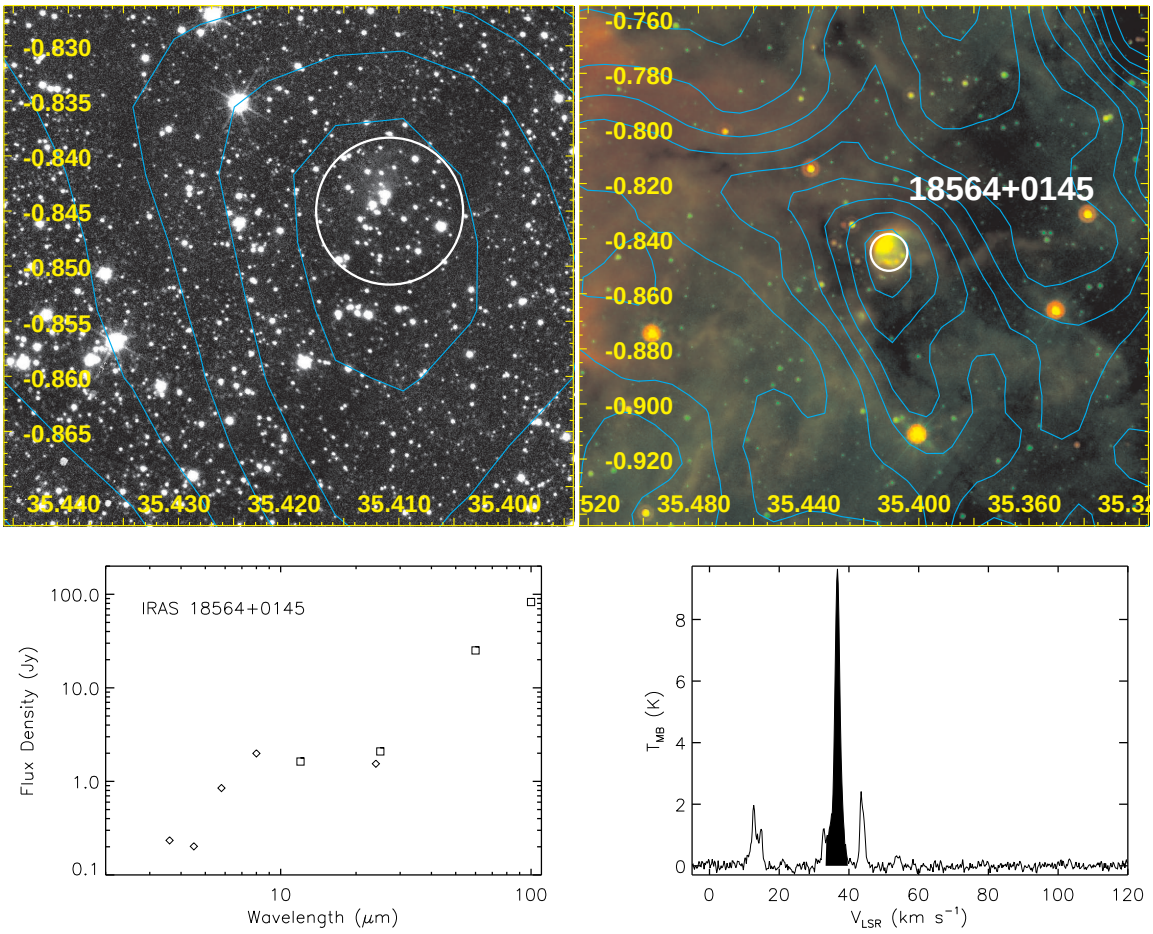

Figure 2.13 Four views of *IRAS* 18564+0145, like Figure 2.5. The guiding circle has a radius of 24″. This 0.7′ blob sits on CO that can be seen as dark absorption features in the 8.0 μm emission. The molecular material is likely referenced as "clump" c1 in GRSMC G035.59-00.91.

remaining unassigned objects, the mean diameter changes by very little.

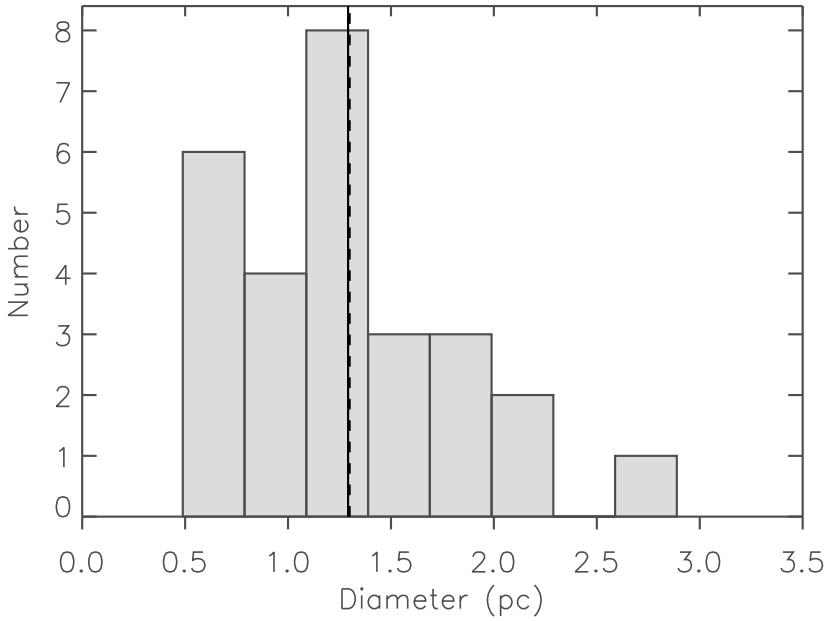

Figure 2.14 Histogram of diameters of the 27 IM SFRs that have assigned distances. The solid line represents the median size (1.3 pc) while the dashed line represents the average size (1.3 pc). The bin size is 0.3 pc.

2.4 Spectral Energy Distribution

Aperture photometry using circular apertures and background annuli, defined by eye, was performed on the Spitzer images based on the morphology of each object in the 8.0 and 24 μm images. Typical aperture radii range between 14″ and 162″ and are listed in Table 2.4. The irregular shapes and complex backgrounds near most targets, particularly at 8.0 and 24 μm, in addition to bright stars at the shorter bands, do not easily lend themselves to more quantitative approaches that could uniformly be applied to all bandpasses. Nevertheless, the relatively isolated nature of these objects makes it

possible to obtain a meaningful measure of their total flux densities using basic aperture photometry. Figure 2.15 shows the integrated flux density of one object, *IRAS* 18180-1342, as a function of aperture size, at each of the four IRAC and the MIPS 24 μm bandpasses. Note that the radial profiles are similar in each bandpass. The 8.0 and 24 μm flux densities asymptotically approach $\sim$ 42 and $\sim$ 50 Jy at a radius of 120$''$. The chosen aperture radius of 76$''$ encompasses about half of this total. Typically, the aperture defined by eye encompasses about half of the asymptotic flux density, while an extended envelope accounts for the other half. In some cases emission from a more extended envelope, and possibly other unrelated emission along the line of sight, exceeds half of the asymptotic flux density. In an effort to measure only the flux density from the immediate vicinity of the IM SFRs, the by-eye apertures were adopted. These produce flux densities that are typically a factor of two (0.3 dex) lower than the asymptotic flux densities. Table 2.4 lists the adopted aperture radii in arcsec and resultant flux densities (F_λ) for each object. Aperture corrections were applied as given by *Spitzer* SSC webpage handbooks. Specifically, the IRAC aperture correction[1] is of the analytical form $a \cdot e^{-b} + c$ where b depends on aperture and a and c are constants that depend on bandpass. For the 24 μm MIPS bandpass, the aperture correction[2] was estimated based on aperture size and it is typically 1.06. Uncertainties are dominated more by systematic effects stemming from aperture definition than statistical fluctuations. Relative systematic uncertainties were conservatively estimated to be 10% in each band, and were added in quadrature with the uncertainty in the flux calibration at each bandpass. The IRAC flux calibration uncertainties are 2% (Reach et al., 2005) and the MIPS 24 μm flux calibration uncertainty is 4% (Engelbracht et al., 2007). Saturation was not an issue for these sources, and total uncertainties are typically $\sim$ 10% for *Spitzer* photometry. Since MIPS 70 μm and 160 μm mosaics were unavailable at the time of this

[1] http://ssc.spitzer.caltech.edu/irac/iracinstrumenthandbook/
[2] http://ssc.spitzer.caltech.edu/mips/mipsinstrumenthandbook/

project, the flux densities from the *IRAS* PSC for the 60 and 100 μm bands ($\sim$ 15% flux density uncertainties) were used. All flux densities are listed in Table 2.4. The final SEDs, from 3.6 to 100 μm, were then plotted, see for example Figure 2.5, bottom left.

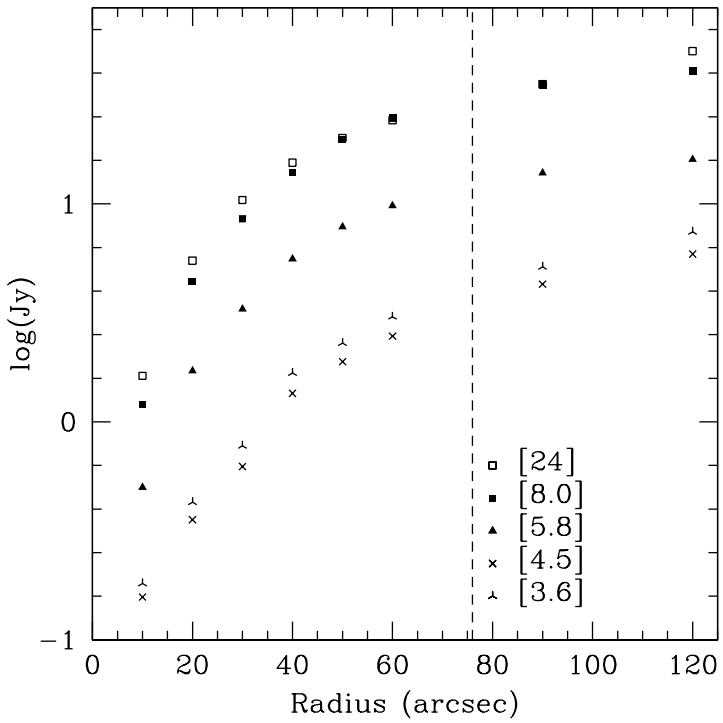

Figure 2.15 Figure showing the integrated flux density of *IRAS* 18180-1342 as a function of aperture radius at each of the four IRAC and the MIPS 24 μm bandpasses. The radial profiles are similar in each bandpass. The 8.0 and 24 μm flux densities asymptotically approach $\sim$ 42 and $\sim$ 50 Jy at a radius of 120″. The chosen aperture radius of 76″ is indicated by the dashed line and encompasses about half of this total.

In the vast majority of cases, the flux density in the shorter wavelength IRAC bands is $\sim$ 1 Jy and decreases from 3.6 to 4.5 μm. The SED then rises to a few Jy at 5.8 μm and continues to rise at 8.0 μm. This SED shape is a signature of PAH dominated objects, owing to the lack of PAH lines within the 4.5 μm band. All SEDs continue to rise through 24 μm, indicating the presence of hot dust. They are still rising in the *IRAS*

60 and 100 μm bands, typically reaching $F_\nu(100) \approx 200$ Jy. Typically the *IRAS* PSC $F_\nu(12)$ and $F_\nu(25)$ are lower than $F_{8.0}$ and F_{24} found using aperture photometry. This effect is expected for extended sources since the *IRAS* PSC filter suppresses extended emission, thus underestimating the true flux density. This effect is most dramatic at 12 and 25 μm (Fich & Terebey, 1996).

2.4.1 Infrared Luminosities

From the SEDs and distance estimates, the infrared luminosity ($L_{\rm IR}$) can be estimated by integrating under the curve. For the contribution from the *IRAS* PSC 60 and 100 μm flux densities, the method of Emerson (1988) was used. The luminosities (near and far) are then obtained by multiplying the fluxes by $4\pi d^2$, where d is the distance (near and far). These infrared luminosities are listed in Table 2.4. The tabulated luminosities are lower limits since they do not consider contributions from wavelengths longer than 135 μm (the edge of the *IRAS* 100 μm bandpass). Comparison of *IRAS*-derived luminosities with SEDs from the Diffuse Infrared Background Experiment (DIRBE) and the Balloon-borne Large Aperture Submillimeter Telescope (BLAST) suggest that $\sim 10\%$ of the total luminosity is missing (Kerton, 2000; Chapin et al., 2008).

The distribution of $L_{\rm IR}$ for the near eight objects is shown as a histogram in Figure 2.16 (left). The luminosities range from 7×10^2 to 3.7×10^4 $L_\odot$. Most are less than 10^4 solar luminosities, which is reflected in a median value of 4.9×10^3 $L_\odot$ (solid line) and an average value of 8.4×10^3 $L_\odot$ (dashed line). If instead these objects were considered to be at the far distance, the luminosities would range from 1.4×10^4 to 3.3×10^5 $L_\odot$, with a median value of 7.0×10^4 $L_\odot$ and an average value of 1.2×10^5 $L_\odot$.

The right panel of Figure 2.16 shows a histogram of the distribution of $L_{\rm IR}$ for the 27

Table 2.4 Photometry and luminosity of the objects listed as blobs or shells.

IRAS name	Aperture ($''$)	$F_{3.6}$ (Jy)	$\sigma_{3.6}$ (Jy)	$F_{4.5}$ (Jy)	$\sigma_{4.5}$ (Jy)	$F_{5.8}$ (Jy)	$\sigma_{5.8}$ (Jy)	$F_{8.0}$ (Jy)	$\sigma_{8.0}$ (Jy)	F_{24} (Jy)	σ_{24} (Jy)	$F_\nu(60)$ (Jy)	$F_\nu(100)$ (Jy)	Flag	$L_{\rm near}$ (10^3 $L_\odot$)	$L_{\rm far}$ (10^3 $L_\odot$)
18131-1606	54	2.28	0.23	1.47	0.15	6.60	0.68	14.74	1.51	42.39	5.67	305.0	799.3	N	10.7	234.3
18180-1342	76	3.78	0.54	3.05	0.31	11.68	1.20	29.40	3.01	29.98	4.01	216.6	830.6	N	4.9	248.5
18241-1320	26	0.19	0.02	0.21	0.02	0.55	0.06	1.11	0.11	4.05	0.37	17.2	62.8	N	1.2	14.3
18224-1228	65	2.43	0.25	2.29	0.24	12.63	1.29	29.43	3.02	67.49	6.92	542.6	1506.0	N	36.5	334.2
18253-1210	36	0.35	0.04	0.29	0.03	1.68	0.17	4.17	0.43	5.93	0.61	62.4	210.2	N	6.0	36.8
18322-0956	52	0.87	0.09	0.63	0.06	2.72	0.28	7.22	0.74	19.52	2.00	90.2	268.7	N	4.6	69.5
18308-0741	72	2.13	0.22	1.57	0.16	4.58	0.47	9.19	0.94	27.19	2.79	166.6	560.2	U	27.7	73.3
18370-0607	43	0.70	0.07	0.49	0.05	1.02	0.10	1.91	0.20	5.55	0.57	72.4	170.3	T	15.0	15.0
18367-0529	44	0.45	0.05	0.36	0.04	1.53	0.16	3.67	0.38	12.02	1.23	147.2	445.1	A	...	...
18362-0517	91	3.75	0.38	2.73	0.28	5.72	0.59	11.76	1.21	18.13	1.86	130.5	399.1	A	...	...
18412-0440	35	0.94	0.10	0.71	0.07	1.82	0.19	3.50	0.36	3.52	0.36	61.7	173.8	N	2.4	35.9
18411-0312	42	0.45	0.05	0.40	0.04	1.79	0.18	4.26	0.44	16.43	1.68	122.0	382.8	A	...	...
18433-0327	19	0.11	0.01	0.11	0.01	0.77	0.08	1.75	0.18	4.11	0.42	75.4	215.2	A	...	...
18441-0118	64	1.08	0.11	0.79	0.08	0.93	0.10	0.97	0.10	2.79	0.29	32.0	156.5	U	5.7	13.2
18463-0052	101	6.62	0.68	6.01	0.62	16.26	1.67	24.46	2.51	81.06	8.31	248.9	531.5	T	29.0	29.0
18502-0018	146	9.33	0.96	6.54	0.67	10.19	1.04	18.64	1.91	42.04	4.31	118.3	497.6	F	9.2	110.3
18504+0025	34	0.28	0.03	0.21	0.02	1.27	0.13	3.06	0.31	2.22	0.23	98.1	304.9	A	...	...
18537+0145	30	0.50	0.05	0.28	0.03	1.28	0.13	2.92	0.30	11.03	1.13	101.9	253.1	U	4.4	42.9
18527+0203	40	0.25	0.03	0.28	0.03	0.96	0.10	2.09	0.21	5.60	0.57	57.4	257.2	A	...	...
18564+0145	24	0.23	0.02	0.20	0.02	0.85	0.09	1.99	0.20	1.54	0.16	25.1	82.7	N	0.7	14.8
19014+0451	31	0.81	0.08	0.36	0.04	1.23	0.13	2.63	0.27	3.50	0.36	61.3	178.1	U	4.9	18.5
19012+0505-N	113	4.95	0.51	3.89	0.40	20.49	2.10	49.67	5.09	93.25	9.56	497.2	1156.0	N	10.7	177.8
19012+0505-S	122	4.79	0.49	3.59	0.37	20.36	2.09	37.42	3.83	25.64	2.63	497.2	1156.0	N	9.0	135.6
19023+0545	18	0.05	0.01	0.05	0.01	0.42	0.04	0.98	0.10	3.61	0.37	46.0	197.0	F	0.7	26.6
19023+0601	103	1.99	0.20	1.41	0.14	1.46	0.15	4.88	0.50	3.57	0.37	128.2	488.1	N	8.0	47.0
19027+0656	32	0.19	0.02	0.12	0.01	0.64	0.07	0.62	0.07	1.87	0.19	34.2	98.3	F	0.2	17.1
19060+0657	48	0.38	0.04	0.30	0.03	1.46	0.15	4.88	0.50	3.57	0.37	59.3	150.4	A	...	...
19072+0649	40	0.19	0.02	0.14	0.01	0.62	0.06	0.94	0.10	0.88	0.09	25.5	56.4	U	2.1	5.5
19049+0712	162	4.95	0.51	3.97	0.41	10.09	1.03	10.07	1.03	28.95	2.97	110.0	271.4	N	10.2	45.9
19062+0758	35	0.91	0.09	0.59	0.06	1.12	0.12	2.04	0.21	2.75	0.28	22.9	80.6	N	3.8	6.1
19105+0852	25	0.14	0.02	0.16	0.02	0.81	0.08	1.72	0.18	2.29	0.24	42.1	162.9	U	3.3	12.5
19056+0947	22	0.25	0.03	0.15	0.02	0.34	0.04	0.71	0.07	1.83	0.19	23.9	54.8	No CO	...	...
19139+1045	61	0.89	0.09	0.62	0.06	2.93	0.30	6.59	0.68	7.81	0.80	81.5	270.5	N	9.2	18.8
19138+1055	19	0.07	0.01	0.06	0.01	0.56	0.06	1.38	0.14	2.59	0.27	38.6	106.6	U	3.0	8.0
19157+1319	38	0.24	0.02	0.19	0.02	0.73	0.07	1.69	0.17	6.80	0.70	32.1	76.6	T	4.5	4.5
19207+1329	19	0.08	0.01	0.07	0.01	0.46	0.05	1.20	0.12	2.78	0.29	35.2	127.7	U	2.9	7.2
19207+1348	68	1.11	0.11	0.89	0.09	5.17	0.53	13.69	1.40	36.48	3.74	214.9	789.6	T	33.4	33.4
19156+1441	14	0.05	0.01	0.04	0.00	0.22	0.02	0.56	0.06	0.77	0.08	7.8	33.8	U	0.8	1.7
19193+1443	19	0.07	0.01	0.06	0.01	0.44	0.05	0.86	0.09	1.19	0.12	35.0	123.3	T	4.2	4.2
19233+1413	38	0.26	0.03	0.46	0.05	1.51	0.16	2.85	0.29	7.29	0.75	68.1	179.7	U	2.9	16.1
19205+1447	54	0.88	0.09	0.69	0.07	4.24	0.44	10.21	1.05	35.26	3.61	216.3	523.3	U	13.4	44.5
19221+1456	73	1.61	0.17	1.26	0.13	4.39	0.45	10.44	1.07	10.45	1.07	109.9	376.5	T	16.3	16.3
19214+1556	30	0.09	0.01	0.08	0.01	0.54	0.06	1.37	0.14	2.47	0.25	65.9	242.5	U	2.7	15.3
19255+1531	41	0.30	0.03	0.26	0.03	1.44	0.15	3.64	0.37	3.78	0.39	63.3	156.6	U	2.2	14.3
19256+1705	22	0.07	0.01	0.07	0.01	0.36	0.04	0.90	0.09	2.13	0.22	28.4	88.1	F	0.1	9.7
19248+1730	32	0.24	0.02	0.17	0.02	0.81	0.08	2.02	0.21	4.99	0.51	31.5	108.6	U	1.9	7.0
19247+1829	23	0.08	0.01	0.07	0.01	0.43	0.04	1.10	0.11	0.86	0.09	17.1	51.0	F	0.01	6.9
19260+1821	23	0.09	0.01	0.09	0.01	0.48	0.05	1.16	0.12	2.20	0.23	17.7	54.2	T	2.1	2.1
19266+1926	60	0.42	0.04	0.30	0.03	2.09	0.21	5.64	0.58	10.63	1.09	75.1	230.1	U	2.5	17.5
19330+1956	50	0.86	0.09	0.89	0.09	2.45	0.25	5.35	0.55	2.60	0.27	53.2	104.2	F	1.7	10.2

objects that have assigned distances. The luminosities range from 7×10^2 to 1.1×10^5 $L_\odot$. The median value is 9.2×10^3 $L_\odot$ (solid line) and the average value is 1.5×10^4 $L_\odot$ (dashed line). This luminosity range is consistent with recent models of young stellar object (YSO) SEDs (Robitaille et al., 2006). Figure 2.17 shows the model YSO luminosities of a range of objects that have optically thick disks (Stage II) as a function of stellar mass. Evidently, 10^3 to 10^4 $L_\odot$ corresponds roughly to $\sim 4 - 10$ $M_\odot$ YSOs, i.e., intermediate-mass. In Section 2.6.1, this range in luminosity is compared to luminosities of UCH II regions, showing that IM SFRs and UCH II regions are quite distinct sets.

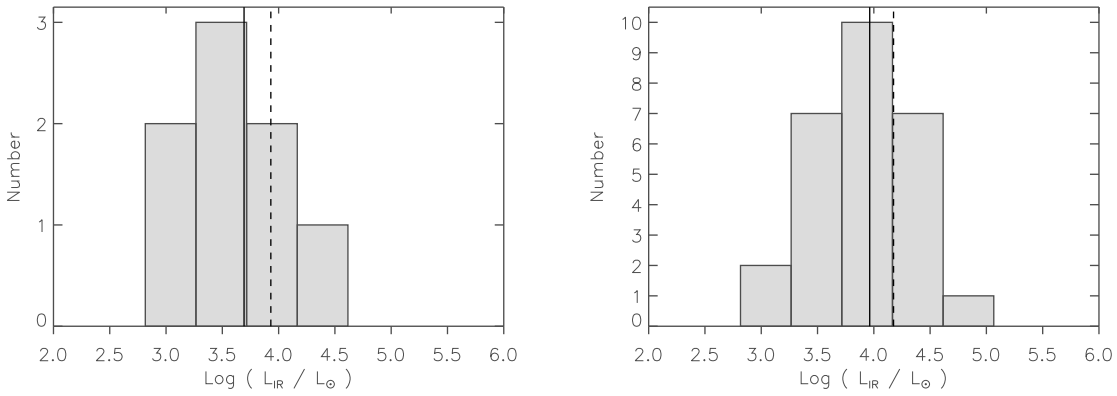

Figure 2.16 (Left) Histogram of $\log(L_{\rm IR}/L_\odot)$ for the eight near IM SFRs. The solid line represents log(median) = 3.7 while the dashed line represents log(average) = 3.9. (Right) Histogram of $\log(L_{\rm IR}/L_\odot)$ for the 27 IM SFRs that have assigned distances. The solid line represents log(median) = 4.0 while the dashed line represents log(average) = 4.2. The bin size is 0.45 dex.

2.5 Molecular Material and Masses

In this section, the molecular material that is spatially associated with the IM SFRs is investigated using the corresponding zeroth-moment maps. Usually, the location of the

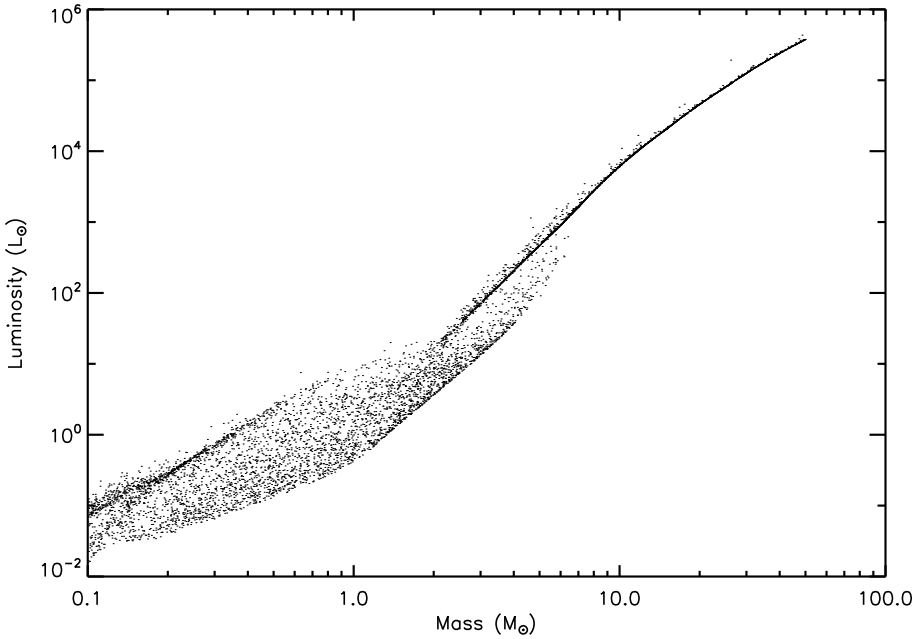

Figure 2.17 Robitaille et al. (2006) model YSO luminosities of a range of Stage II objects as a function of stellar mass. The $L_{\rm IR}$ range found in Section 2.4.1, 10^3 to 10^4 $L_\odot$, corresponds roughly to $\sim 4-10$ $M_\odot$ YSOs, i.e., intermediate-mass.

maximum value in the zeroth-moment map (i.e., the peak integrated intensity) for the local CO "clump" lies outside of the mid-IR blob/shell seen in *Spitzer* mosaics. Table 2.5 lists the *IRAS* name for sources having a velocity association from Table 2.3, the peak integrated intensity ($I_{\rm peak}$), the corresponding peak H_2 column density ($N(H_2)_{\rm peak}$) and peak mass column density ($N(M)_{\rm peak}$), the solid angle (Ω) occupied by the CO clump (used to calculate the mass), the flag from Table 2.3 indicating distance assumption, the near and far distance clump masses ($M_{\rm LTE}$), the parent GRS Molecular Cloud (GRSMC), associated GRSMC-clump, the mass of the GRSMC ($M_{\rm Cloud}$), and a note on the distance determination of the GRSMC.

Table 2.5 Properties of molecular material associated with the objects listed as blobs or shells, obtained using the GRS.

IRAS name	$I_{\rm peak}$ (K km s^{-1})	$N({\rm H_2})_{\rm peak}$ (10^{21} cm^{-2})	$N(M)_{\rm peak}$ (g cm^{-2})	Ω (10^{-7} sr)	Flag	$M_{\rm LTE}^{\rm near}$ ($M_\odot$)	$M_{\rm LTE}^{\rm far}$ ($M_\odot$)	Cloud GRSMC	Clump	$M_{\rm Cloud}$ ($M_\odot$)	Note
18131-1606	28.5	11.7	0.05	11.2	N	500	10100	···	···	···	
18180-1342	9.7	4.0	0.02	6.1	N	40	1800	···	···	···	
18241-1320	14.9	6.1	0.03	19.5	N	800	8700	G018.39-00.41	c7	46500	N
18224-1228	41.3	17.0	0.08	47.8	N	6100	56200	G018.89+00.04	c1	238500	F (!)
18253-1210	16.5	6.8	0.03	32.1	N	2800	17000	G019.54-00.46	c1	61600	F (!)
18322-0956	10.5	4.3	0.02	20.4	N	200	3800	none	none	···	
18308-0741	25.3	10.4	0.05	19.4	U	4300	11500	G024.09+00.44	c1	225100	N
18370-0607	14.7	6.0	0.03	10.8	T	1700	1700	G025.94-00.11	c3	156300	T
18412-0440	29.1	11.9	0.05	41.2	N	2300	34000	G027.99-0.46	c2	17000	N
18441-0118	15.2	6.2	0.03	20.0	U	2100	4900	none	none	···	
18463-0052	17.0	7.0	0.03	8.9	T	1600	1600	G031.79+00.14	c1	56300	T
18502-0018	21.2	8.7	0.04	4.8	F	200	2600	G032.89-00.46	c3	54500	F
18537+0145	9.6	3.9	0.02	3.7	U	100	900	none	none	···	
18564+0145	22.0	9.0	0.04	63.1	N	1000	21600	G035.59-00.91	c1	3600	N
19014+0451	19.2	7.9	0.04	3.8	U	200	800	G038.79-00.51	c1	109000	F
19012+0505-N	41.2	16.9	0.08	16.2	N	700	12200	G038.94-00.46	c2	308200	F (!)
19012+0505-S	35.8	14.7	0.07	25.8	N	1400	21200	G038.89-00.26	c1	1800	N
19023+0545	3.4	1.4	0.01	2.0	F	5	200	none	none	···	
19023+0601	17.3	7.1	0.03	4.3	N	200	900	G039.89-00.21	c6	···	···
19027+0656	12.9	5.3	0.02	11.3	F	40	3100	none	none	···	
19072+0649	11.5	4.7	0.02	9.7	U	700	1700	G041.14-00.86	c2	···	···
19049+0712	26.6	10.9	0.05	6.2	N	400	2000	G041.19-00.21	c4	218900	F (!)
19062+0758	16.2	6.6	0.03	16.4	N	1600	2600	G042.14-00.61	c2	211700	N
19105+0852	16.2	6.6	0.03	7.8	U	500	1800	G043.39-00.66	c2	1800	F
19139+1045	14.0	5.7	0.03	6.1	N	300	600	none	none	···	
19138+1055	23.3	9.5	0.04	12.2	U	1000	2600	none	none	···	
19157+1319	16.1	6.6	0.03	16.9	T	1400	1400	none	none	···	
19207+1329	17.2	7.1	0.03	7.0	U	500	1200	G048.84-00.51	c4	23200	F
19207+1348	31.7	13.0	0.06	19.1	T	4300	4300	G049.04-00.46	c3	22300	T
19156+1441	8.7	3.6	0.02	9.2	U	300	600	none	none	···	
19193+1443	7.6	3.1	0.01	13.1	T	600	600	G049.44-00.06	none	162600	T
19233+1413	23.0	9.4	0.04	15.6	U	600	3200	G049.54-00.91	c1	37500	F
19205+1447	32.4	13.3	0.06	22.0	U	2000	6700	G049.74-00.01	c1	5400	N
19221+1456	14.4	5.9	0.03	16.0	T	1300	1300	G050.44-00.41	c1	12500	T
19214+1556	25.5	10.4	0.05	18.7	U	1000	5400	G050.84+00.24	c2	12500	N
19255+1531	11.9	4.9	0.02	19.9	U	300	1800	G050.94-00.61	c2	6300	N
19256+1705	7.7	3.2	0.01	4.4	F	10	600	none	none	···	
19248+1730	6.1	2.5	0.01	8.2	U	100	500	none	none	···	
19247+1829	7.1	2.9	0.01	10.9	F	1	1300	none	none	···	
19260+1821	16.5	6.7	0.03	36.1	T	2000	2000	G053.49+00.49	c1	1800	T
19266+1926	14.6	6.0	0.03	17.4	U	400	2500	G054.64+00.79	c2	50900	F
19330+1956	10.6	4.4	0.02	7.5	F	100	900	G055.34+00.19	c2	15200	F

2.5.1 Column densities and masses from CO/H_2

To estimate column densities and molecular masses from GRS ^{13}CO observations, an optically thin, local thermodynamic equilibrium (LTE) situation for the ^{13}CO $J = 1 \rightarrow 0$ rotational line was assumed (CO is almost always close to LTE, see Rohlfs & Wilson, 2004). Furthermore, the excitation temperature is assumed approximately equal the main beam temperature; typically ~ 10 K for dense cold molecular material. The derived ^{13}CO column densities are only weakly sensitive to the exact choice of the excitation temperature, changing it to 20 K increases the derived mass by 40% (Simon et al., 2001). Under these assumptions, the expression for the column density of ^{13}CO is (Rohlfs & Wilson, 2004, eq. 14.40),

$$N(^{13}\mathrm{CO}) = 7.3 \times 10^{14} \int T_{\mathrm{MB}} \mathrm{d}V \ \mathrm{cm}^{-2} \tag{2.1}$$

Using isotope number ratios (R) from Simon et al. (2001) and references therein ($\mathrm{R}(^{12}\mathrm{CO}/^{13}\mathrm{CO}) = 45$ and $\mathrm{R}(^{12}\mathrm{CO}/\mathrm{H_2}) = 8 \times 10^{-5}$) the peak H_2 column density ($N(\mathrm{H_2})_{\mathrm{peak}}$) in cm^{-2} is calculated. The peak mass column density is then obtained by multiplying $N(\mathrm{H_2})_{\mathrm{peak}}$ with the H_2 molecular mass and a factor of 1.36 to account for elements heavier than hydrogen (Simon et al., 2001). Summing over the area of the ^{13}CO clump yields the (near and far distance) clump mass, given in Table 2.5. The uncertainty in the mass calculation from ^{13}CO is dominated by the background determination, and is estimated to be $\sim 10\%$. Using the Dominion Radio Astrophysical Observatory (DRAO) software IMVIEW, a polygon incorporating the local ^{13}CO feature seen in the zeroth-moment maps is drawn by eye. This polygon encloses the area given in Table 2.5. Typically, the polygon is drawn between 20% to 40% of I_{peak}. The polygon's perimeter defines the background level, and a plane is fitted to the perimeter in order estimate the background across the ^{13}CO feature. The sum of $N(M)$ above the fitted background plane inside the polygon is used to calculate M_{LTE}. More importantly, moderate opacity effects make column densities and derived masses lower limits that are estimated to be

accurate within a factor of a few (Simon et al., 2001).

The median and average peak mass column density obtained this way is 0.03 g cm^{-2} with a maximum of 0.08 g cm^{-2}. The mass of the local molecular material associated with the eight near sources, $M_{\rm LTE}$, range from 40 M$_\odot$ to 2800 M$_\odot$, and Figure 2.18 (left) shows a histogram of this distribution. The median of the masses is 900 M$_\odot$ (solid line) and the average is 1700 M$_\odot$ (dashed line). If instead these objects were considered to be at the far distance, the masses would range from 1.8×10^3 M$_\odot$ to 5.6×10^5 M$_\odot$, with a median value of 1.4×10^4 M$_\odot$ and an average value of 1.9×10^4 M$_\odot$. The right panel of Figure 2.18 shows a histogram of the distribution of $M_{\rm LTE}$ for the molecular material associated with the 27 objects that have assigned distances. The masses range from 40 M$_\odot$ to 6100 M$_\odot$, with a median of 1300 M$_\odot$ (solid line) and an average of 1500 M$_\odot$ (dashed line).

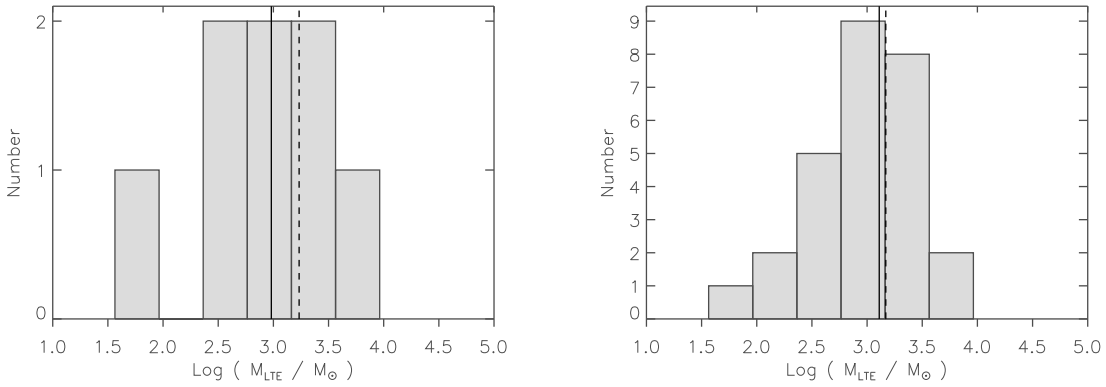

Figure 2.18 (Left) Histogram of $\log(M_{\rm LTE}/M_\odot)$ for the local molecular material associated with the eight near IM SFRs. The solid line represents log(median) = 3.0 while the dashed line represents log(average) = 3.2. (Right) Histogram of $\log(M_{\rm LTE}/M_\odot)$ for the local molecular material associated with the 27 IM SFRs that have assigned distances. The solid line represents log(median) = 3.1 while the dashed line represents log(average) = 3.2. The bin size is 0.4 dex.

2.5.2 Column densities and masses from BGPS

Out of the 50 objects, the ^{13}CO material is spatially associated with a millimeter-wave continuum source from the BGPS catalog (Rosolowsky et al., 2010) in 28 objects, 10 objects have no BGPS source associated, and 12 objects are not covered by the BGPS. Typically for an association, the BGPS continuum source is located on or very near the location of $I_{\rm peak}$. For some objects there are several BGPS sources within the ^{13}CO feature, but Table 2.6 only lists the source closest to $I_{\rm peak}$. The peak brightness within the BGPS source, $F_{\rm peak}$, is related to the peak column density, $N({\rm H_2})_{\rm peak}$, through the conversion factor of $N({\rm H_2})/F = 6.77 \times 10^{19}$ cm^{-2} (mJy beam^{-1})$^{-1}$ (Table A.1 in Kauffmann et al., 2008). From the peak H_2 column density traced by millimeter continuum emission, the peak mass column density is obtained as in Section 2.5.1. Column densities derived in this manner are lower limits for unresolved sources in the BGPS. The peak mass column densities traced by the BGPS are typically ~ 0.1 g cm^{-2}, with a minimum of 0.05 g cm^{-2} and a maximum of 0.5 g cm^{-2}. As seen in Figure 2.19, these peak mass column densities are higher than the corresponding peak mass column densities determined using the GRS. This is likely an effect of ^{13}CO becoming optically thick in the denser regions.

Out of the 28 BGPS sources, 22 have velocities from CO associations. Fifteen of them have distance determinations while seven do not. Using the integrated flux density (S) from the BGPS catalog together with the distance estimates, the source masses can be estimated using (Rosolowsky et al., 2010, eq. 10),

$$M = 13.1 {\rm M}_\odot \left(\frac{d}{1\ {\rm kpc}}\right)^2 \left(\frac{S}{1\ {\rm Jy}}\right) \left[\frac{\exp(13.0\ {\rm K}/T) - 1}{\exp(13.0/20) - 1}\right] \tag{2.2}$$

where $T = 10$ K like before. The results are given in Table 2.6. Figure 2.20 shows a histogram of the distribution of $M_{\rm BGPS}$ for the 15 objects with distance determinations. The masses range from 200 M$_\odot$ to 6700 M$_\odot$, with a median of 1000 M$_\odot$ (solid line) and

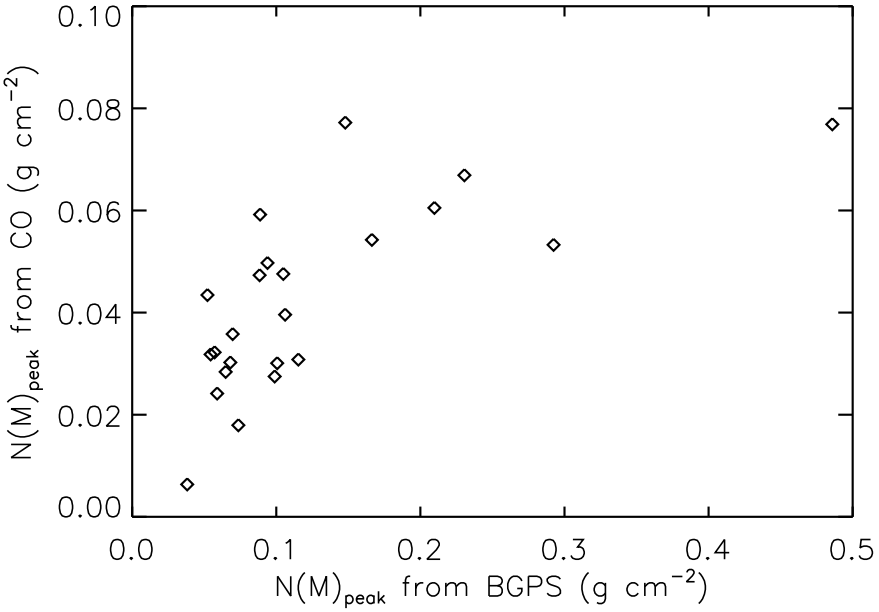

Figure 2.19 Peak mass column density obtained with millimeter-wave continuum (BGPS) versus peak mass column density obtained with ^{13}CO (GRS) for IM SFRs.

an average of 1400 $M_\odot$ (dashed line). This result largely agrees with ^{13}CO-based mass estimates.

2.5.3 Molecular Clouds

To investigate the possibility that IM SFRs are only found in low mass molecular clouds, the catalog of GRS molecular clouds (GRSMCs; Rathborne et al., 2009) was used to identify the large scale molecular clouds containing the IM SFRs. The identification was made by comparing the locations and velocities of so called "clumps" in Rathborne et al. (2009) to the identifications of molecular material. An identification was made if the clump has a tabulated velocity within ~ 1 km s^{-1} of the velocity listed in Table 2.3 and has a position centered on or very near the location of $I_{\rm peak}$. In 28 out of 42 cases,

Table 2.6 BGPS sources associated with the objects listed as blobs or shells.

IRAS name	Source BGPS	$F_{\rm peak}$ (Jy beam^{-1})	$N({\rm H_2})_{\rm peak}$ (10^{21} cm^{-2})	$N(M)_{\rm peak}$ (g cm^{-2})	S (Jy)	Flag	$M^{\rm near}_{\rm BGPS}$ ($M_\odot$)	$M^{\rm far}_{\rm BGPS}$ ($M_\odot$)
18131-1606	G014.634+00.308	0.92	62.4	0.29	2.3	N	800	16500
18180-1342	none	...	...	...	...	N	...	...
18241-1320	...	...	...	...	...	N	...	...
18224-1228	G018.890+00.045	0.47	31.6	0.15	2.9	N	1800	16100
18253-1210	G019.542-00.457	0.36	24.6	0.12	1.7	N	1300	8200
18322-0956	...	...	...	...	...	N	...	...
18308-0741	G024.100+00.456	0.28	18.9	0.09	0.6	U	800	2200
18370-0607	G026.190-00.179	0.31	21.1	0.10	0.6	T	1300	1300
18367-0529	G026.722+00.173	0.24	16.0	0.07	0.8	A	...	...
18362-0517	G026.827+00.391	0.16	11.0	0.05	0.2	A	...	...
18412-0440	G027.972-00.422	0.52	35.5	0.17	1.6	N	600	8800
18411-0312	G029.241+00.251	0.26	17.7	0.08	0.6	A	...	...
18433-0327	G029.285-00.333	0.43	29.0	0.14	2.2	A	...	...
18441-0118	G031.283+00.495	0.20	13.8	0.06	0.5	U	700	1500
18463-0052	G031.911+00.189	0.17	11.6	0.05	0.7	T	1400	1400
18502-0018	G032.861-00.411	0.33	22.6	0.11	1.4	F	600	6700
18504+0025	G033.544-00.133	0.16	10.7	0.05	0.4	A	...	...
18537+0145	G035.102-00.246	0.23	15.7	0.07	0.3	U	100	1300
18527+0203	G035.268+00.118	0.22	15.2	0.07	1.0	A	...	...
18564+0145	...	...	...	...	...	N	...	...
19014+0451	G038.758-00.530	0.22	14.9	0.07	0.4	U	300	1100
19012+0505-N	G038.920-00.352	1.53	103.7	0.49	6.4	N	1700	27600
19012+0505-S	G038.959-00.468	0.73	49.2	0.23	2.8	N	800	11700
19023+0545	none	...	...	...	...	F	...	...
19023+0601	G039.878-00.169	0.18	12.2	0.06	0.3	N	200	1100
19027+0656	G040.741+00.161	0.19	12.6	0.06	0.2	F	10	1000
19060+0657	none	...	...	...	...	A	...	...
19072+0649	...	...	...	...	...	U	...	...
19049+0712	G041.228-00.205	0.30	20.0	0.09	1.0	N	600	2800
19062+0758	G042.051-00.123	0.21	14.5	0.07	0.4	N	500	800
19105+0852	...	...	...	...	...	U	...	...
19056+0947	...	...	...	...	...	No CO	...	...
19139+1045	none	...	...	...	...	N	...	...
19138+1055	G045.524-00.363	0.16	11.1	0.05	0.4	U	300	700
19157+1319	G047.871+00.313	0.32	21.5	0.10	0.8	T	1000	1000
19207+1329	...	...	...	...	...	U	...	...
19207+1348	G048.872-00.512	0.28	18.9	0.09	0.6	T	700	700
19156+1441	...	...	...	...	...	U	...	...
19193+1443	none	...	...	...	...	T	...	...
19233+1413	...	...	...	...	...	U	...	...
19205+1447	G049.722-00.012	0.66	44.7	0.21	1.5	U	900	3000
19221+1456	none	...	...	...	...	T	...	...
19214+1556	G050.846+00.333	0.33	22.4	0.10	1.3	U	500	2900
19255+1531	...	...	...	...	...	U	...	...
19256+1705	none	...	...	...	...	F	...	...
19248+1730	none	...	...	...	...	U	...	...
19247+1829	...	...	...	...	...	F	...	...
19260+1821	none	...	...	...	...	T	...	...
19266+1926	...	...	...	...	...	U	...	...
19330+1956	none	...	...	...	...	F	...	...

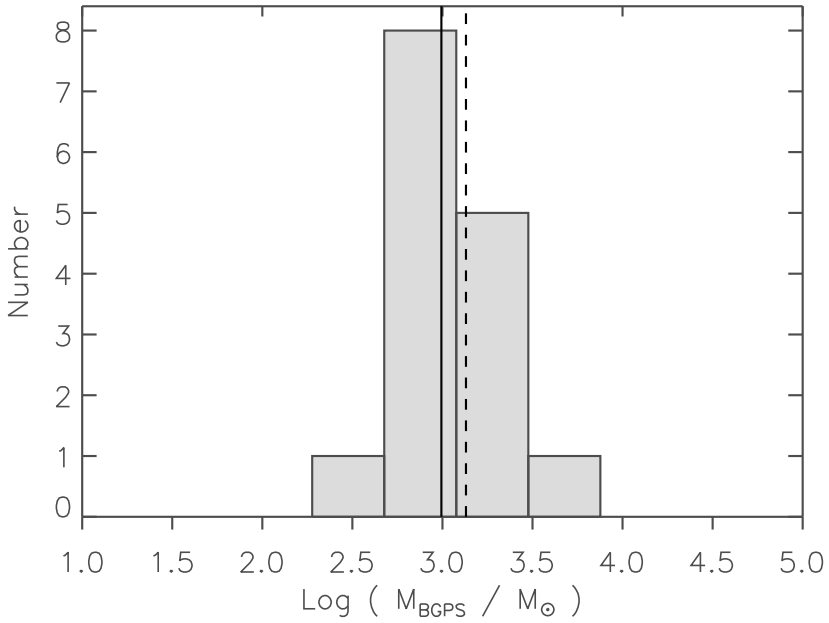

Figure 2.20 Histogram of $\log(M_{\rm BGPS}/M_{\odot})$ for the 15 objects with assigned distances that are associated with BGPS sources. The solid line represents log(median) = 3.0 while the dashed line represents log(average) = 3.1. The object with the highest $M_{\rm BGPS}$ in the figure is *IRAS* 18502-0018, an object dominated by an H II region (see Section 2.7). The bin size is 0.4 dex.

an association of a clump with a particular molecular cloud was possible (see Table 2.5).

Roman-Duval et al. (2009) lists distances to 26 of the 28 GRSMCs found to be associated with IM SFRs. Note that none of these GRSMCs have strong 21 cm continuum sources associated with them, therefore the kinematic distance ambiguity was resolved by the presence or absence of H I self-absorption (HISA). Only four of the 26 GRSMC distance determinations disagree with the IM SFR standard ruler method determinations, they are marked as (!) in Table 2.5. The ^{13}CO luminosity ($L(^{13}\mathrm{CO})$) of the cloud from Roman-Duval et al. (2009) and the same conversion factors used in Section 2.5.1 were used to compute the cloud mass. The results of the calculations are listed in Table 2.5.

Figure 2.21 shows a histogram of the 26 GRSMC masses where the four GRSMCs listed as (!) in Table 2.5 have been recalculated using the near distance d_{near} from Table 2.3. The GRSMC masses range from 1800 $M_\odot$ to 2.3×10^5 $M_\odot$, with a median of 2.3×10^4 $M_\odot$ (solid line) and an average of 5.1×10^4 $M_\odot$ (dashed line). These fall toward the lower end of the range in mass expected of Giant Molecular Clouds (GMCs; $10^4 - 10^6$ $M_\odot$).

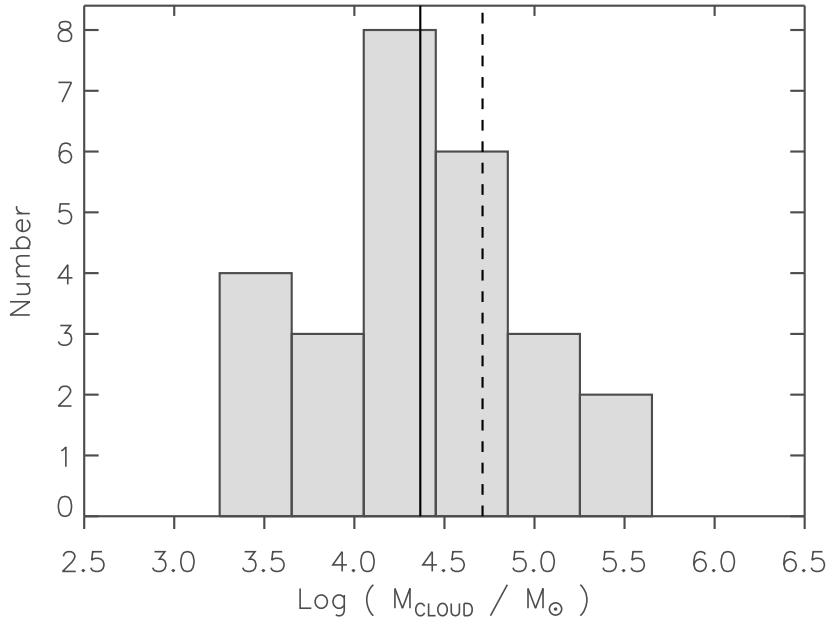

Figure 2.21 Histogram of $\log(M_{\rm Cloud}/M_\odot)$ for the 26 GRSMCs associated with the IM SFRs. The four GRSMCs listed as (!) in Table 2.5 have been scaled to the near distance using d_{near} from Table 2.3. The solid line represents log(median) = 4.4 while the dashed line represents log(average) = 4.7. The bin size is 0.4 dex.

2.6 Comparison to UCH II regions

UCH II regions are manifestations of newly formed massive stars that are still embedded in their natal molecular clouds. They are small (< 0.1 pc), dense ($> 10^4$ cm^{-3}),

bright photoionized nebulae. At *IRAS* 100 μm they are among the brightest objects in the Galaxy because of the warm dust envelope converting the entire stellar luminosity into FIR radiation. These relatively well-studied objects are compared to the IM SFRs, showing that UCH II regions are quite distinct from IM SFRs in luminosity, in column density, and in the mass of associated material traced with millimeter-wave continuum emission. Table 2.7 lists the UCH II source names, their *IRAS* identification, adopted distance and $L_{\rm IR}$, all from Wood & Churchwell (1989a). Then the associated BGPS source, peak brightness, peak H_2 column density, peak mass column density, BGPS integrated flux density and associated mass are given.

2.6.1 UCH II region luminosities

Figure 2.22 shows a histogram of the infrared luminosities ($L_{\rm IR}$) of the IM SFRs (shaded), with all the objects labeled Unassigned ("U" in Table 2.3) assumed to be at the far distance (as a most extreme case scenario). The barred histogram shows $L_{\rm IR}$ for 42 of the UCH II regions in Table 18 of Wood & Churchwell (1989a). In both cases contributions to $L_{\rm IR}$ from wavelengths longer than the edge of the *IRAS* 100 μm bandpass were not considered, and so in both cases $L_{\rm IR}$ are lower limits to the bolometric luminosities. The luminosity distribution is bi-modal, with UCH II regions and IM SFRs forming two distinct populations separated by roughly an order of magnitude. In fact, the overlapping region at the higher end of the IM SFR luminosity distribution (shaded) consists of objects with unassigned distances (which were all assumed at the far distance for the figure). If they instead were assumed to be at near distance only one object would overlap with the lower end of the UCH II region distribution, and that object turns out to be dominated by an H II region (*IRAS* 18502-0018, see Section 2.7). Comparing the median (or average) shows that UCH II regions are typically 40–80 times more luminous than IM SFRs.

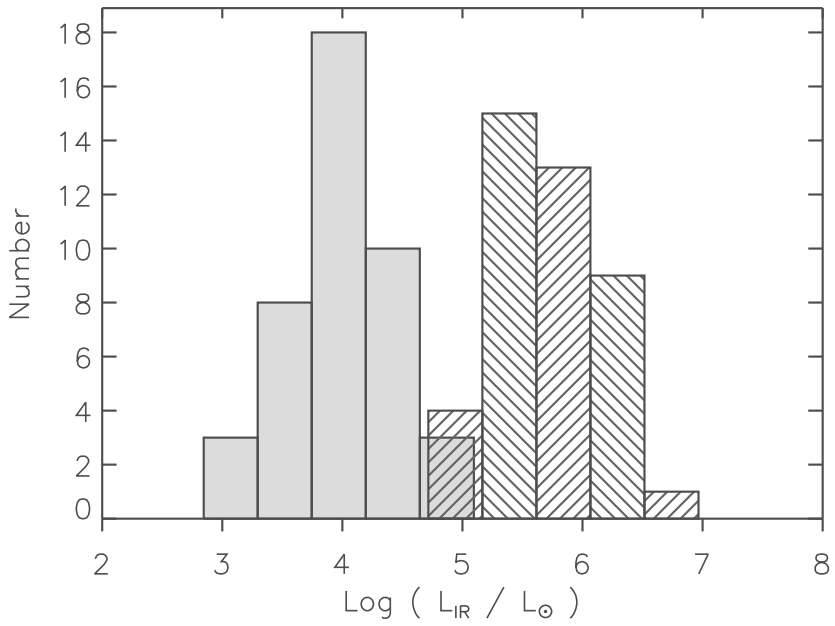

Figure 2.22 Histogram of $\log(L_{\rm IR}/L_{\odot})$ for 42 IM SFR luminosities (shaded, with unassigned objects assumed to be at the far distance) and for 42 UCH II region luminosities (barred) from Wood & Churchwell (1989a). The luminosity distribution is bi-modal, with UCH II regions and IM SFRs forming two distinct populations separated by roughly an order of magnitude. The IM SFR overlap consists of unassigned objects and *IRAS* 18502-0018, an object dominated by an H II region (see Section 2.7). The bin size is 0.45 dex.

2.6.2 UCH II regions in the BGPS

The positions of UCH II regions with adopted distances (Table 4 in Wood & Churchwell, 1989a) were examined by eye for association with a millimeter-wave continuum source from the BGPS catalog (Rosolowsky et al., 2010). For 33 UCH II regions, an associated BGPS source were found. Using the same technique as were used for IM SFRs in Section 2.5.2, peak mass column densities toward these UCH II regions were calculated. Figure 2.23 shows peak mass column densities for IM SFRs (shaded) and UCH II

regions (barred). The peak mass column density distribution is roughly bi-modal, with UCH II regions and IM SFRs forming two populations separated by roughly an order of magnitude. Comparing the median (or average) shows that peak mass column densities for the material associated with UCH II regions are typically $\sim$ 10 times greater than for IM SFRs.

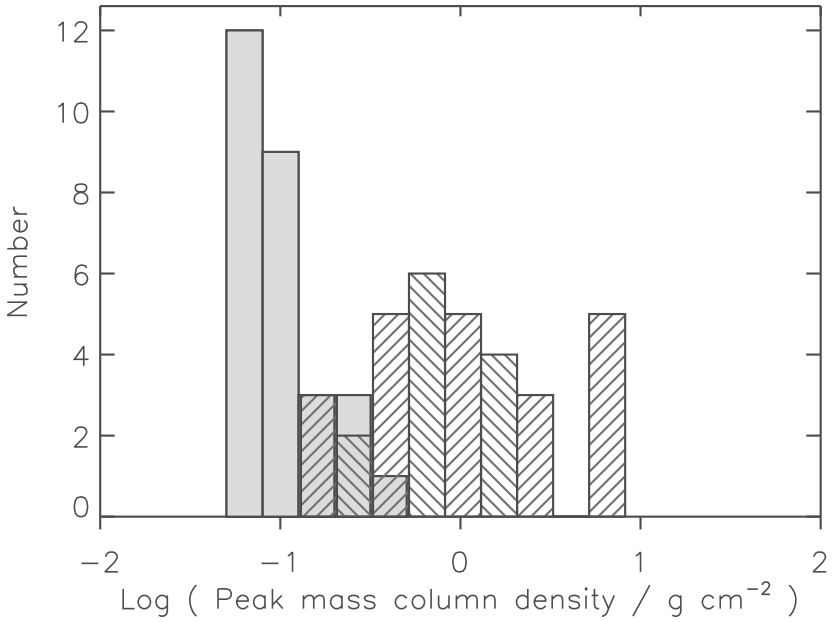

Figure 2.23 Histogram of the peak mass column density, $\log(N(M)_{\rm peak}/{\rm g\ cm^{-2}})$ for the material associated with 28 IM SFRs, traced by millimeter-wave continuum (shaded) and for the material associated with 33 UCH II regions (barred). The mass column density distribution is roughly bi-modal, with UCH II regions and IM SFRs forming two populations separated by roughly an order of magnitude. The bin size is 0.2 dex.

Equation 2.2 with the same assumptions as in Section 2.5.2 were again used, together with the adopted distances from Table 4 in Wood & Churchwell (1989a) to compute the masses of the cold, dense material associated with the UCH II regions. The masses

of the material associated with UCH II regions is shown as the barred histogram in Figure 2.24 while the shaded histogram is the mass of the material closely associated with the IM SFRs (from Table 2.6, with unassigned objects being assumed to be at the far distance). As with the distributions of luminosities and peak mass column densities, the masses of the closely associated material form a bi-modal distribution, with UCH II regions and IM SFRs forming two populations separated by roughly an order of magnitude. The one overlapping shaded object is again *IRAS* 18502-0018. Comparing the median (or average) of the two populations shows material associated with UCH II regions is typically ~ 20 times more massive than the material associated with IM SFRs.

2.7 Discussion

Radio continuum images from the NRAO/VLA Sky Survey (NVSS; Condon et al., 1998) at 1.42 GHz show that all but one of the investigated blobs/shells lack 1.42 GHz continuum emission from H II . NVSS has a 45″ FWHM resolution and rms brightness uncertainties of about ~ 0.45 mJy beam^{-1} ≈ 0.14 K (Stokes I). The completeness limit is about 2.5 mJy. Radio continuum measurements of H II regions can provide a lower limit on the total number of ionizing photons (N_L),

$$N_L \geq 7.5 \times 10^{43} S_\nu d^2 \nu^{0.1} T_e^{-0.45} \text{ s}^{-1} \tag{2.3}$$

where ν is the frequency in GHz, S_ν is the flux density measured at frequency ν in mJy, d is the distance to the source in kpc, and T_e is the electron temperature in units of 10^4 K (Rudolph et al., 1996). This assumes an optically thin, spherical, constant-density H II region. Given the adopted distances in Table 2.3, a 3σ NVSS detection would correspond to about $\log(N_L) \sim 45$ (with a maximum of 46.1). For comparison, a B0.5 V star powered H II region has $\log(N_L) = 47.77$ (Schaerer & de Koter, 1997) and would

Table 2.7 BGPS sources associated with the UCH II regions.

Source(s)[a]	*IRAS*[a] identification	Adopted Distance[a] (kpc)	L_{IR}[a] (10^4 $L_\odot$)	Source BGPS	F_{peak} (Jy beam^{-1})	$N(H_2)_{peak}$ (10^{22} cm^{-2})	$N(M)_{peak}$ (g cm^{-2})	S (Jy)	M_{BGPS} (10^3 $M_\odot$)
G8.14+0.23	17599-2148	4.2	19.2	G008.141+00.224	3.7	25	1.2	14.2	9.6
G8.67-0.36	18032-2137	6.2	26.4	G008.670-00.356	8.1	55	2.6	17.9	26.3
G10.15-0.34	18064-2020	6.0	148.0	G010.152-00.344	2.2	15	0.7	10.3	14.2
G10.30-0.15	18060-2005	6.0	73.4	G010.300-00.148	3.7	25	1.2	8.0	11.0
G10.47+0.03 complex	18056-1952	7.3	67.9	G010.472+00.026	17.3	117	5.5	20.8	42.3
G10.62-0.38 complex	18075-1956	6.5	124.0	G010.625-00.384	18.5	125	5.9	20.0	32.3
G12.21-0.10	Co-add/18097-1825A	16.1	144.0	G012.209-00.104	4.6	31	1.5	7.7	76.7
G12.43-0.05	18099-1810	16.7	17.3	G012.435-00.050	0.4	3	0.1	2.8	30.0
G15.04-0.68	18174-1612	2.1	43.3	G015.031-00.670	19.1	129	6.1	97.9	16.5
G19.07-0.27 complex	18239-1228	5.4	26.2	G019.077-00.287	2.3	16	0.7	9.9	11.0
G19.61-0.23 complex	18248-1158	4.5	26.1	G019.609-00.233	8.0	54	2.5	10.9	8.5
G20.08-0.14 complex	Co-add	4.1	7.3	G020.082-00.135	2.8	19	0.9	5.9	3.8
G23.46-0.20	18319-0834	9.0	87.5	G023.440-00.206	0.7	5	0.2	2.2	6.9
G23.71+0.17	18311-0809	9.0	39.9	G023.711+00.170	1.5	10	0.5	5.5	17.1
G23.96+0.15	18317-0757	6.0	24.9	G023.955+00.150	1.7	11	0.5	7.4	10.1
G25.71+0.05	18353-0628	14.0	59.4	G025.713+00.045	0.9	6	0.3	2.4	17.8
G27.28+0.15	18379-0500	15.2	50.4	G027.283+00.149	1.1	7	0.3	8.6	75.5
G29.96-0.02	18434-0242	9.0	198.0	G029.955-00.018	5.6	38	1.8	10.8	33.3
G30.54+0.02 complex	18443-0210	13.8	51.6	G030.536+00.021	1.1	7	0.3	2.8	20.0
G31.41+0.31	18449-0115	8.5	27.9	G031.414+00.307	10.2	69	3.2	20.3	55.9
G33.92+0.11	18502+0051	8.2	31.0	G033.914+00.107	3.1	21	1.0	8.5	21.8
G34.26+0.15 complex	18507+0110	3.7	59.3	G034.258+00.154	25.6	174	8.1	78.5	41.1
G35.05-0.52	18545+0134	12.7	39.9	G035.052-00.516	0.5	4	0.2	1.5	9.4
G37.55-.011	18577+0358	12.0	47.5	G037.547-00.112	1.0	7	0.3	2.6	14.0
G43.18-0.52	19097+0847	4.6	5.2	G043.177-00.521	2.0	14	0.6	4.6	3.7
G45.07+0.13	19110+1045	9.7	142.4	G045.069+00.133	2.9	19	0.9	4.8	17.1
G45.12+0.13	19111+1048	9.5	166.0	G045.121+00.133	4.3	29	1.4	9.8	33.8
G45.45+0.06	19120+1103	9.7	144.0	G045.453+00.061	2.4	16	0.8	7.9	28.4
G45.47+0.05	19120+1103	9.7	149.0	G045.465+00.047	1.9	13	0.6	5.2	18.6
G45.48+0.13	19117+1107	9.7	97.5	G045.477+00.135	1.6	11	0.5	6.8	24.5
W51d complex	19213+1424	7.0	341.0	G049.489-00.370	20.9	142	6.6	80.2	150.1
G54.10-0.06	19294+1836	7.9	17.5	G054.108-00.049	0.6	4	0.2	5.3	12.7
G61.48+0.09 complex	19446+2505	2.0	10.2	G061.475+00.090	5.4	37	1.7	18.5	2.8

[a]From Wood & Churchwell (1989a)

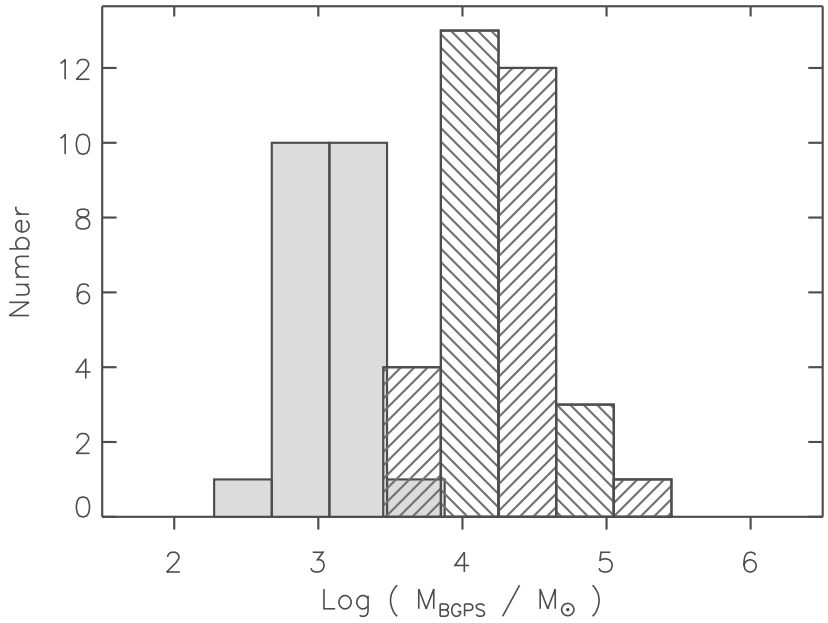

Figure 2.24 Histogram of $\log(M_{\rm BGPS}/M_{\odot})$ for the material associated with 22 IM SFRs, traced by millimeter-wave continuum (shaded, with unassigned objects assumed to be at the far distance) and for the material associated with 33 UCH II regions (barred). The mass distribution is bi-modal, with UCH II regions and IM SFRs forming two distinct populations separated by roughly an order of magnitude. The IM SFR overlap consists of *IRAS* 18502-0018, an object dominated by an H II region (see Section 2.7). The bin size is 0.4 dex.

easily be detected at a 3σ level in NVSS if $d \leq 75$ kpc.

Highly embedded massive stars can potentially be radio quiet due to the absorption of ultraviolet photons by surrounding dust. It is very unlikely that this study is probing massive stars at such a very early stage because the sample's range in luminosity, total molecular mass and mass column density are all much lower than those associated with regions of known massive star formation. The conclusion drawn is that the lack of radio continuum emission in these sources is consistent with our interpretation of them as IM SFRs.

The only apparent exception, *IRAS* 18502-0018, actually consists of a 0.4′ blob located on the edge of a dusty 2.5′ diameter H II region, see Figure 2.25. Applying the standard ruler technique to the 0.4′ blob results in a distance of 11.1 kpc, which agrees with the distance found for the associated GRSMC (Roman-Duval et al., 2009). The 1.42 GHz continuum emission associated with the H II region has a flux density of $S_\nu = 126.7 \pm 5.1$ mJy in the NVSS catalog. This corresponds to $\log(N_L) = 48.1$ or a single B0 V star (Schaerer & de Koter, 1997). This region is interpreted as a possible IM SFR sitting on the edge of a dusty shell surrounding a small H II region.

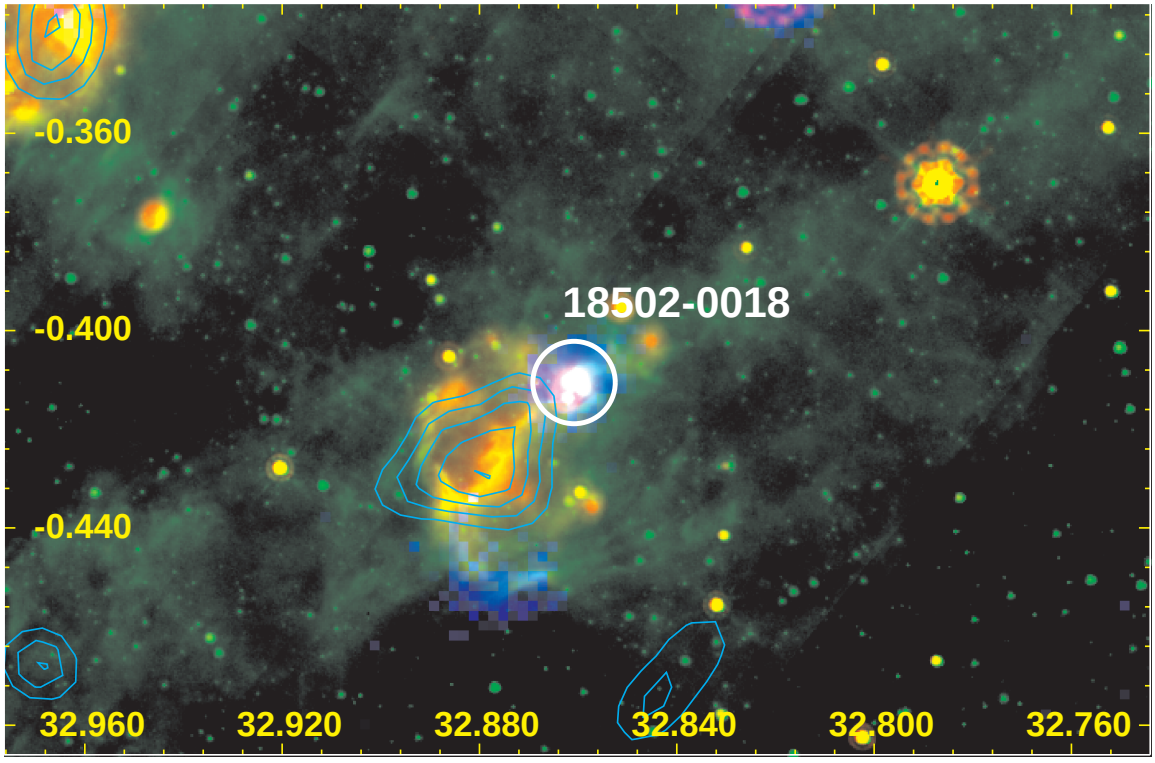

Figure 2.25 *IRAS* 18502-0018, an object dominated by an H II region. The contours correspond to 0.03, 0.025, 0.02, 0.015 and 0.01 Jy beam^{-1} in NVSS.

The large-scale molecular environment associated with IM SFRs is found to be sim-

ilar to that associated with high-mass star formation; IM SFRs are found in molecular clumps of $\sim 10^3$ $M_\odot$ sitting within Giant Molecular Clouds (GMCs) with a range of masses between $10^4 - 10^5$ $M_\odot$. The implication of this result is that massive star formation, while possible in GMCs in this mass range, is not inevitable. IM SFRs are also associated with lower mass $\sim 10^2$ $M_\odot$ clumps, much lower than those associated with high mass star formation (Zinnecker & Yorke, 2007). In contrast, no IM SFRs are found in GMCs with masses $\geq 10^6$ $M_\odot$, suggesting that for the most massive GMCs, high-mass stars will always form.

The left hand panel of Figure 2.26 shows a strong correlation between luminosity and associated clump mass for both IM SFRs and UCH II regions. The data are fit by $L \propto M^{1.12\pm0.08}$ which agrees with the mass-luminosity relationship found by Chini et al. (1987) that was derived using only a sample of compact H II regions. This relationship clearly holds over three orders of magnitude, a result only hinted at in Chini et al. (1987).

In the right panel of Figure 2.26 luminosity versus peak mass column density for the sample of IM SFRs and UCH II regions is plotted. Krumholz & McKee (2008) provide a theoretical expectation that mass column densities ≥ 1 g cm^{-2} are needed for massive star formation. The maximum mass column density for IM SFRs is observed to be 0.5 g cm^{-2} and both the median and the average are ~ 0.1 g cm^{-2}, all well below the proposed threshold. A simple interpretation of the data shown in the right panel of Figure 2.26 is that if the mass column density is above 1 g cm^{-2}, only massive stars will form, below 1 g cm^{-2} intermediate through massive stars can form, and at or below 0.1 g cm^{-2}, no massive stars will form.

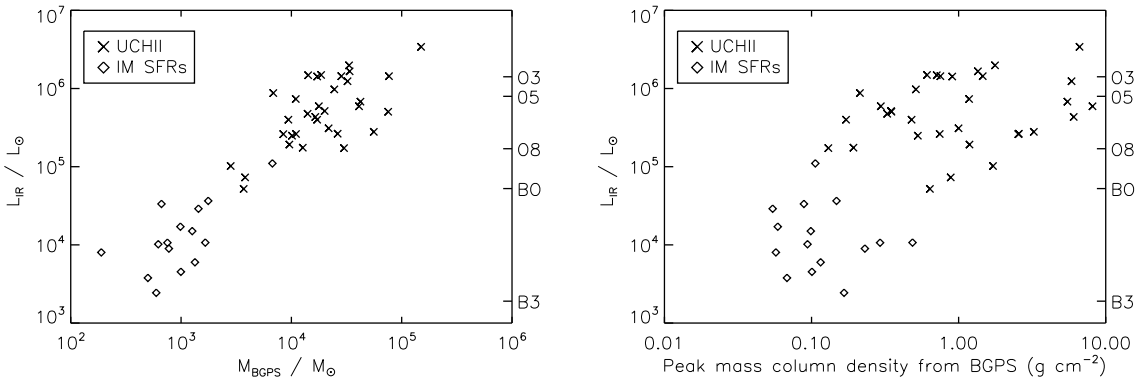

Figure 2.26 (Left) Luminosity versus associated mass. (Right) Luminosity versus the peak mass column density, traced by millimeter-wave continuum. IM SFRs (15 objects) are diamonds. UCH II regions (33 objects) are crosses. The scale on the right is spectral type of a single class V star.

2.8 Conclusions

A sample of 50 IM SFRs in the inner Galaxy has been identified. The IM SFRs share some basic properties. They have typical luminosities of $\sim 10^4$ $L_\odot$ and the PDRs that demarcate the IM SFRs have typical diameters of ~ 1 pc. All but one lack radio continuum emission and some show small stellar clusters visible in the NIR. These properties are consistent with these objects being regions containing stars in the $2 - 8$ $M_\odot$ range with their associated clusters of low-mass stars. The most massive stars in these regions are likely to be precursors to Herbig AeBe stars.

IM SFRs do show some similarities with high-mass star-forming regions. On parsec-scales IM SFRs are typically associated with molecular clumps of mass $\sim 10^3$ $M_\odot$ and on larger scales they are found within GMCs with masses between $10^4 - 10^5$ $M_\odot$. The conclusion drawn is that massive star formation in GMCs in that mass range is not inevitable.

IM SFRs are also distinct from regions of more massive star formation, forming in clumps with masses as low as $\sim 10^2$ $M_\odot$ and not being found in the most massive GMCs ($\geq 10^6$ $M_\odot$). IM SFRs typically have an order of magnitude less luminosity than UCH II regions.

The sample of IM SFRs, combined with UCH II region data, shows that a strong correlation between luminosity and associated molecular mass in star-forming regions applies over three orders of magnitude encompassing both IM SFRs and UCH II regions.

The molecular material associated with IM SFRs typically have an order of magnitude smaller peak mass column density and clump mass compared to UCH II regions. The lack of IM SFRs found with associated peak mass column densities > 0.5 g cm^{-2} supports the idea that there is a threshold in mass column density above which only massive star formation occurs.

CHAPTER 3. CTB 102 – AN ENORMOUS GALACTIC H II REGION

3.1 Introduction

The radio bright outer Galaxy region CTB 102 ($\ell = 93\overset{\circ}{.}060,\ b = +2\overset{\circ}{.}810$) was first cataloged by the Wilson & Bolton (1960) radio survey of the Galactic plane. The source is then mentioned in subsequent Galactic radio surveys including Kallas & Reich (1980) where it is identified as KR 1. Using radio recombination line (RRL) observations at $\lambda 3$ cm, Lockman (1989) (H87α, $\sim 3'$ beam) identified the region as a H II region with a line brightness of $T_{line} = 18 \pm 1.3$ mK, a velocity of $V_{\rm LSR} = -61.0 \pm 0.8$ km s^{-1} and a full width at half maximum (FWHM) of $\Delta V = 22.9 \pm 1.9$ km s^{-1}. Radio continuum images at 1.42 GHz and $\sim 1'$ resolution from the Canadian Galactic Plane Survey (CGPS, Taylor et al., 2003), show filamentary structures extending from a bright complex source. From the appearance of the structure and a kinematic distance estimate, the region appears to be a very large H II region and a major feature in the Perseus spiral arm.

Yet this major Galactic region is unstudied. Suffering heavy extinction in this direction in the Galactic plane, there is no known optical counterpart to CTB 102. The purpose of this study is to determine the basic properties of CTB 102, mainly how large in physical size it is, and how it influences its Galactic environment. In this study new RRL observations toward CTB 102 are presented. RRL observations allow direct velocity measurements, and along with continuum observations can reveal the density and

temperature of any gas in the beam at or near thermodynamic equilibrium.

3.2 Observations

RRL observations toward CTB 102 were performed with the 100-m NRAO Green Bank Telescope (GBT) during 6 nights in 2006, July 31, August 2-4, 15 & 17. Twelve pointings were observed around the CTB 102 complex. These telescope pointings are illustrated in Figures 3.1 and 3.3. Positions and total integration times for the chosen observations are given in Table 3.1, the observations themselves were divided into 600 s scans. RRLs observed were H103α through H110α. A 50 MHz bandwidth receiver was used to allow the eight recombination lines to be simultaneously observed in the high end of the C-band ($\nu = 4.8 - 5.9$ GHz). Both polarizations were admitted, and the spectrum consists of 4096 channels ($0.62 - 0.75$ km s^{-1} per channel). System temperatures ranged from 19 to 26 K, depending mainly on the elevation of the source. Average system temperatures for each observation are given in Table 3.1. As a check of the system's ability to record RRL emission, the bright "head" of CTB 102 at $\ell = 93\overset{\circ}{.}115$, $b = +2\overset{\circ}{.}835$, hereafter CTB102p, was observed for 600 s at the beginning of each session.

3.3 Data Reduction

None of the eight 50 MHz bands were seriously affected by radio frequency interference. Frequency-switched scans in each linear polarization (YY, XX) were folded individually; since frequency-switching was done in-band ($\pm$12.5 MHz), the effective integration time was doubled. Each 600 s scan contains 16 spectra. To assure that no line structure (e.g., very extended wings from outflows) is removed, velocities forbidden by Galactic rotation (typically -300 km s^{-1} $\leq V_{\rm LSR} \leq -130$ km s^{-1} and $+30$ km

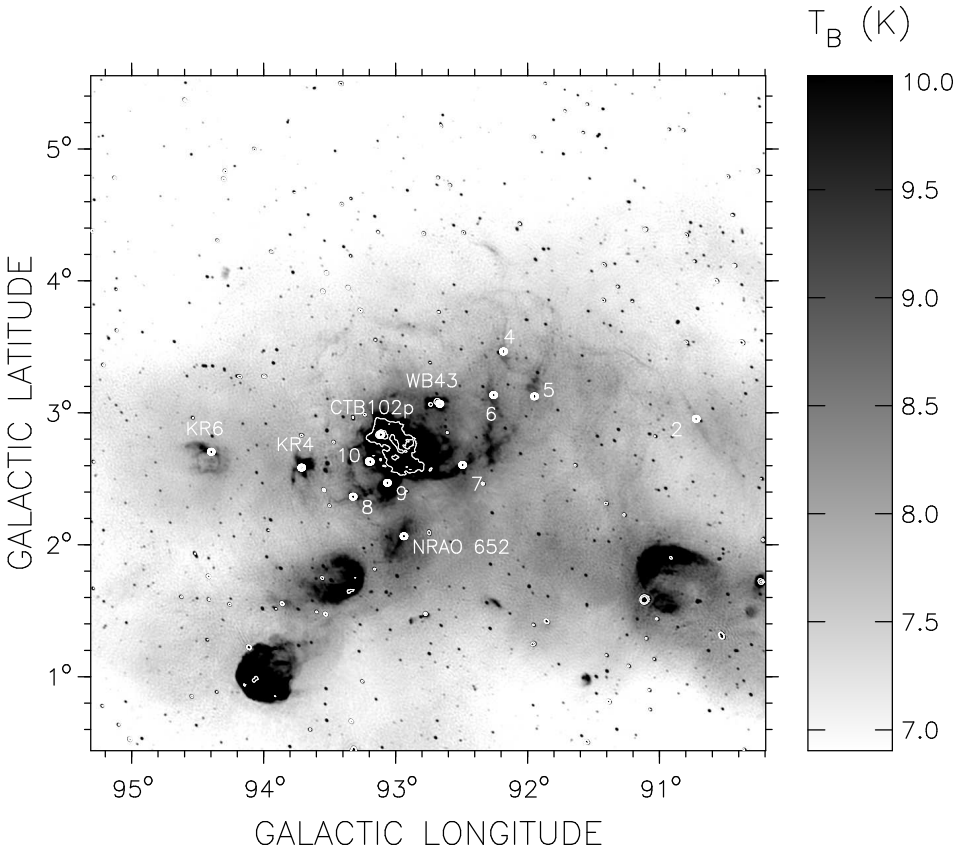

Figure 3.1 CGPS 1.42 GHz continuum image with GBT pointings (see Table 3.1) labelled and displayed as circles. The size of the circles correspond to the GBT beam size, 2.5′. The contours correspond to 15 and 30 K brightness temperature levels.

s^{-1} $\leq V_{\rm LSR} \leq$ +200 km s^{-1}) defines a range of baseline velocities. For each of the 16 spectra in every scan, a baseline was determined using a fourth-order polynomial fitted to the range of baseline velocities. This fitted baseline was then subtracted from every spectrum in each scan. After baseline subtraction, the spectra in the individual scans were combined (for every velocity channel, intensity values were summed up and then divided by the number of scans) to create averaged spectra, one for each line and polarization. At this point in the reduction process, there were 16 spectra (H103α XX, H103α YY, H104α XX, etc.) for every observation in Table 3.1.

Table 3.1 RRL Observations.

Filament/ Object	RA[a] (h m s)	Dec[a] (° ′ ″)	ℓ^a (°)	b^a (°)	Integration time[b] (s)	$\overline{T}^b_{\rm system}$ (K)
CTB102p	21 12 28.9	52 32 23	93.115	2.835	3600	23.7
2	21 01 32.5	50 51 17	90.725	2.955	30000	21.9
4	21 05 19.1	52 17 01	92.185	3.465	14400	21.3
5	21 05 56.4	51 52 53	91.950	3.125	15000	21.0
6	21 07 14.6	52 07 03	92.260	3.135	10200	21.1
7	21 10 48.6	51 55 51	92.495	2.605	3000	21.9
8	21 15 39.9	52 22 03	93.325	2.365	7200	22.4
9	21 13 59.6	52 15 09	93.065	2.470	2400	23.0
10	21 13 49.2	52 27 25	93.195	2.630	600	23.5
KR 4	21 16 24.3	52 48 02	93.715	2.585	3000	22.1
KR 6	21 19 01.0	53 22 26	94.400	2.705	6600	21.5
NRAO 652	21 15 20.1	51 52 56	92.940	2.065	6600	23.5
WB 43	21 09 21.6	52 22 22	92.668	3.069	600	23.9

[a]Positions are J2000.

[b]Integration times and average system temperatures are for the GBT observations.

These averaged spectra were regridded to a common channel width (0.67 km s^{-1}) and smoothed to a common velocity resolution (1.5015 km s^{-1}). Typically 4-10 of these averaged spectra did not show residual wavy baselines in regions of no RRL signal. The only exception was H110α (polarization XX), which showed a very wide "bump" in the spectrum centered around -200 km s^{-1}, extending into the region of the RRL signal. This line and polarization was completely excluded from the analysis. To reduce noise, composite spectra, one for each filament, were made by combining the averaged spectra that did not show residual wavy baselines. The composite spectra typically have a noise level of $\Delta T_{rms} \leq 1$ mK (antenna temperature).

Since RRLs are expected to be quite wide (25–30 km s^{-1}; Lockman, 1989), a spectral resolution of 1.5 km s^{-1} is unnecessarily fine. A higher signal-to-noise ratio can be achieved without loss of information by moderate smoothing of the composite spectra, although too much will add an artificial width to spectral lines present. A resolution of

3.0 km s^{-1} was conservatively chosen.

3.4 RRL Results and Analysis

To the final smoothed composite spectra, Gaussians were fit to obtain spectral line parameters: line amplitude (T_l), central velocity ($V_{\rm LSR}$) and FWHM (ΔV). Smoothed spectra and the Gaussian fits are shown in Figure 3.2 and the obtained parameters are presented in Table 3.2. Note that antenna temperature has been divided by the beam efficiency, $\eta_b = 0.92$ for the GBT at 5 GHz, to convert to brightness temperature. The noise, ΔT_{rms}, was obtained by considering regions on both sides of the line. The $|V - V_{ref}|$ column displays the absolute difference in $V_{\rm LSR}$ for each observed filament/object, compared to CTB102p and rounded to the nearest integer. Figure 3.3 displays the observed velocities of the filaments/objects, overlayed on a CGPS 1.42 GHz continuum image.

Table 3.2 Spectral parameters for each filament/object observed.

Filament/ Object	T_l (mK)	ΔT_{rms} (mK)	$V_{\rm LSR}$ (km s^{-1})	ΔV (km s^{-1})	$\lvert V - V_{ref}\rvert$ (km s^{-1})
CTB102p	102.6 ± 0.4	1.2	-62.66 ± 0.05	18.34 ± 0.08	$\cdots$
2	1.7 ± 0.1	0.3	-78.4 ± 0.6	13.9 ± 1.1	16
4	2.6 ± 0.1	0.6	-67.2 ± 1.3	30.6 ± 2.2	5
5	3.5 ± 0.2	0.7	-51.9 ± 0.9	21.0 ± 1.5	11
6	3.5 ± 0.2	0.6	-67.0 ± 0.8	25.4 ± 1.4	4
7	6.7 ± 0.3	1.2	-57.7 ± 0.8	22.8 ± 1.4	5
8	4.4 ± 0.2	0.7	-56.4 ± 0.7	21.2 ± 1.2	6
9	10.7 ± 0.3	1.1	-66.3 ± 0.5	24.8 ± 0.8	4
10	29.0 ± 0.5	1.5	-65.0 ± 0.2	19.7 ± 0.4	2
KR 4	12.1 ± 0.3	0.9	-67.8 ± 0.4	24.5 ± 0.6	5
KR 6	4.7 ± 0.2	0.7	-56.1 ± 0.5	16.0 ± 0.9	7
NRAO 652	5.7 ± 0.2	0.7	-68.7 ± 0.5	26.0 ± 0.9	6
WB 43	68.9 ± 0.6	1.7	-0.8 ± 0.1	15.3 ± 0.2	62

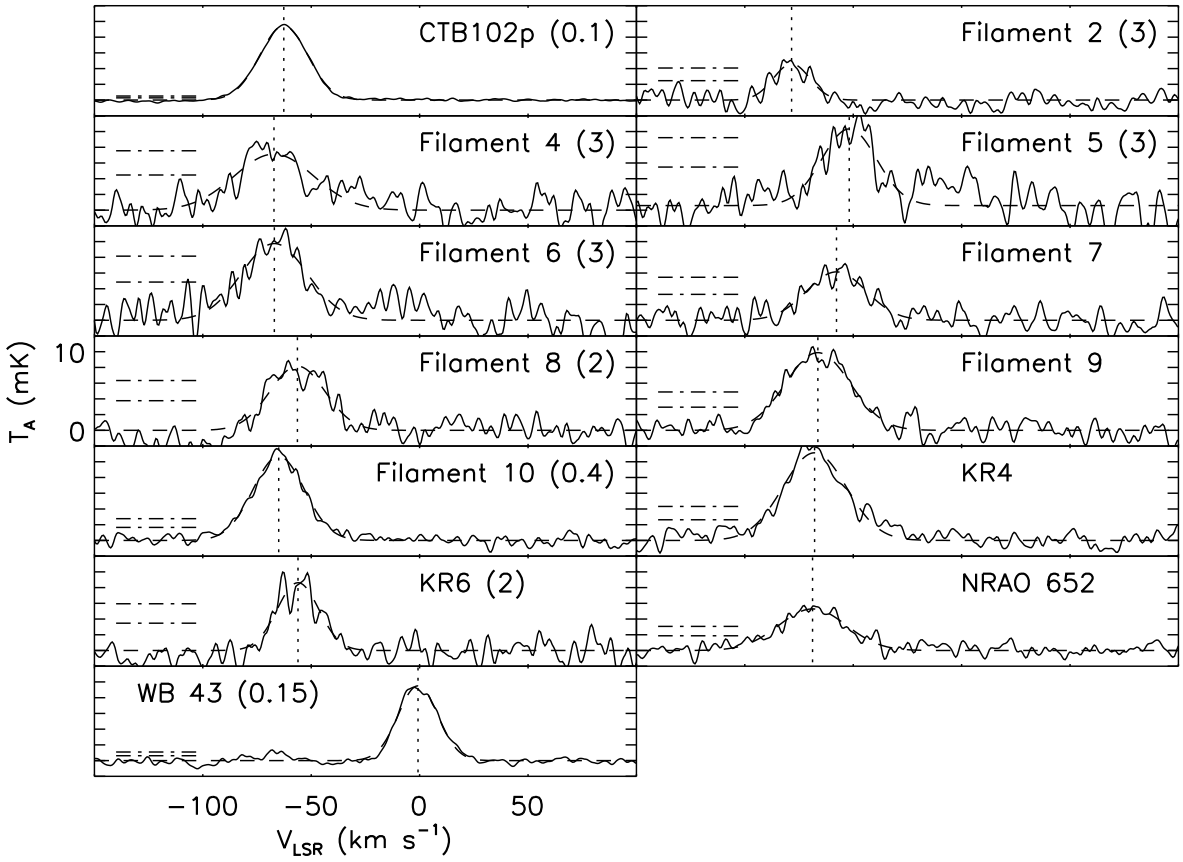

Figure 3.2 Reduced spectra (solid) and Gaussian fits (dashed) for each observation, plotted on the same vertical and horizontal scale. The number in parenthesis is the scaling factor by which the spectrum was multiplied in order to fit the scale. The dash-dotted lines correspond to the 3σ and 5σ noise levels. The vertical dotted line is the central velocity from the Gaussian fit.

3.4.1 Line parameter uncertainties

The line parameter uncertainties in Table 3.2 are obtained in Monte Carlo fashion with IDL (Research Systems, Inc., Boulder) code specifically written for the task of evaluating line parameter uncertainties, see Appendix A. The approach is statistical and attempts to characterize the total uncertainty from two contributions, random noise and fit uncertainties. The routine first takes the reduced spectral line and fits a Gaussian to the observed line using the IDL built-in least squares fit routine. The obtained

parameters are stored. On both sides of the observed line, regions where no line structure is evident are used to characterize the observed noise, ΔT_{rms}. Then, to the originally obtained Gaussian fit, randomly drawn noise from a normal distribution with the same standard deviation as the previously obtained ΔT_{rms} is added. A new Gaussian line profile is then fitted to the generated spectrum. This process is then repeated a number of times with new noise normal distribution added to the originally obtained Gaussian fit each time, to get a standard deviation for each of the fitted parameters. In this study, the standard deviations of the spectral line parameters are extracted after 1000 repetitions. The line parameter uncertainties from the fits themselves are taken as the average values resulting from the 1000 repetitions. They are then combined with the previous standard deviations to produce the total uncertainties. Typically, the two contributions contribute roughly equally to the total uncertainties. The total uncertainties are listed as 1σ in Table 3.2.

3.4.2 Velocities

This study finds that the bright radio source CTB102p has a velocity of $V_{\rm LSR} = -62.66 \pm 0.05$ km s^{-1}, which is 1.7 km s^{-1} less than the value in Lockman (1989). The difference is probably due to the difference in pointing position, as well as the difference in telescope beam size between the studies. The velocity of CTB102p is hereafter referred to as V_{ref}. One purpose of this study is to find out the size of CTB 102, i.e., are the filaments and objects seen around CTB 102 at the same distance? The velocity gradient in this part of the Galaxy is ~ 10 km s^{-1} kpc^{-1}. Looking at the last column of Table 3.2, most filaments and objects have a $|V - V_{ref}| \leq 6$ km s^{-1} , so it seems likely that the CTB 102 complex and objects KR 4, KR 6 and NRAO 652 are in the same part of the Galaxy. In contrast, WB 43 (-0.8 km s^{-1}) is clearly a local H II region, and in no way connected to the CTB 102 complex (Figure 3.2). Filament 2 is another possibly unrelated object (see Section 3.7), its velocity (-78.4 km s^{-1}) deviates the most from

the velocity of CTB102p, $|V - V_{ref}| \sim 16$ km s^{-1}, and is ~ 10 km s^{-1} less than any other velocity observed in this study. Computing the average absolute difference for all observations (except WB 43) yields a result of 6.6 km s^{-1}, but excluding filament 2 from the average, the value drops to 4.3 km s^{-1}.

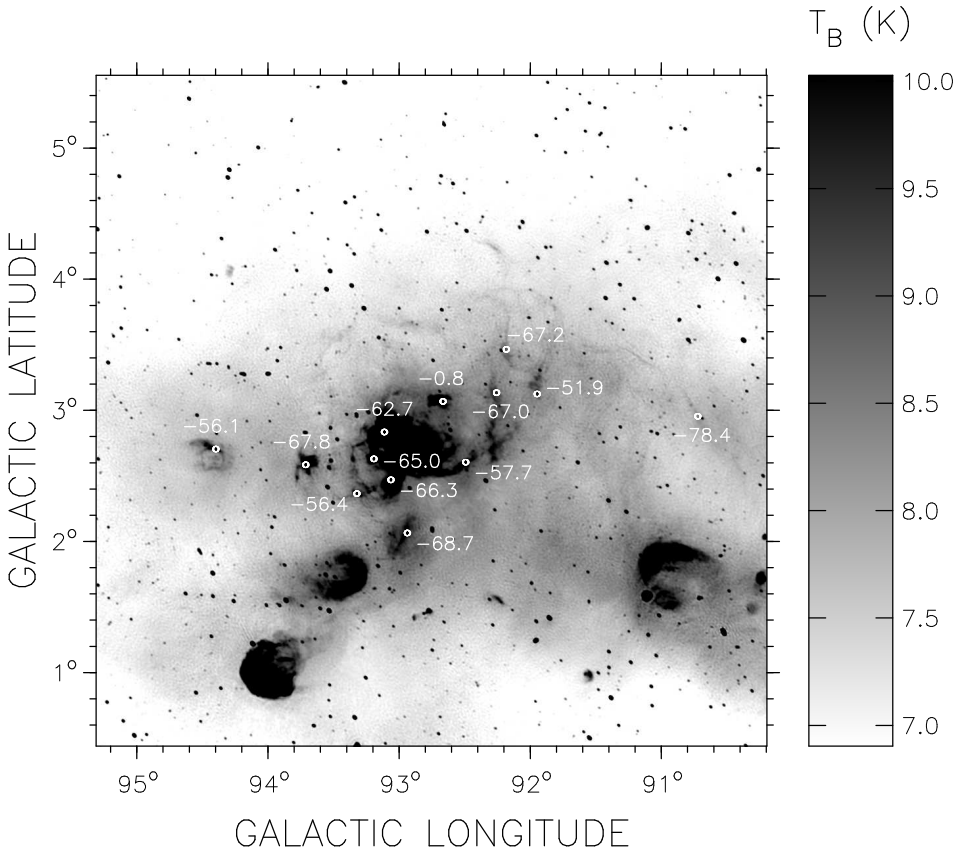

Figure 3.3 As Figure 3.1 but showing the observed velocities for each position.

3.4.3 Line Widths & Electron Temperatures

The majority of FWHMs in this study fall between 20 km s^{-1} and 26 km s^{-1}, which is typical for dense H II regions (Lockman, 1989). The line width of a RRL depends on mainly two things, thermal motion, which is described by the electron temperature (T_e),

and turbulence. Both of these processes produce Gaussian profile shapes, so a Doppler temperature (T_D), which provides an upper limit to the true electron temperature, can be adopted as follows (Rohlfs & Wilson, 2004):

$$\Delta V = 0.21 T_D^{1/2} \tag{3.1}$$

where ΔV is the observed FWHM in km s^{-1} from Table 3.2, corrected for the spectral resolution of 3 km s^{-1}.

The LTE electron temperature can be calculated using the line to continuum brightness ratio:

$$\frac{T_l}{T_c}\left(\frac{\Delta V}{\text{km s}^{-1}}\right) = \frac{6.985\times10^3}{a(\nu,\ T_e)}\left(\frac{\nu}{\text{GHz}}\right)^{1.1}\left(\frac{T_e}{\text{K}}\right)^{-1.15} \times \frac{1}{1+N_{\text{He}^+}/N_{\text{H}^+}} \tag{3.2}$$

where $a(\nu,\ T_e) \simeq\ 1$ and $N_{\text{He}^+}/N_{\text{H}^+} \simeq\ 0.08$ (Rohlfs & Wilson, 2004). The continuum brightness temperature T_c is obtained by convolving the CGPS 1.42 GHz mosaic to the $2.5'$ resolution of the GBT. The background is estimated individually for each filament (typical background estimate uncertainty $\sim$ 0.5 K) and the background is subtracted from the average brightness temperature within a $2.5'$ circle centered on the telescope pointing. Assuming temperature follows the power law $T_{\nu'}/T_\nu = (\nu/\nu')^{-2.1}$ the resulting T_c is scaled using the average frequency of the observed RRLs (5.46 GHz). The parameters derived in this way for each filament/object are in Table 3.3. The T_e is quite sensitive to the estimated background temperature, especially when the peak brightness temperature is barely above the background. The listed uncertainties in T_e comes from considering the uncertainty in the background estimate, 0.5 K. The total uncertainty in T_e is by far dominated by this background uncertainty, the other two contributions (from T_l and ΔV) are both $\simeq$ 10% of the dominant background contribution. Note that $T_D \geq T_e$ within the 1σ uncertainty in all cases. T_D provides a useful upper limit to T_e in case the uncertainty in T_e is large. These derived parameters for the ionized gas gives

an average LTE electron temperature of $\sim 6 \times 10^3$ K. This value falls within the typical range of electron temperatures for H II regions.

The FWHM of CTB102p determined in this study, $\Delta V = 18.34 \pm 0.08$ km s^{-1}, is 4.6 km s^{-1} less than the value for ΔV in Lockman (1989). Again, the difference is probably due to the difference in beam size and pointing position.

Table 3.3 Derived parameters for each filament observed.

Filament/ Object	T_D (K)	T_e (K)
CTB102p	7400 ± 100	5200^{+200}_{-200}
2	4200 ± 600	3400^{+12200}_{-3400}
4	21000 ± 2900	5300^{+3600}_{-4100}
5	9800 ± 1300	6000^{+3800}_{-4300}
6	14400 ± 1500	5000^{+3200}_{-3600}
7	11600 ± 1300	5000^{+1900}_{-2000}
8	10000 ± 1100	8300^{+2900}_{-3100}
9	13800 ± 800	7900^{+1000}_{-1100}
10	8600 ± 300	7700^{+500}_{-500}
KR 4	13400 ± 600	8100^{+900}_{-1000}
KR 6	5600 ± 600	5800^{+3800}_{-4300}
NRAO 652	15100 ± 1000	6000^{+1900}_{-2000}
WB 43	5200 ± 100	5500^{+300}_{-300}

3.5 Distance

With the majority of the filaments' velocities found to be very similar to that of the central body, the whole CTB 102 complex extends about one to two degrees in the sky. In this study, the first ever distance estimate for this H II region is provided.

Figure 3.4 shows a latitude-velocity slice in the direction $\ell \sim 93\overset{\circ}{.}6$, taken from the low-resolution ($36'$) 26-m telescope survey of Galactic plane H I (Higgs & Tapping, 2000). Extensive intermediate velocity ($-90 \leq V_{\rm LSR} \leq -20$ km s^{-1}) H I is seen extending from $-2^\circ \leq b \leq +5^\circ$ in latitude. The H I beyond $V_{\rm LSR} < -20$ km s^{-1} appears split into three concentrations. The lower-latitude concentration at $b = 0^\circ$ and $V_{\rm LSR} = -44$ km s^{-1} blended together with the concentration near $b = +1\overset{\circ}{.}4$ at $V_{\rm LSR} = -68$ km s^{-1} form the Perseus H I arm (see Roberts, 1972, for example). The Cygnus (=Outer) arm is the smaller H I feature up at $b = +3\overset{\circ}{.}6$, $V_{\rm LSR} = -82$ km s^{-1}.

As seen in Figure 3.4, the Perseus arm exhibits a very substantial upward tilt in latitude toward more negative velocities. This is known as the "rolling" motion in this arm. The splitting of the H I Perseus arm into two concentrations has been explained by a spiral shock which is thought to precede the arm (Roberts, 1972). The Cygnus arm appears at higher latitudes than Perseus since it lies further out in the upwardly-warped Galactic disk. The velocity estimated for CTB 102 in H I ($\simeq -58$ km s^{-1}; see Section 3.7) and its latitude ($b = +2\overset{\circ}{.}8$) place it somewhat in the middle of the Perseus arm, in an H I "wall" that connects the two brighter concentrations.

In Figure 3.5 (longitude-latitude), a "mushroom-cap"-like feature centered on CTB 102's coordinates ($\ell = 93\overset{\circ}{.}2$, $b = +2\overset{\circ}{.}8$, $V_{\rm LSR} = -58$ km s^{-1}) appears as a "blister" off of the top of the extensive H I arm at $b = +2^\circ$.

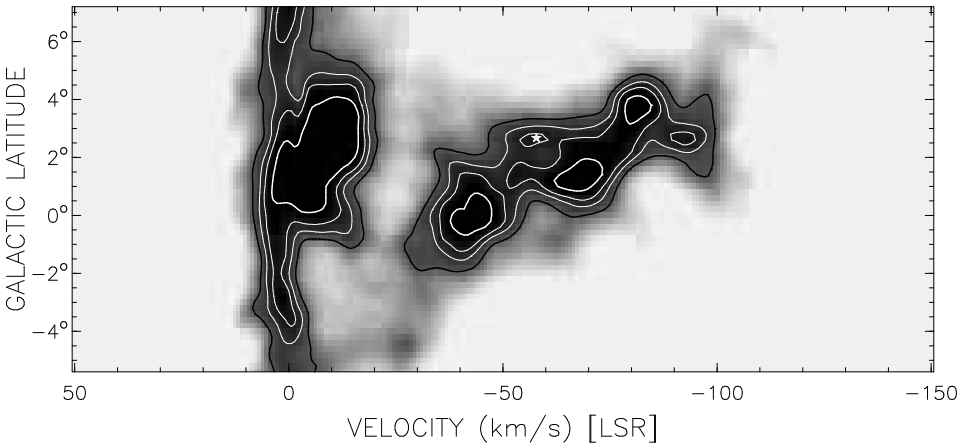

Figure 3.4 $T_B\,(b,\ V)$ (latitude-velocity) centered on $\ell = 93\overset{\circ}{.}6$. The position of CTB 102 is marked with the star symbol. Contours correspond to brightness temperatures at 40, 54, 65 and 80 K.

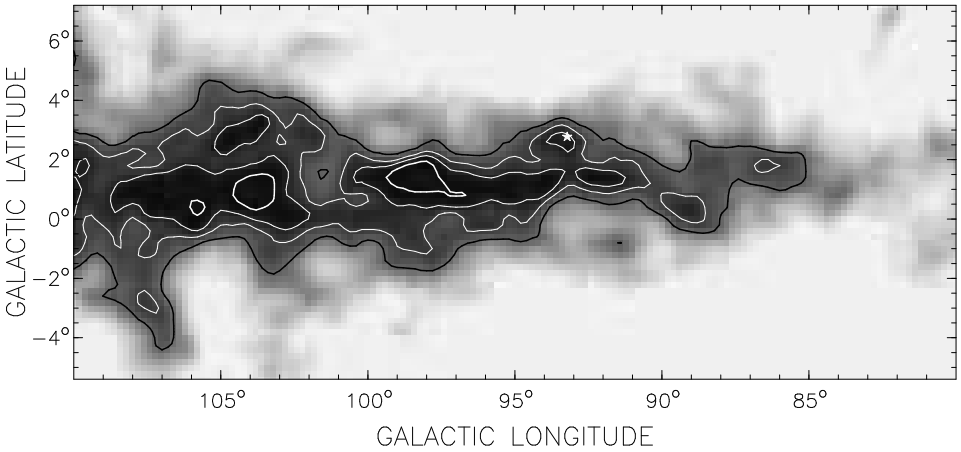

Figure 3.5 $T_B\,(\ell,\ b)$ (longitude-latitude) centered at $V_{\rm LSR} = -58$ km s^{-1}. The position of CTB 102 is marked with the star symbol. Contours correspond to brightness temperatures at 40, 54, 65 and 80 K.

Assuming a flat rotation curve with $R_\odot = 8.0$ kpc and $V_\odot = 220$ km s^{-1}, the velocity of CTB 102 ($V_{\rm LSR} \simeq -58$ km s^{-1}) indicates a rather large kinematic distance of 7.0 kpc (if $R_\odot = 8.5$ kpc, then the kinematic distance is 7.4 kpc). However, this assumes that $V_{\rm LSR}$ derives only from the projection of the object's Galactic circular motion

onto the line-of-sight. Being near a major spiral feature of the Galaxy, like the Perseus arm, CTB 102 is likely influenced by gravitational forces from the stellar component of the arm, so its velocity is likely tainted with non-circular motions such as those from the "rolling" motions in the arms (velocity gradients perpendicular to the plane), and streaming motions from the gravitational influence of density waves.

A kinematic-based distance method for the outer Galaxy that accounts for non-circular streaming motions due to a two-armed density wave has been developed by Foster & MacWilliams (2006). The basic approach is to model the Galactic H I distribution and rotation curve by fitting an empirical model of Galactic structure and density-wave motions to the observations, rather than just assuming a purely circular model. The model assumes only two arms are present in the second quadrant, arranged as a two-armed density wave pattern. A direction near to $b = 0°$ was modeled to ensure that effects from velocity gradients with latitude (i.e., rolling motions, which are not accounted for in Foster & MacWilliams, 2006) are not included. The "rolling" gradient of the H I Perseus arm observed towards CTB 102 is $dV/db \sim -2$ km s^{-1} per degree of latitude. Corrected for this latitude gradient, CTB 102's velocity is $V_{\rm LSR}^{\rm corr} \simeq -52$ km s^{-1}. The velocity field of the best fitting H I model in the direction $\ell = 92\overset{\circ}{.}4$, $b = -0\overset{\circ}{.}2$ is shown in Figure 3.6. The model shows the Perseus arm gaseous density peak (associated with the spiral shock) to be 4.3 kpc distant from the Sun in this direction. The velocity field is ambiguous between $-55 \leq V_{\rm LSR} \leq -44$ km s^{-1} due to the shock, so the heliocentric distance to CTB 102 is either 4.3 kpc or 5.8 kpc.

The farther distance, $r = 5.8$ kpc, is probably not the true distance to CTB 102, as the following discussion will show. Suppose that it is, then for $\ell = 93°$ the galactocentric distance to CTB 102 is $R = 10.1$ kpc (for $R_0 = 8$ kpc). In this direction the Perseus arm shock (which defines where the arm is) is 9.3 kpc from the center. By assuming the arm

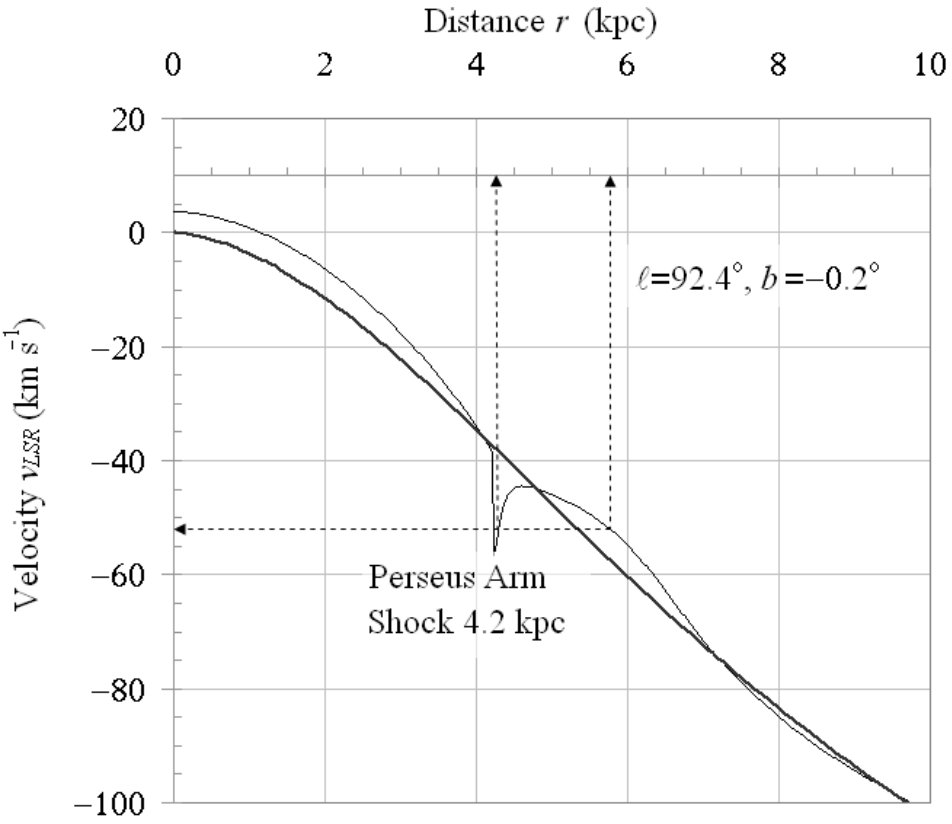

Figure 3.6 Model velocity curve toward $\ell = 92.^{\circ}4$, $b = -0.^{\circ}2$, from the best-fitting model of H I density and kinematics of Foster & MacWilliams (2006). The circular velocity field only (no streaming motions from density waves) is shown by the thick line; with streaming added, the result is the thin line which includes the shock at 4.2 kpc. CTB 102 is found at either 4.3 kpc or 5.8 kpc along the line-of-sight.

is a logarithmic spiral with pitch angle 12°, the intersection of a 10.1 kpc radius circle with the shock is found at a current position of $\phi \approx 5°$. The galactocentric azimuth (ϕ) is defined as zero from the Galactic center to the Sun and related to the longitude ℓ by $\sin\phi = (r/R)\sin\ell$. Thus CTB 102 would have migrated some $\Delta\phi \sim 30°$ beyond the arm, from the formation place to the current position of $R = 10.1$ kpc and $\phi \approx 35°$. How long would it have taken to move this 30° angular distance? For "flat" circular rotation the angular velocity of CTB 102 is $\Omega = 220/10.1 = 21.8$ km s^{-1} kpc^{-1}. The angular speed of the Perseus arm is $\Omega_p =\sim 15$ km s^{-1} kpc^{-1}, a mean between modern estimates near 20 (Martos et al., 2004) and older estimates near 11 (Roberts, 1972) for the Milky Way's spiral arms. Then the time it would have taken CTB 102 to migrate $\Delta\phi$ from the arm at angular rate $\Omega - \Omega_p$ (the relative angular velocity with respect to the arm) is $t = \Delta\phi/(\Omega - \Omega_p) = 75$ Myr. If the massive stars in CTB 102 formed from the compression of the shock, then by now the only ones left would be those that live longer than 75 Myr, or stars of ≤ 7 M$_\odot$ (B5 V types, for example). A cluster of hundreds of such stars would be needed to power CTB 102 ($U = 112$ pc cm^{-2}, see Section 3.6.1). It is highly unlikely that CTB 102 contains stars later than B5 *only*. It is more likely that CTB 102 lies near to the arm/shock, that has a distance of 4.3 kpc in this direction.

From the variation of best-fitting models for the same direction and for models fitted to several immediately adjacent directions, the uncertainty in the distance estimate is ±20% (see Foster & MacWilliams, 2006). This agrees with stellar distances of the nearby H II regions Sh 2-124 and Sh 2-132, both of which are Perseus arm objects.

3.6 Radio Continuum Analysis

Radio continuum measurements of H II regions can provide a lower limit on the total number of ionizing photons (N_L) and estimates of the average excitation parameter (U). Assuming an optically thin, spherical, constant-density H II region, the equations used are (Rudolph et al., 1996):

$$N_L = 7.5 \times 10^{43} S_\nu d^2 \nu^{0.1} T_e^{-0.45} \text{ s}^{-1} \quad (3.3)$$

$$U = 1.33 S_\nu^{1/3} d^{2/3} \nu^{1/30} T_e^{0.116} \text{ pc cm}^{-2} \quad (3.4)$$

where ν is the frequency in GHz, S_ν is the flux density measured at frequency ν in mJy, d is the distance to the source in kpc, and T_e is the electron temperature in units of 10^4 K. Parameter values used are $\nu = 1.42$ GHz, $d = 4.3$ kpc and $T_e = 10000$ K. Since none of the parameters are very sensitive to T_e, and the uncertainties in Table 3.3 are large, a general value of 10^4 K is used (Rudolph et al., 1996).

The flux density for the considered region is obtained from the CGPS continuum image by using the Dominion Radio Astrophysical Observatory (DRAO) software IMVIEW. A polygon incorporating the region of interest is drawn by eye. The polygon's perimeter defines the background, and a twisted plane is fitted to estimate the background. The flux density with the estimated background subtracted is then used to compute the parameters N_L and U. The biggest contribution to the uncertainty is where to draw the polygon around the region of interest. To estimate this uncertainty, each flux measurement is done ten times, each time with a new polygon drawn. The average value is used to compute the estimated parameters, and the standard deviation is used to estimate the uncertainty in the flux measurement.

3.6.1 CTB 102 Central Region

A representative polygon around the region of interest is shown in Figure 3.7, left. The flux density is measured ten times with results ranging between 28.9 and 36.9 Jy. After subtraction of the flux density from the foreground source WB 43, the average value and 1σ uncertainty in the flux density is 31.3 ± 2.5 Jy, which gives a value of $N_L = (4.5 \pm 1.8) \times 10^{49}$ s^{-1} and $U = 112 \pm 15$ pc cm^{-2}. Almost all the uncertainty in these values comes from the uncertainty in the distance. Comparing the values ($\log N_L = 49.7$) to Panagia (1973) suggests an ionizing flux and excitation parameter corresponding to a O5 V class star. Comparing to Vacca et al. (1996) suggests an O4 V star. However, the 30 K contour in Figure 3.7 shows the brightest parts of CTB 102 being along an arc stretching from CTB102p towards filament 7 (i.e., toward smaller Galactic longitude and latitude). Given this continuum flux distribution, it is more likely that the ionizing flux comes from several stars. In summary, the estimates together with the morphology of the 1.42 GHz continuum emission, suggest that the CTB 102 complex is powered by at least several late type O stars, maybe even an early type O star (since N_L is a lower limit).

3.6.2 Filament 10

Filament 10 looks strikingly circular in the 1.42 GHz continuum image (see Figure 3.7, right) with an angular diameter of $\sim 5'$, yielding a physical size of ~ 6 pc at a distance of 4.3 kpc. The intensity profile, with a rapid fall-off at the edge, strongly suggests the region is ionization bound. As such this filament would not contribute ionizing photons to the larger complex. Drawing a circular polygon around Filament 10 (average background $T_b \simeq 11.1$ K) yields 0.46 ± 0.03 Jy for the flux density (same method for uncertainty estimate as for the whole complex), giving $N_L = (6.6 \pm 2.6) \times 10^{47}$ s^{-1}

($\log N_L = 47.8$) and $U = 28 \pm 4$ pc cm^{-2}. Comparisons suggest an O9.5 V (Panagia, 1973) or an B0.5 V (Vacca et al., 1996) star ionizing the region. For this filament, a single star or a compact cluster of early type B stars are ionizing the probably homogeneous ISM, given the circular radio continuum profile.

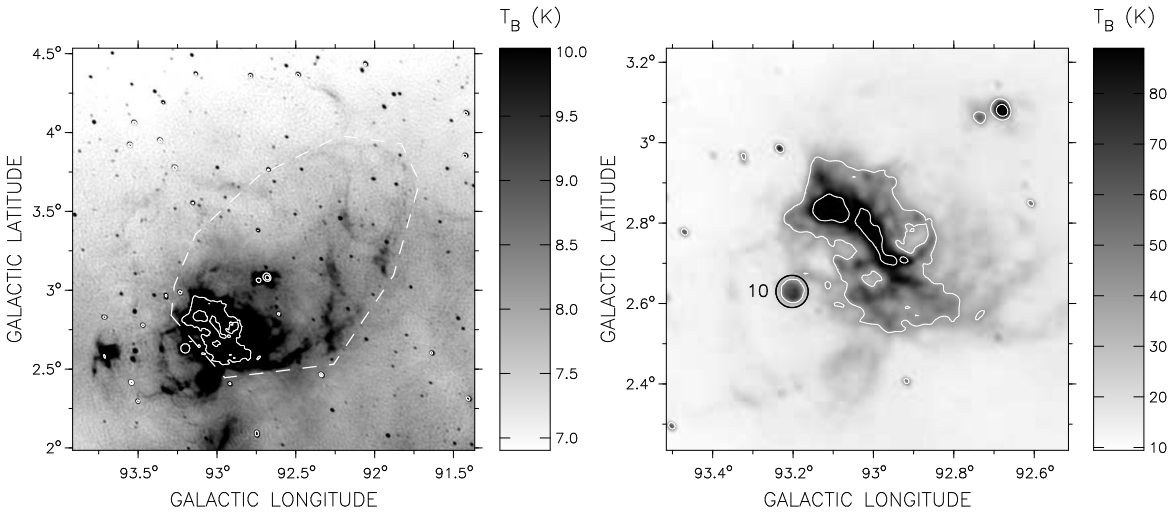

Figure 3.7 Two CGPS 1.42 GHz continuum images of CTB 102 overlayed by contours corresponding to 15 and 30 K. (Left) The dashed polygon is a representative of the polygons used in Section 3.6.1. (Right) The circle indicates the area used for estimates for filament 10 in Section 3.6.2.

3.7 Discussion

This study was partly motivated by the appearance of the CTB 102 region in the 1.42 GHz continuum mosaic (Figure 3.1). Looking at Figure 3.3, one can make out the region looking like a cone-shaped bubble. The radio brightness is concentrated along a ridge following an arc with a maximum at CTB102p. The arc goes toward filaments (in turn) 7, 6, 5, 4 and continues towards greater Galactic latitude, with faint filamentary structures around $b = +4°$ eventually bending back towards greater Galactic longitude and then down. Within this arc, there appears to be a "cleared out" region extending

from the central region of CTB 102 towards greater Galactic latitude and smaller Galactic longitude. The observed velocities for the filaments along this arc all fall within ≤ 11 km s^{-1} of the velocity of CTB102p, indicating that they at least are in the same part of the Galaxy. Taking the velocities and 1.42 GHz continuum image together, it is likely that the CTB 102 complex includes filaments 7, 6, 5 and 4. Filament 2 is probably not part of the region, since its velocity deviates by 16 km s^{-1}, and no obvious association with the other filaments is seen in the radio continuum data. As will be discussed below, the model shows that filament 2 could not be powered by CTB 102.

With the inclusion of these filaments, the angular size of the CTB 102 H II region is $\sim 80'$, which corresponds to a physical size of $\sim$ 100 pc at a distance of 4.3 kpc. Inclusion of filaments 8, 9, and 10, all within ≤ 6 km s^{-1} of CTB102p with apparent connections to CTB 102 in the 1.42 GHz image, increases the angular size of the H II to $\sim 100'$ or $\sim$ 130 pc at 4.3 kpc. The objects KR 4, KR 6 and NRAO 652 have no obvious connection to the region in the radio data, and are probably H II regions which happen to be in the same part of the Galaxy as CTB 102.

If the assumption of the filaments being part of the structure is indeed correct, what sort of process would create such a big H II region? The typical sound speed in a H II region is on the order of 10 km s^{-1}, which is also the typical velocity associated with blister regions and champagne flows (Tenorio-Tagle, 1982). This velocity corresponds to $\sim$ 10 pc/(10^6 yr). The velocity is consistent with the observed velocities in Table 3.2. However, to reach a radius of $50 - 65$ pc ($2R =\sim 100$ or $\sim$ 130 pc) would require a time scale of 5 to 6.5 million years (assuming constant expansion velocity). This time scale is longer than the main-sequence life time of a O5 V star, 3.7×10^6 years (Schaller et al., 1992), but a comparison of the CGPS 408 MHz and 1.42 GHz shows no sign of a supernova in the CTB 102 region. Also, CTB 102 does not appear like a blister in the

1.42 GHz continuum image.

Rather, an alternative interpretation is the whole CTB 102 complex with its filaments is a combination of an H II region with a bubble/chimney structure. A stellar wind from massive O star(s) creates a bubble in the interstellar medium (ISM). Toward a region of the Galaxy with lower density (higher Galactic latitude) the expanding bubble has its top "blown off", creating the possible chimney. Towards regions with higher densities, the expanding stellar wind bubble sweeps up a shell of the ISM. The shell and left over neutral material is exposed to ultraviolet radiation from the O star(s), gets ionized and forms the H II region.

What would be expected if this interpretation is correct? In this picture, the expanding bubble sweeps up a shell of neutral material, leaving a cavity in H I. This shell would be ionized from the inside of the bubble and if viewed through the edge, the increased path length would cause the shell to appear as neutral and ionized filaments. These H I and H II filaments would have observed velocities which do not deviate too much from each other and from the velocity of the central region. Also, the ionized filaments would be expected to be located on the "inside" of the neutral filaments.

Support for the idea comes from viewing the H I structure in the region. Figure 3.8 shows the averaged velocity slices (of width 2.5 km s^{-1}) of the CGPS H I line data, overlaid with contours (15 and 30 K) indicating where the 1.42 GHz continuum flux is located in relation to the H I. A cleared out region is most easily seen in the final three velocity frames (-60.8 to -65.8 km s^{-1}), extending from the central region of CTB 102 towards the Galactic north. This cavity in H I disappears beyond ~ -72 km s^{-1}. The cavity is not the result of the Galaxy running out of gas since in this direction, the Galaxy contains gas out to ~ -100 km s^{-1} (see Figure 3.4). The H I emission

is mostly concentrated along an arc extending from north of CTB 102, wrapping around the "edges" of the H II region and extending more faintly up next to filaments 7, 6 and 4. These H I filaments (seen in the final three velocity frames, -60.8 to -65.8 km s^{-1}) are located on the "outside" of the corresponding H II filaments and they correspond roughly in velocity to the RRL results in Table 3.2. In the first velocity frame, -53.4 km s^{-1}, a filament of H I is spatially coincident with filament 5 (observed $V_{\rm LSR} = -51.9$ km s^{-1}).

Figure 3.9 shows a *MSX* A-band image (8.3 μm, Price et al., 2001) toward CTB 102. The contour corresponds to an averaged CGPS H I brightness temperature level of 70 K from the -55.9 km s^{-1} velocity frame in Figure 3.8. The *MSX* A-band traces PAH emission from neutral material being bombarded with ultraviolet photons. Figure 3.9 clearly shows the morphological association between structures seen in the H I arc discussed above, neutral material in a UV radiation field and the 1.42 GHz continuum emission. This is best demonstrated by the 8.3 μm emission tracing a thin filamentary H I structure which extends from the main H I arc towards CTB102p (i.e., toward greater Galactic longitude and latitude). This thin filament runs parallel to the bright arc seen in the 1.42 GHz continuum image (traced by the 30 K contour in Figure 3.7), something which would be expected if the interpretation of a neutral shell being ionized from slightly above the bright arc is correct.

Could ionizing photons reach the filaments? To reach the inside of the proposed swept up shell at filament 6, ionizing photons have to travel an angular distance of $\sim 50'$ from CTB102p, corresponding to ~ 60 pc at 4.3 kpc. In the bubble scenario, the inside of the bubble is filled with stellar wind, a hot, low density plasma. Absorption in such a plasma is negligible, and the purely geometrically diluted radiation field could easily maintain a high ionization fraction in the ionized inside of the swept up shell. The same

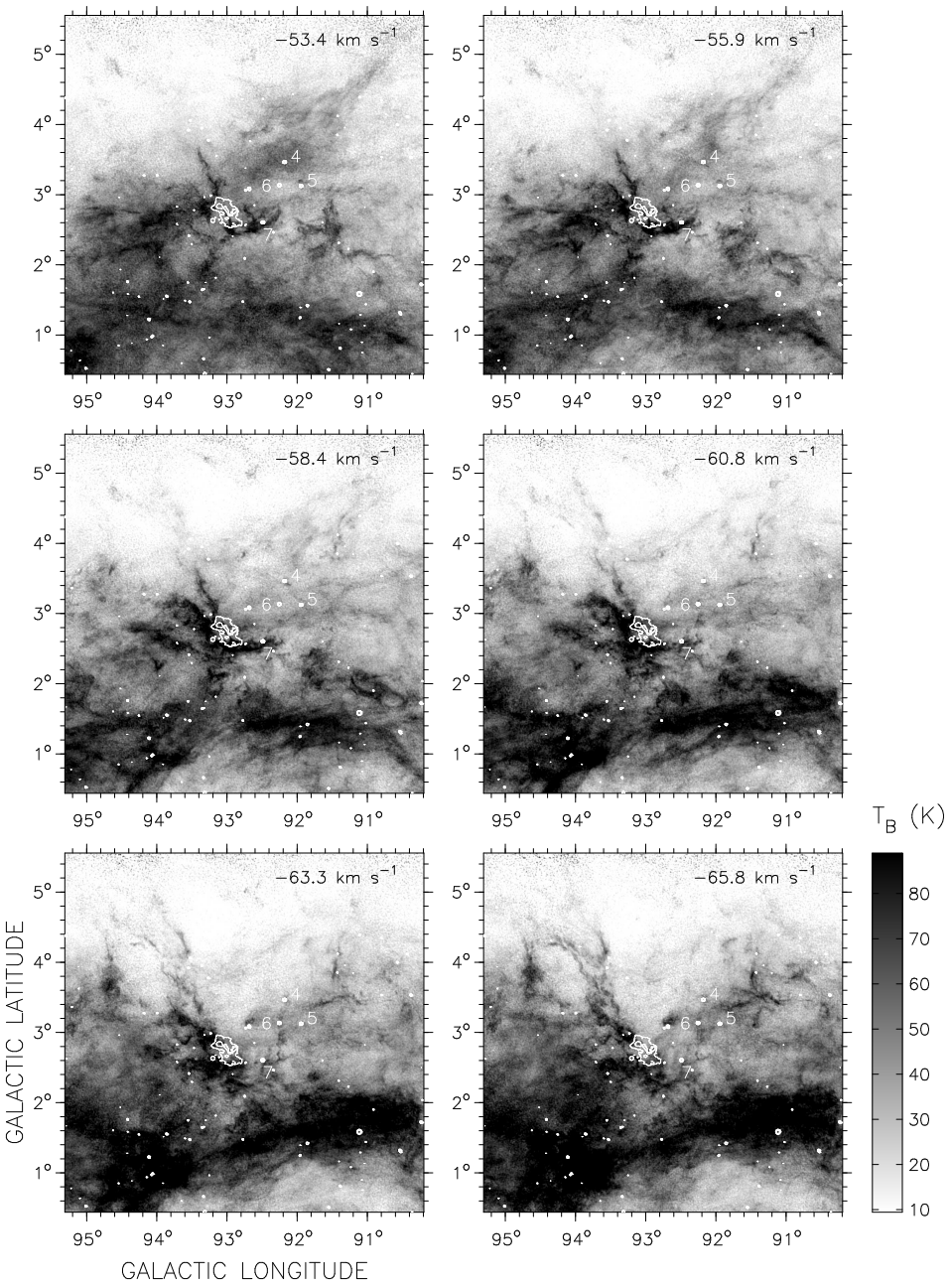

Figure 3.8 CGPS H I line images, averaged over three velocity channels to a width of 2.5 km s^{-1}, centered on the velocities shown in each frame. The white contours correspond to 1.42 GHz continuum brightness temperature levels of 15 and 30 K. The white circles indicate the positions of the GBT pointings for filaments 4, 5, 6 and 7 (from Figure 3.1).

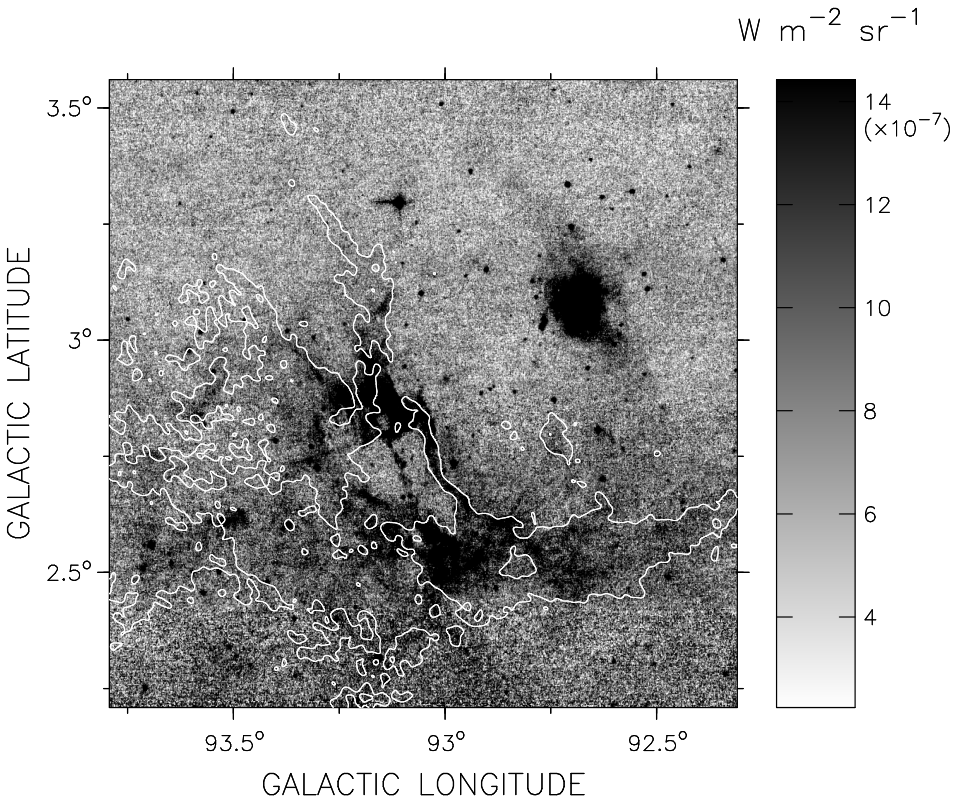

Figure 3.9 *MSX* A-band image (8.3 μm). The contour corresponds to an averaged CGPS H I brightness temperature level of 70 K from the -55.9 km s^{-1} velocity frame in Figure 3.8.

is true for the other filaments we consider part of the shell structure. For filament 2, at a distance of ~ 180 pc from CTB102p ($\sim 140'$), a purely geometrically diluted radiation field could maintain a high ionization fraction if the stellar wind bubble extended all the way out to filament 2. The proposed bubble does not extend that far (see below), and inserting any realistic ISM between the proposed bubble and filament 2 causes significant absorption in the ISM, thus leaving no photons from CTB 102 to ionize filament 2.

A simple analytical model of the development of a stellar wind bubble was given by Castor et al. (1975). Using the formulation in Kwok (2007), the radius (R), shell expansion velocity ($\dot{R}$) and shell fractional thickness ($\Delta R/R$) of such a region are given by:

$$R = 28 \left(\frac{\dot{E}/10^{36} \text{ erg s}^{-1}}{\mu n_0/1 \text{ cm}^{-3}} \right)^{\frac{1}{5}} \left(t/10^6 \text{ yr} \right)^{\frac{3}{5}} \text{ pc} \tag{3.5}$$

$$\dot{R} = 16 \left(\frac{\dot{E}/10^{36} \text{ erg s}^{-1}}{\mu n_0/1 \text{ cm}^{-3}} \right)^{\frac{1}{5}} \left(t/10^6 \text{ yr} \right)^{-\frac{2}{5}} \text{ km s}^{-1} \tag{3.6}$$

$$\frac{\Delta R}{R} = \frac{1}{3} \left(\frac{a_0}{\dot{R}} \right)^2 \tag{3.7}$$

where $\dot{E}$ is the energy loss rate from the star, μ is the mean molecular weight of the medium the shell is expanding into ($\mu = 1.4$ for neutral ISM, $\mu = 0.62$ for a fully ionized ISM), n_0 is the ISM number density and a_0 is the sound speed inside the bubble.

Using a typical mass loss rate of $\dot{M} = 10^{-6}$ $M_\odot$/yr and a stellar wind velocity of $V = 2000$ km s^{-1}, $\dot{E}$ was estimated. The sound speed is $a_0 = 10$ km s^{-1} and the ISM number density is $n_0 = 1$ cm^{-3} (mean ISM density, from Basu et al., 1999). If $\mu = 1.4$ it would take 3.8×10^6 years to reach the position of filament 6 from CTB102p (60 pc), by that time the expansion velocity of the shell will be 9 km s^{-1}. The other extreme, if $\mu = 0.62$, a radius of 60 pc would be reached in 2.8×10^6 years, with a expansion velocity at that time of 12 km s^{-1}. The expansion velocity for both scenarios is fairly insensitive

to large t, and reaches order of magnitude ~ 10 km s^{-1} after roughly 2.5 million years. The estimated thickness of the proposed shell from the 1.42 GHz continuum image and the H I line data is $\sim 6'$, corresponding to a fractional thickness of $\sim 12\%$. The time it takes the model shell to reach such a fractional thickness is 0.9×10^6 years (if $\mu = 1.4$) or 1.3×10^6 years (if $\mu = 0.62$). If instead $n_0 = 10$ cm^{-3} (the rest of the parameters remain the same), time to reach 60 pc increases by a factor of ~ 4. This suggests that if this mechanism is responsible for the observed filaments, the ISM in the direction of decreasing Galactic latitude cannot be more than a few particles per cubic centimeter, or the timescale exceeds the main-sequence life time of the probable star(s).

In the basic model for the expanding swept-up shell, the shell density would be (Kwok, 2007):

$$\rho_s = \left(\frac{\dot{R}}{a_0}\right)^2 \rho_0 \text{ cm}^{-3} \tag{3.8}$$

Estimates of the column density test this picture where the observed filaments are due to our line of sight through the edge of the shell. The maximum path length s looking through the edge of a uniform density spherical shell of radius R and thickness ΔR would be:

$$s = 2R\sqrt{2\left(\Delta R/R\right) + \left(\Delta R/R\right)^2} \tag{3.9}$$

Estimating the column density towards the filaments is done by integrating the CGPS H I line data. The single channel (width 0.82 km s^{-1}) rms noise is 3.3 K, corresponding to a single channel rms noise in the column density of 4.9×10^{18} cm^{-2}. For filament 6, $R = 60$ pc and $\Delta R/R = 0.12$, which gives $s \approx 60$ pc. This is on the order of the radius of the proposed bubble in this direction, so this is probably an upper limit in path length through the edge of any shell associated with CTB 102. The column density through filament 6 is $\sim 10^{21}$ cm^{-2} (making the rms noise negligible). The uniform density needed in a shell to produce such a column density is ~ 5 cm^{-3}. In the model, the

time required to reach this shell density (with $n_0 = 1$ cm^{-3}) is 0.6×10^6 years. Given the large uncertainties of the parameters involved, in R (from the distance uncertainty), ΔR (uncertainty in telling where the filaments start and end) and column density (mainly determining the background), the uncertainty in the shell density can be as large as $\sim 60\%$. Within such a large uncertainty, the model can account for observed column densities within a time frame set by the main-sequence life time of a massive star. However, it cannot be ruled out that the observed filaments are higher density regions in the ISM that happen to be exposed to ionizing photons from the star(s) powering the H II region. Even if that is the case, the medium between the filaments and the powering source would most likely be low density material with a high ionization fraction to allow for enough photons to reach the filaments. Such a medium is consistent with the H I line data and the 1.42 GHz continuum image.

The Castor et al. (1975) model is very basic and does not take into account multiple stellar winds nor non-uniform ISM, but the estimates indicate that the bubble model is a plausible explanation of the size of CTB 102, allowing for observed size, velocities and fractional shell thickness in a time scale of $1 - 2 \times 10^6$ years. That is less than the main-sequence life time of the star(s) that is probably powering the region. For the same reason, it is unlikely that the proposed bubble would reach all the way out to filament 2.

3.8 Conclusions

New RRL observations of CTB 102 were obtained. Analysis show that the filamentary structure surrounding the central region is physically associated with the central region. The first ever distance estimate for this H II region is provided, 4.3 kpc. The

best explanation for the size and appearance of the whole complex is that it is a large H II region combined with a wind-blown interstellar bubble/chimney structure. *MSX*, H I and 1.42 GHz observational data are consistent with this view. The overall morphology of CTB 102 indicates that the proposed H II region/bubble/chimney is a major feature in the Perseus Galactic arm, powerful enough to disrupt the ISM and clear out a $\sim 100 - 130$ pc region. The appearance of CTB 102 in H I with a cleared out region makes the CTB 102 complex comparable in size to the W4 superbubble in the Perseus arm (Normandeau et al., 1996). The W4 superbubble is modeled by Basu et al. (1999) as expanding in a stratified atmosphere. An association of nine O-type stars (IC 1805) is probably the reason for the cavity in H I and the ionization structure of the W4 H II region. CTB 102 shares similarities with W4 in large scale H I distribution and ionization structure.

CHAPTER 4. SUB-MM AND MOLECULAR VIEWS OF GALACTIC HALO H II REGIONS

4.1 Introduction

YSOs are often observed at the peripheries of H II regions, suggesting that star formation can be triggered at such locations (Elmegreen, 1998; Deharveng et al., 2005). This study is aimed at investigating such sites of possible triggered star formation around a sample of so-called halo H II regions. These H II regions have a distinctive ring morphology in Midcourse Space Experiment Galactic Plane Survey (MSX; Price et al., 2001) A-band images filled with radio continuum emission. *MSX* A-band ($\lambda_0 = 8.3$ μm, FWHM $\Delta\lambda = 7 - 11$ μm) emission is dominated by intense line emission from Polycyclic Aromatic Hydrocarbons (PAHs). Photo Dissociation Regions (PDRs) arise in the interface between ionized gas in an H II region and the surrounding molecular material and can be detected through PAH emission. Inside the H II region, the flux of UV photons is sufficiently high to destroy PAHs. Outside of the PAH-free region, e.g., in the PDR, the remaining UV photon flux is insufficiently energetic to destroy PAHs, but it is sufficiently energetic to excite PAHs in a layer surrounding the H II region. This results in a striking ring-like or "halo" morphology. In this interface region, new stars are possibly being formed.

This study means to address the following issues. What are the physical conditions such as mass and column density at the sites of possible star formation? How many

such sites are there? What does the YSO content, if any, look like? This study will look at sub-mm and molecular line observations toward a selected sample of three halo H II regions, KR 7, KR 81 and KR 120. These single star powered regions were chosen to minimize the effects of feedback from multiple massive stars. They were selected based on their appearance in the Canadian Galactic Plane Survey (CGPS, Taylor et al., 2003), displaying the expected roughly circular morphology and size associated with small H II regions. Figures 4.1, 4.2 and 4.3 show *MSX* A-band images of the halo H II regions KR 7, KR 81 and KR 120 respectively (Kallas & Reich, 1980), overlaid with 1420 MHz radio continuum contours. Positions and various other designations of these H II regions are listed in Table 4.1. The *MSX* A-band images have a resolution of 18.3″ and were obtained as part of the Midcourse Space Experiment Galactic Plane Survey (Price et al., 2001). The 1420 MHz radio continuum images were obtained from the CGPS and have a resolution of $\sim 1'$.

In addition, these new data will be combined with data on KR 140, another small halo H II region that has been the subject of several studies (Kerton et al., 1999; Ballantyne et al., 2000; Kerton et al., 2001, 2008). This larger sample will be contrasted with sub-mm observations of a very different environment, the interface between the massive star-forming complex W3 and its surrounding molecular cloud.

Table 4.1 Table of the investigated regions.

Region	RA (h m s)	Dec (° ′ ″)	ℓ (°)	b (°)	Distance (kpc)	Designations/ Associations
KR 7	21 38 17.0	+50 19 48	94.461	−1.549	2.8 ± 0.4^a	Sh 2-124, LBN 426
KR 81	23 39 43.7	+61 54 58	114.600	0.210	1.9 ± 0.4^a	Sh 2-165, LBN 565
KR 120	01 22 58.0	+61 48 16	126.647	−0.840	1.44 ± 0.26^b	Sh 2-187, LBN 630

Coordinates are J2000

[a]From Foster & Routledge (2003)

[b]From Russeil et al. (2007)

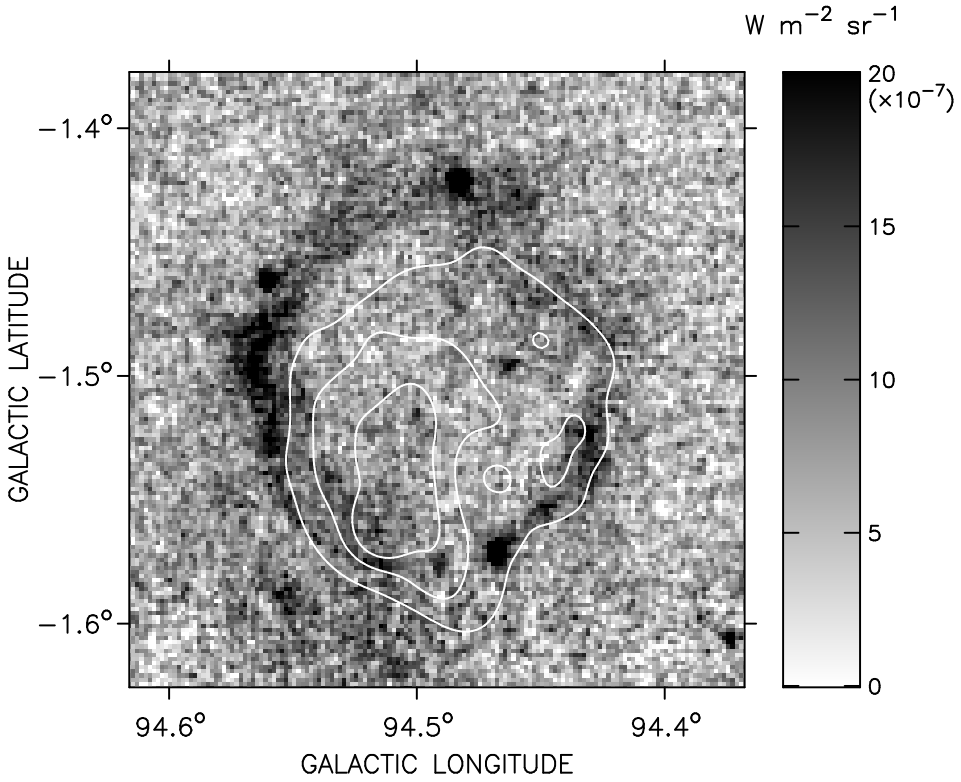

Figure 4.1 *MSX* 8.3 μm image of KR 7. The white contours correspond to CGPS 1420 MHz continuum brightness temperature levels of 11, 13 and 15 K.

4.2 Observations

4.2.1 Sub-mm observations

The sub-mm observations were obtained using the Submillimeter Common-User Bolometer Array (SCUBA) on the 15-m James Clerk Maxwell Telescope (JCMT) at Mauna Kea, Hawaii. SCUBA was used to acquire 450 μm and 850 μm images during 11 nights in 2003, August 12, 15 and 17, September 17 and 25-26, October 4 and October 9-11. The beam can be approximated as a Gaussian with a FWHM of about 8″ at 450 μm and 15″ at 850 μm. The solid angle of the main-beam ($\Omega_{\rm MB}$) can be calculated using the standard formula $\Omega_{\rm MB} = 1.133\theta^2_{\rm FWHM}$.

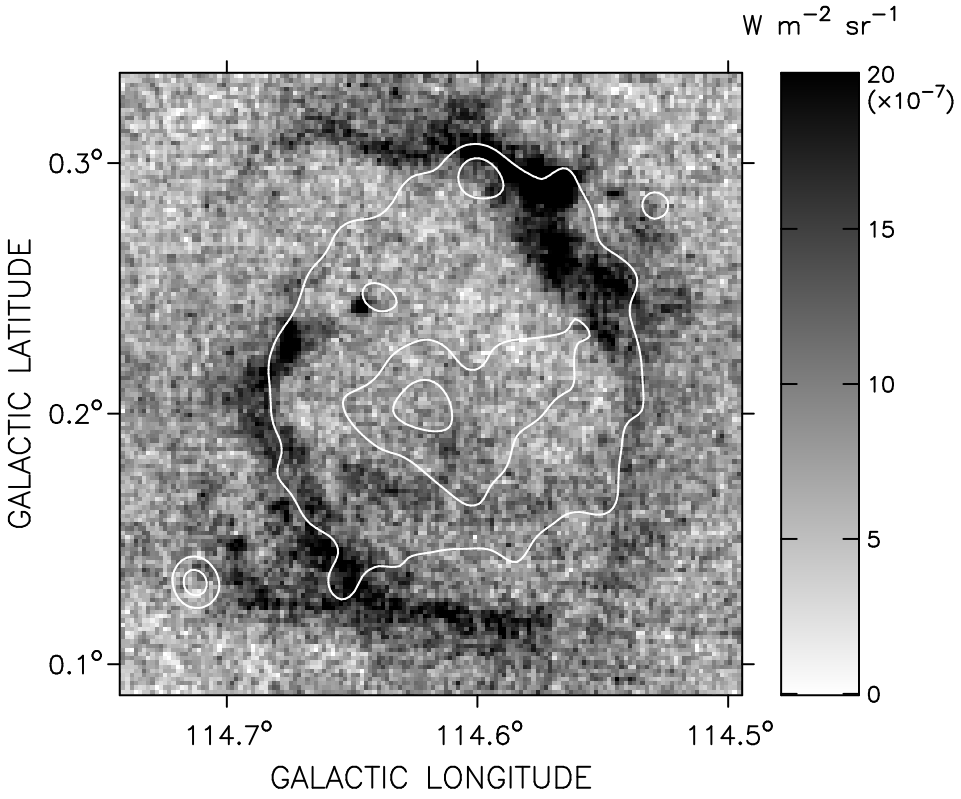

Figure 4.2 *MSX* 8.3 μm image of KR 81. The white contours correspond to CGPS 1420 MHz continuum brightness temperature levels of 7, 8 and 9 K.

4.2.2 Molecular observations

Observations of CO ($J = 1 \rightarrow 0$) line emission from the isotopes ^{12}CO (115.3 GHz), ^{13}CO (110.2 GHz) and C^{18}O (109.8 GHz) were obtained using the SEcond QUabbin Optical Imaging Array (SEQUOIA) at the FCRAO 14-m telescope in Massachusetts. The reduction, calibration and processing of the raw data into science-ready data cubes was done by C. Brunt in 2004. The molecular line cubes have a spectral resolution of 0.25 km s^{-1} and an angular resolution of 46″.

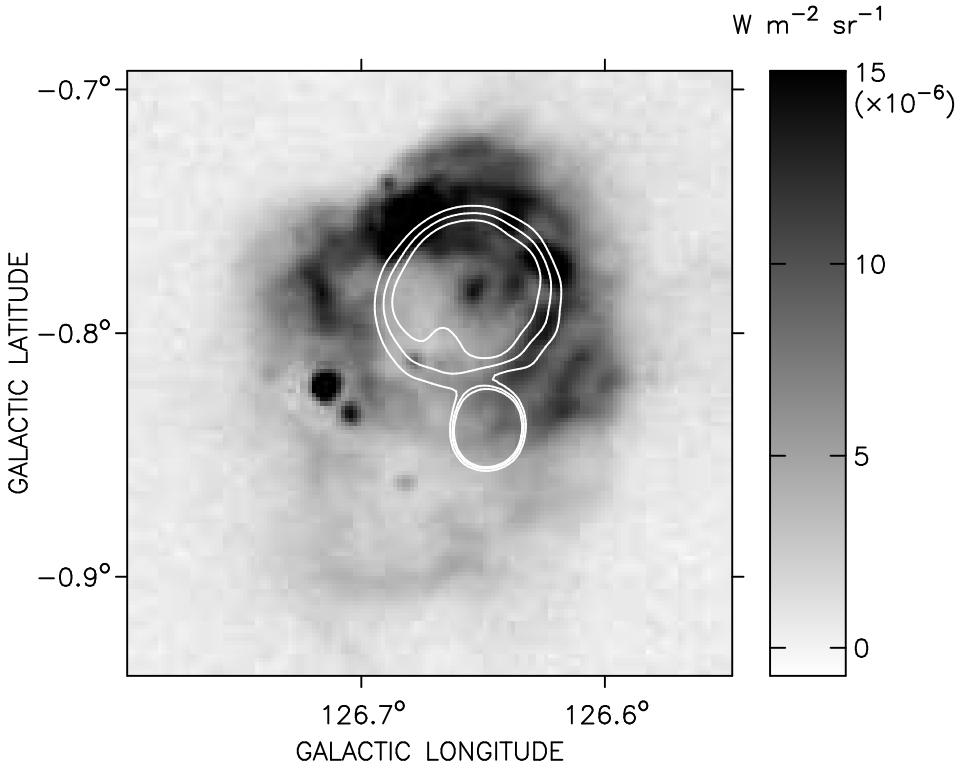

Figure 4.3 *MSX* 8.3 μm image of KR 120. The white contours correspond to CGPS 1420 MHz continuum brightness temperature levels of 10, 12 and 14 K.

4.3 Sub-mm Reduction

The reduction was performed following the SCUBA map reduction cookbook[1]. Standard commands within the SCUBA reduction package SURF were used to apply flat fields, correct for the signal attenuation in the atmosphere, remove spikes, remove base lines, identify noisy bolometers and remove sky noise. For the observations at 450 μm, the weather was too poor and no sources could be seen in the images. These 450 μm observations have been excluded from further study. An example of a reduced, un-calibrated 850 μm image is shown in Figure 4.4. The individual reduced 850 μm images were calibrated into Jy beam^{-1} using the primary calibration source Uranus. To account for the varying background, seen as the large dark and light patches in Figure 4.4, the

[1]http://docs.jach.hawaii.edu/star/sc11.htx/sc11.html

reduced and calibrated images were smoothed to a resolution of 120″. The smoothed images were then subtracted from the reduced and calibrated images, thus removing large-scale structure (> 120″). The background-subtracted images of the same target were then co-added to reduce the noise level. The resulting final background-subtracted images were then used in the subsequent analysis. They have noise levels of $0.07 - 0.04$ Jy beam^{-1}.

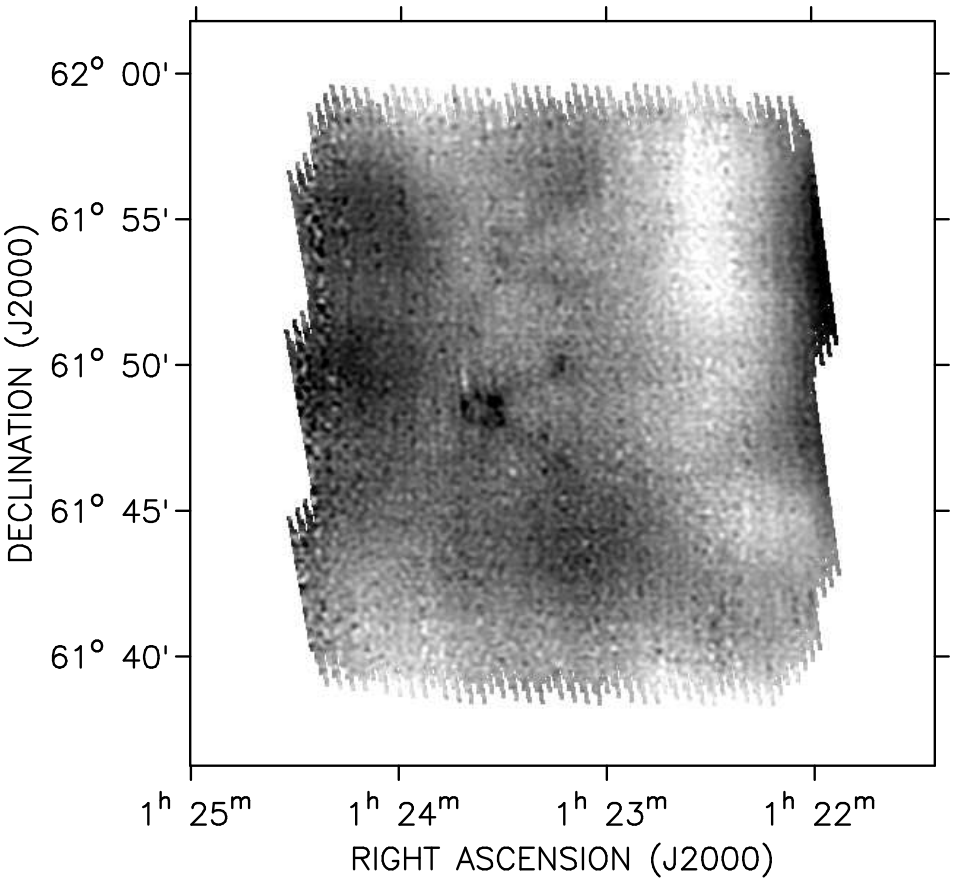

Figure 4.4 Example of single, un-calibrated, non-background subtracted 850 μm image of KR 120. The grey scale goes from -0.006 Volts (white) to 0.006 Volts (black).

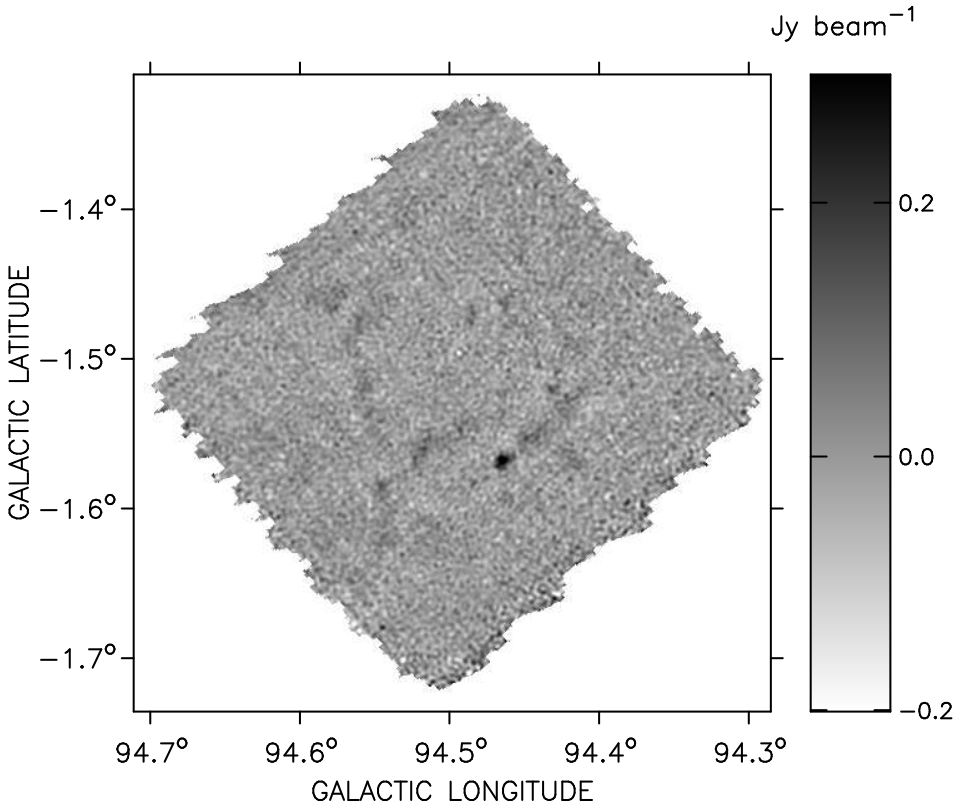

Figure 4.5 Final 850 μm image of KR 7.

4.4 Analysis

Figures 4.5, 4.12 and 4.19 show the 850 μm images of KR 7, KR 81 and KR 120 respectively. They each have one prominent 850 μm source that is located on the "rim" seen in the *MSX* images. Faint extended sub-mm emission can sometimes be seen, it usually lines up with *MSX* emission. This faint emission could be possible clumps, but are ignored in this study. The results of the analysis are listed in Table 4.2.

4.4.1 KR 7

For KR 7, the associated CO emission peaks around −43 km s^{-1} and is mainly found to the Galactic west (smaller Galactic longitude) of the halo H II region, see Figure 4.6. There is also a smaller CO concentration to the Galactic northeast of the H II

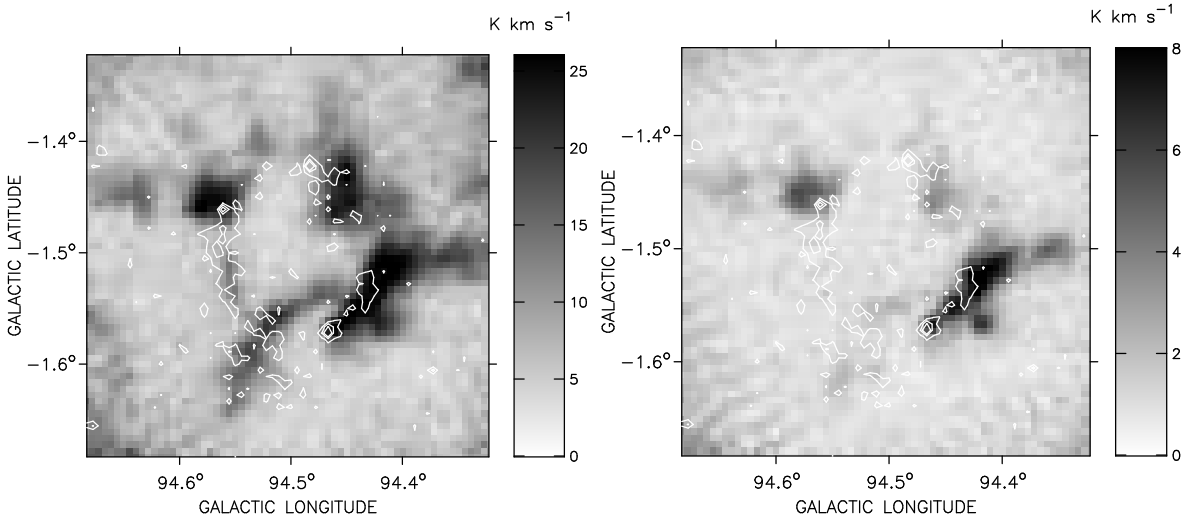

Figure 4.6 Integrated ^{12}CO (left) and ^{13}CO (right) emission around KR 7. The white contours correspond to *MSX* brightness levels of 1.3×10^{-6}, 2×10^{-6} and 3×10^{-6} W m^{-2} sr^{-1} from Figure 4.1.

region. The left panel of Figure 4.6 shows integrated ^{12}CO emission (integrated between $-47.5 < V_{\rm LSR} < -39.5$ km s^{-1}) and the right panel shows ^{13}CO (integrated between $-47.5 < V_{\rm LSR} < -42.8$ km s^{-1}) overlaid with *MSX* A-band contours corresponding to the feature seen in Figure 4.1. For this region and velocity range, C^{18}O barely shows a signal above the noise, even when integrated over a velocity range. C^{18}O analysis is thus not carried out for KR 7. The ^{12}CO and ^{13}CO emission exhibit peaks in the same locations, most notably in a small complex stretching from the location of the sub-mm source up toward the Galactic northwest. This can easily be seen in in the lower right corner of Figure 4.7 that shows the 850 μm images overlaid with ^{13}CO contours. The peak integrated ^{13}CO emission ($I_{\rm peak}$) at the location of the sub-mm source has a value of 7.9 K km s^{-1}, which corresponds to a ^{13}CO-based $N({\rm H_2}) = (5.7 \pm 0.2) \times 10^{21}$ cm^{-2} or $N(M) = 0.026 \pm 0.001$ g cm^{-2}. These quantities were calculated in the same way as in Section 2.5.1. The uncertainties given are due to noise in the maps. This uncertainty is always much smaller than the uncertainty from the assumptions in the method itself. To relate $N({\rm H_2})$ and the integrated ^{12}CO emission, the conversion factor

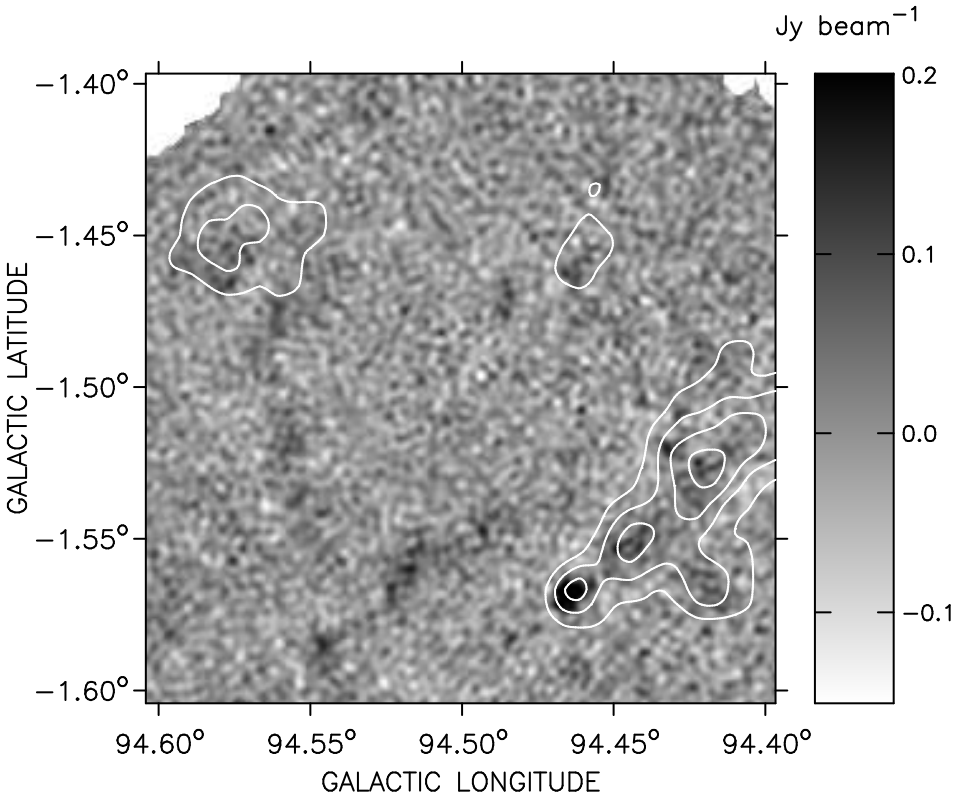

Figure 4.7 Close up view of KR 7 in 850 μm. The white contours correspond to integrated ^{13}CO brightness levels of 3, 5, 7 and 9 K km s^{-1}.

of $X = 2.3 \times 10^{20}$ cm^{-2} (K km s^{-1})$^{-1}$ is used (Rohlfs & Wilson, 2004). By summing over the entire ^{12}CO feature seen in Figure 4.6, the mass of the molecular material surrounding KR 7 is estimated to be ~ 3600 M$_\odot$.

The dominant KR 7 sub-mm source (JCMTSF J213822.5+501908; Di Francesco et al., 2008) has a flux density of 1.1 ± 0.1 Jy within an aperture of 25″ around the peak. The deconvolved radius is $\sim 24''$ and corresponds to a physical diameter of 0.6 pc at a distance of 2.8 kpc. The maximum brightness ($F_{\rm peak}$) is 0.5 Jy beam^{-1} (S/N $\sim$ 13). Using standard conversion factors for SCUBA 850 μm (4.60×10^{22} cm^{-2} (Jy beam^{-1})$^{-1}$ and 6.2 M$_\odot$ Jy^{-1} kpc^{-2} from Table A.1 in Kauffmann et al., 2008) together with an assumed dust temperature $T_d = 20$ K and a distance of 2.8 ± 0.4 kpc (Foster & Routledge, 2003),

$F_{\rm peak}$ corresponds to a dust-derived peak column density of $N(\mathrm{H_2}) = (2.3 \pm 0.2) \times 10^{22}$ cm^{-2} or $N(M) = 0.11 \pm 0.01$ g cm^{-2}. The dust-based column density is greater than the ^{13}CO-based column density for the same location. This could be a result of the ^{13}CO becoming optically thick in the densest regions. The mass of the sub-mm source is 51 ± 15 M$_\odot$, where the listed uncertainty is the combination of the uncertainty in distance and flux density. Dust-based column density and mass estimates are sensitive to the dust temperature. If the dust temperature was instead assumed to be $T_d = 10$ K, the column density would increase to 6.7×10^{22} cm^{-2} or $N(M) = 0.31$ g cm^{-2} and the mass of the sub-mm core would increase to 150 M$_\odot$. Ideally, observations at 450 μm together with 850 μm could give a constraint on the dust temperature. Unfortunately, the 450 μm observations in this study were too affected by bad weather to allow for such an analysis.

In Kerton (2006) KR 7 is listed an 12′ diameter 1420 MHz radio continuum source. The catalogued 1420 MHz flux density is 2690 ± 81 mJy. Using the same technique as in Sections 2.7 and 3.6 to estimate the flux of ionizing photons, the $\log N_L = 48.2$ corresponds to a O9.5 V star (Schaerer & de Koter, 1997) or a B0 V star (Vacca et al., 1996), consistent with observations of an exciting B0 V star (Lahulla, 1985) and with the interpretation of KR 7 as an H II region powered by a single high-mass star.

Figure 4.8 shows an RGB composite image of the region located at the location of the KR 7 850 μm source, made from 2MASS (Skrutskie et al., 2006) J-band (Blue), H-band (Green) and K-band (Red) images. The contours are 850 μm brightness levels of 0.15, 0.3 and 0.45 Jy beam^{-1}, and indicates the very central part of the sub-mm source, seen as the darkest small "blob" in Figures 4.5 and 4.7. A few 2MASS sources are seen within the 850 μm contours. The 2MASS catalog is searched within a radius of $\sim 0.25'$ from the location of $F_{\rm peak}$, an area roughly corresponding to the extent of the 850 μm 0.15 Jy beam^{-1} contour. Within that area, seven 2MASS sources are found.

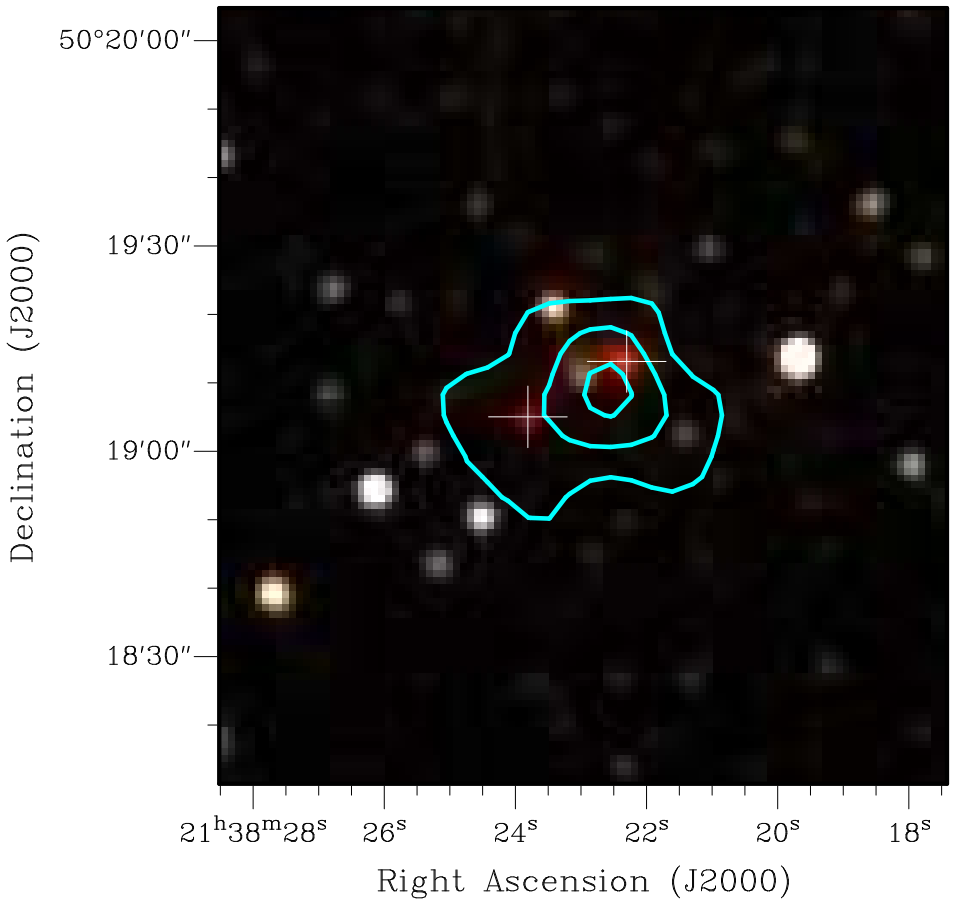

Figure 4.8 Close-up RGB composite of 2MASS J-band (Blue), H-band (Green) and K-band (Red) images of KR 7. The contours correspond to 850 μm brightness levels of 0.15, 0.3 and 0.45 Jy beam^{-1}. The crosses are the two possible embedded YSOs, labeled "3" and "7" in Figure 4.9 and Figure 4.10.

Figure 4.9 shows these sources plotted in a 2MASS color-color diagram. The solid lines in the lower left corner show the intrinsic colors of main-sequence (V) and giant (III) stars (Koornneef, 1983; Bessell & Brett, 1988). The parallel lines show $A_V = 20$ reddening vectors for a K5 V and a O9 V star derived using the infrared extinction law (Rieke & Lebofsky, 1985). The size of the plotted crosses for the 2MASS sources indicate the uncertainty in position in the color-color diagram coming from the uncertainty in 2MASS photometry. An arrow indicates sources where the 2MASS catalog only lists an upper brightness limit in the relevant band. The three sources near the main-sequence

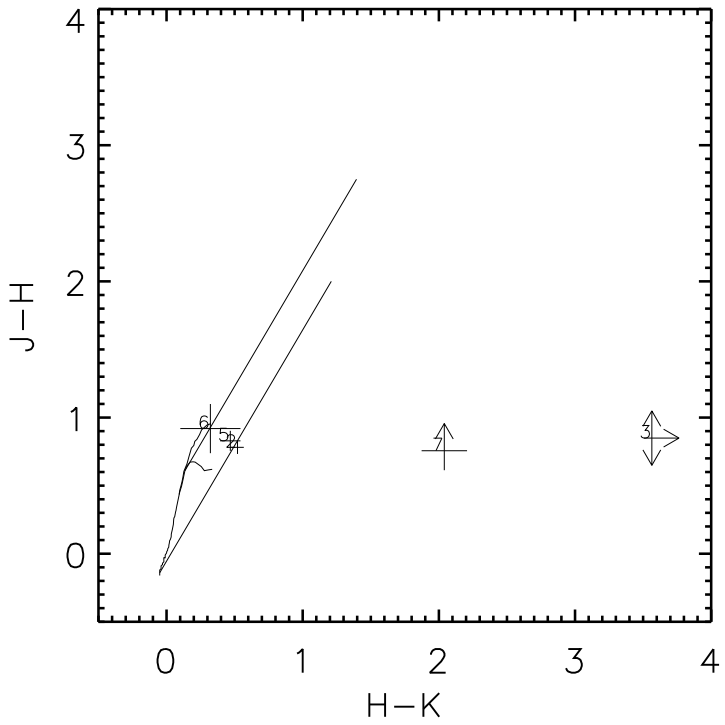

Figure 4.9 Color-color diagram for the 2MASS sources within a radius of $0.25'$ of the KR 7 850 μm source.

line are probably foreground stars. The two sources with $\mathrm{H}-\mathrm{K} \geq 2$ are probably highly embedded YSOs that would be associated with the cold dust core detected in the 850 μm image. Figure 4.10 shows the 2MASS sources plotted in a color-magnitude diagram. The main-sequence and giant branch are shown with some representative spectral types at a distance of 2.8 kpc. The parallel lines are again $A_V = 20$ reddening vectors for a K5 V and a O9 V star. The positions of the 2MASS sources in Figure 4.10 agrees with the conclusions drawn from Figure 4.9.

The KR 7 850 μm source is spatially associated with *IRAS* 21366+5005 and *MSX6C* G094.4674-01.5705. In the *IRAS* PSC, 12, 25 and 60 μm flux densities are listed as being good quality flux densities, while the 100 μm flux density only is an upper limit. In the *MSX6C* catalog, the source is not detected in the bands C (12.1 μm, $11.1-13.2$

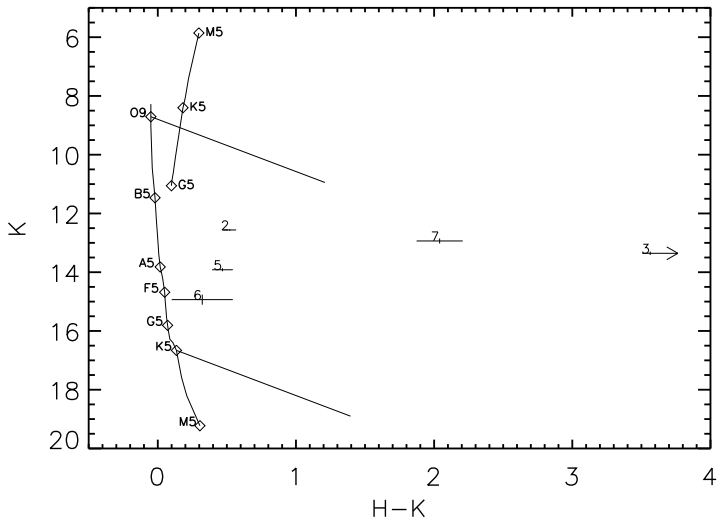

Figure 4.10 Color-magnitude diagram for the 2MASS sources within a radius of 0.25′ of the KR 7 850 μm source.

μm) and E (21.3 μm, $18.2-25.1$ μm), but is is detected in the bands A and D (14.7 μm, $13.5-15.9$ μm). Figure 4.11 shows the spectral energy distribution (SED) of this source from 8.3 to 850 μm. *IRAS* PSC values are squares, *MSX6C* PSC values are diamonds and the 850 μm cross is the 1.1 ± 0.1 Jy found in this work. The arrow indicates an upper limit. Note that in the logarithmic flux density scale, the 1σ uncertainty lines drawn often are smaller than the printed symbol.

4.4.2 KR 81

For KR 81, the associated CO emission peaks around -34 km s^{-1} and is mainly found to the Galactic northwest (smaller Galactic longitude) of the halo H II region, where the prominent sub-mm source is located see Figure 4.13. There is also CO to the Galactic southeast of the H II region. These locations surrounding the H II region are also the locations where the *MSX* A-band emission is the strongest, consistent with a PDR forming in the interface between an H II region and the surrounding molecular material. The left panel of Figure 4.13 shows integrated CO emission from ^{12}CO (integrated between $-37.5 < V_{\rm LSR} < -29.4$ km s^{-1}) and the right panel shows ^{13}CO (in-

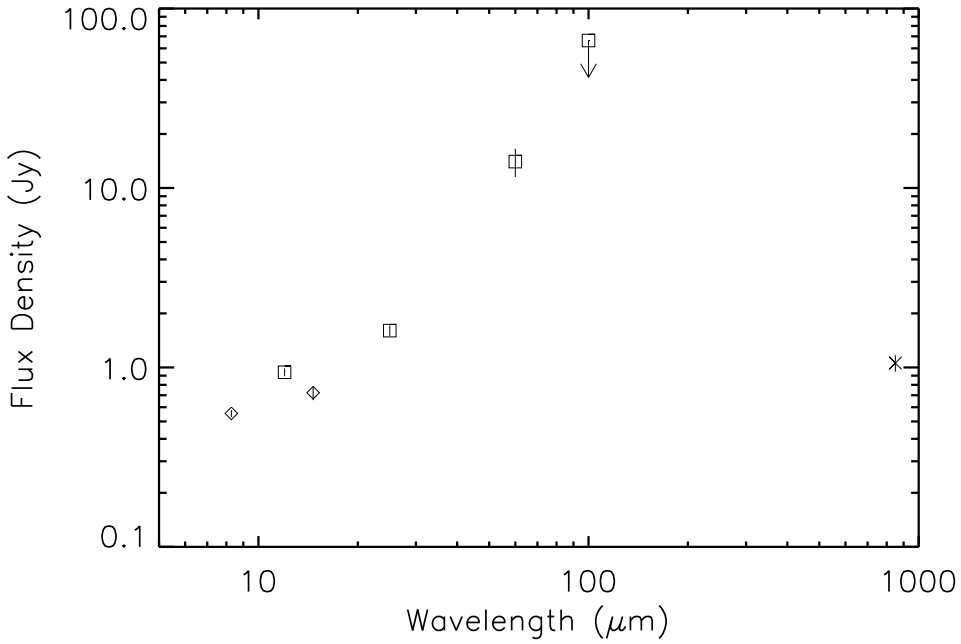

Figure 4.11 Spectral energy distribution for the KR 7 850 μm source.

tegrated between $-35.5 < V_{\rm LSR} < -31.8$ km s^{-1}) overlaid with *MSX* A-band contours corresponding to the feature seen in Figure 4.2. The ^{12}CO, ^{13}CO and C^{18}O emission exhibits peaks in the same locations, most notably in the area surrounding the sub-mm source. This can easily be seen in Figure 4.14, which shows integrated C^{18}O contours overlaid on the 850 μm image. The $I_{\rm peak}$ of the integrated ^{13}CO emission at the location of the sub-mm source has a value of 13.5 K km s^{-1}, which corresponds to a ^{13}CO-based $N({\rm H_2}) = (9.8 \pm 0.1) \times 10^{21}$ cm^{-2} or $N(M) = 0.045 \pm 0.001$ g cm^{-2}. Similarly, using the isotope number ratio R(C^{18}O/H$_2$) = 1.7×10^{-7} (Rohlfs & Wilson, 2004), the C^{18}O-based column density is $N({\rm H_2}) = (1.0 \pm 0.05) \times 10^{22}$ cm^{-2} or $N(M) = 0.045 \pm 0.002$ g cm^{-2}, very close to the estimate from ^{13}CO. By summing over the entire ^{12}CO feature seen in Figure 4.13, the mass of the molecular material surrounding KR 81 is estimated to be ~ 1900 M$_\odot$.

The KR 81 sub-mm source (JCMTSF J233917.8+615914) has a flux density of

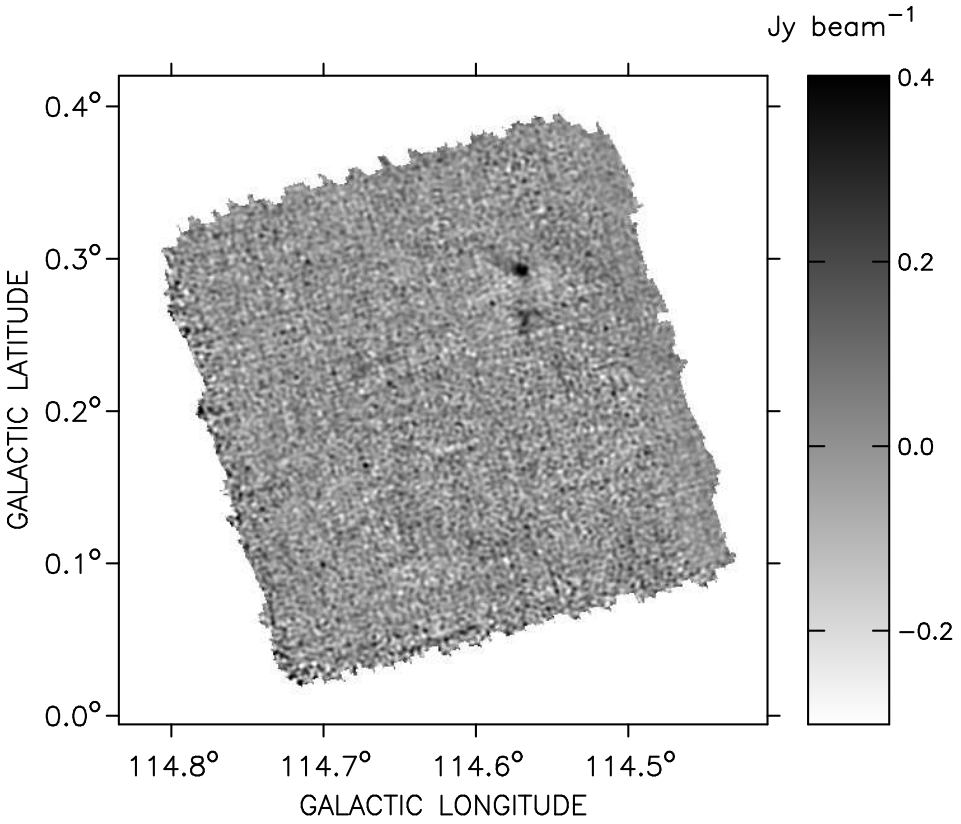

Figure 4.12 Final 850 μm image of KR 81

1.2 ± 0.1 Jy within an aperture of 25″ around the peak. The deconvolved radius is $\sim 24''$ and corresponds to a physical diameter of 0.4 pc at a distance of 1.9 ± 0.4 kpc. $F_{\rm peak}$ is 0.5 Jy beam^{-1} (S/N ratio of ~ 6.7). This corresponds to a dust-derived peak column density of $N(\mathrm{H_2}) = (2.2 \pm 0.3) \times 10^{22}$ cm^{-2} or $N(M) = 0.10 \pm 0.02$ g cm^{-2}. This dust-based column density is greater than the CO-based column density for the same location, again a possible opacity effect. The mass of the sub-mm source is 27 ± 12 $\mathrm{M}_\odot$. If the dust temperature was instead assumed to be $T_d = 10$ K, the column density would increase to 6.4×10^{22} cm^{-2} or $N(M) = 0.30$ g cm^{-2} and the mass would increase to 80 $\mathrm{M}_\odot$.

In Kerton (2006) KR 81 is listed an 6′ diameter 1420 MHz radio continuum source.

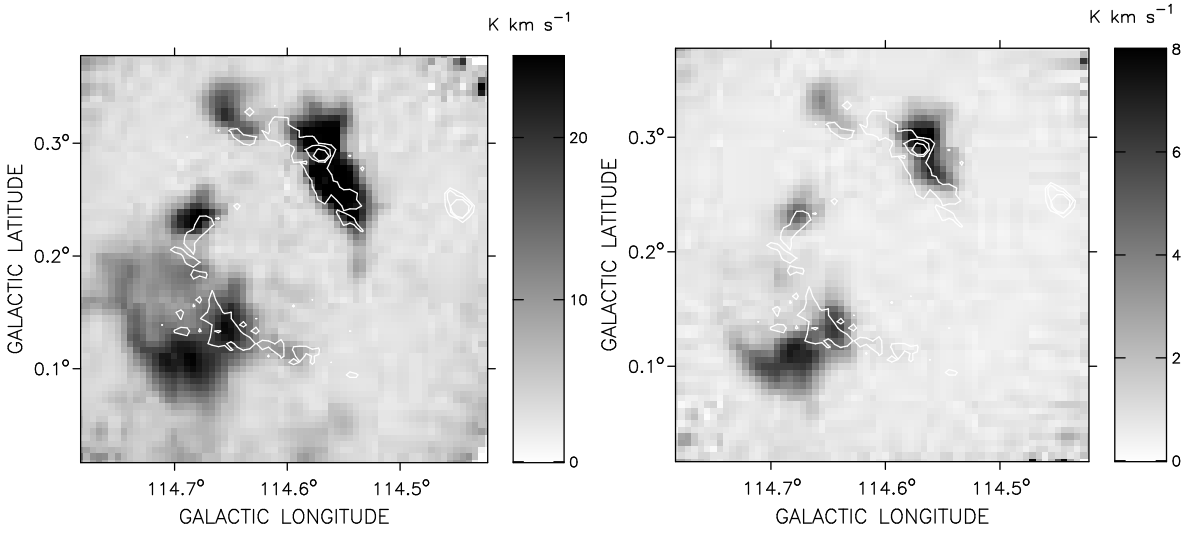

Figure 4.13 Integrated ^{12}CO (left) and ^{13}CO (right) emission around KR 81. The white contours correspond to *MSX* brightness levels of 1.5×10^{-6}, 3×10^{-6} and 6×10^{-6} W m^{-2} sr^{-1} from Figure 4.2.

The catalogued 1420 MHz flux density is 607 ± 40 mJy. The estimated flux of ionizing photons, $\log N_L = 47.2$ corresponds to <B0.5 V star (Schaerer & de Koter, 1997; Vacca et al., 1996).

Figure 4.15 shows an RGB composite image of the region located at the location of the KR 81 850 μm source, made from 2MASS J-band (Blue), H-band (Green) and K-band (Red) images. The contours are 850 μm brightness levels of 0.15, 0.3 and 0.45 Jy beam^{-1}, and indicates the very central part of the sub-mm source, seen as the darkest small "blob" in Figures 4.12 and 4.14. A few 2MASS sources are seen within the 850 μm contours. The 2MASS catalog is searched within a radius of $\sim 0.5'$ from the location of $F_{\rm peak}$, an area roughly corresponding to the extent of the 850 μm 0.15 Jy beam^{-1} contour. Within that area, five 2MASS sources are found. Figure 4.16 shows these sources plotted in a 2MASS color-color diagram, like Figure 4.9. The three sources nearest to the main-sequence/giant branch lines line are probably foreground stars. The two sources with $\mathrm{J} - \mathrm{H} \geq 2.5$, marked with crosses in Figure 4.15, could be background giant stars.

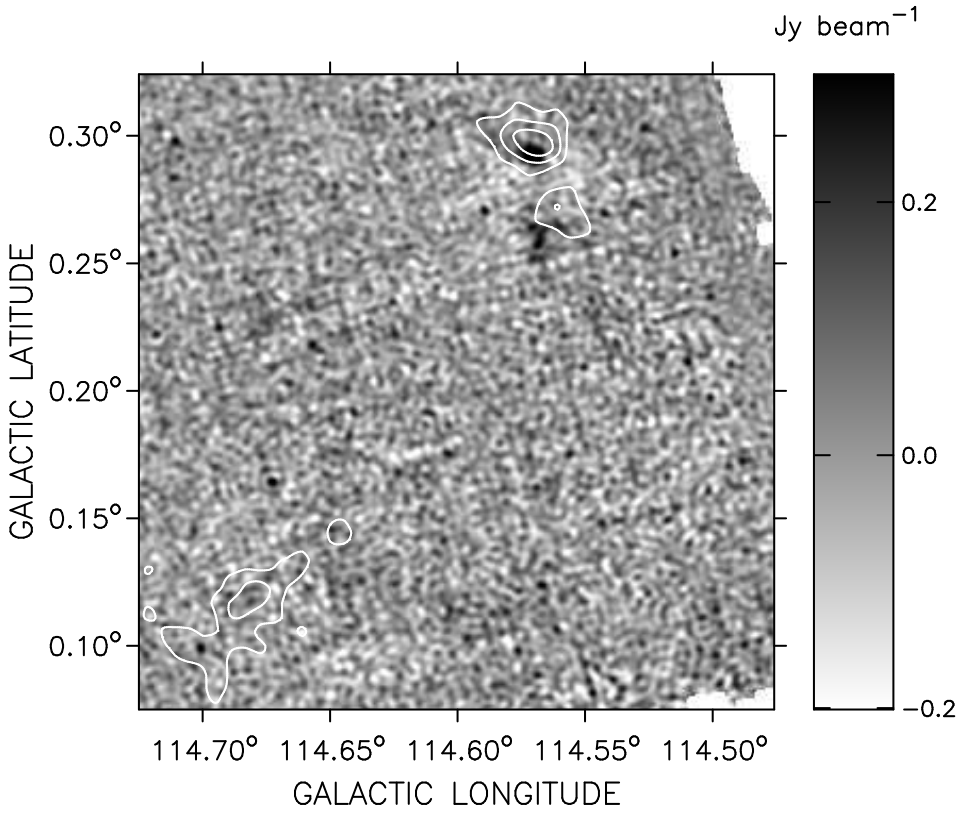

Figure 4.14 Close up view of KR 81 in 850 μm. The white contours correspond to integrated $C^{18}O$ brightness levels of 0.5, 0.75 and 1.0 K km s^{-1}.

Star number 3 in Figures 4.16 and 4.17 is located where a very reddened ($A_V \sim 20$) red giant would be. Star number 2 could be a very reddened Long-Period Variable (LPV) giant star. LPVs are intrinsically very red due to molecular blanketing and cooler continuum temperatures (Bessell & Brett, 1988). No obvious embedded YSO candidates are found in the cold dust core detected in the 850 μm image using 2MASS. Figure 4.17 shows the 2MASS sources plotted in a color-magnitude diagram for a distance of 1.9 kpc and give a picture consistent with the color-color diagram.

The KR 81 850 μm source is spatially associated with *IRAS* 23369+6142 and *MSX6C* G114.5696+00.2899. The *IRAS* PSC entries are all listed as either good or moderate

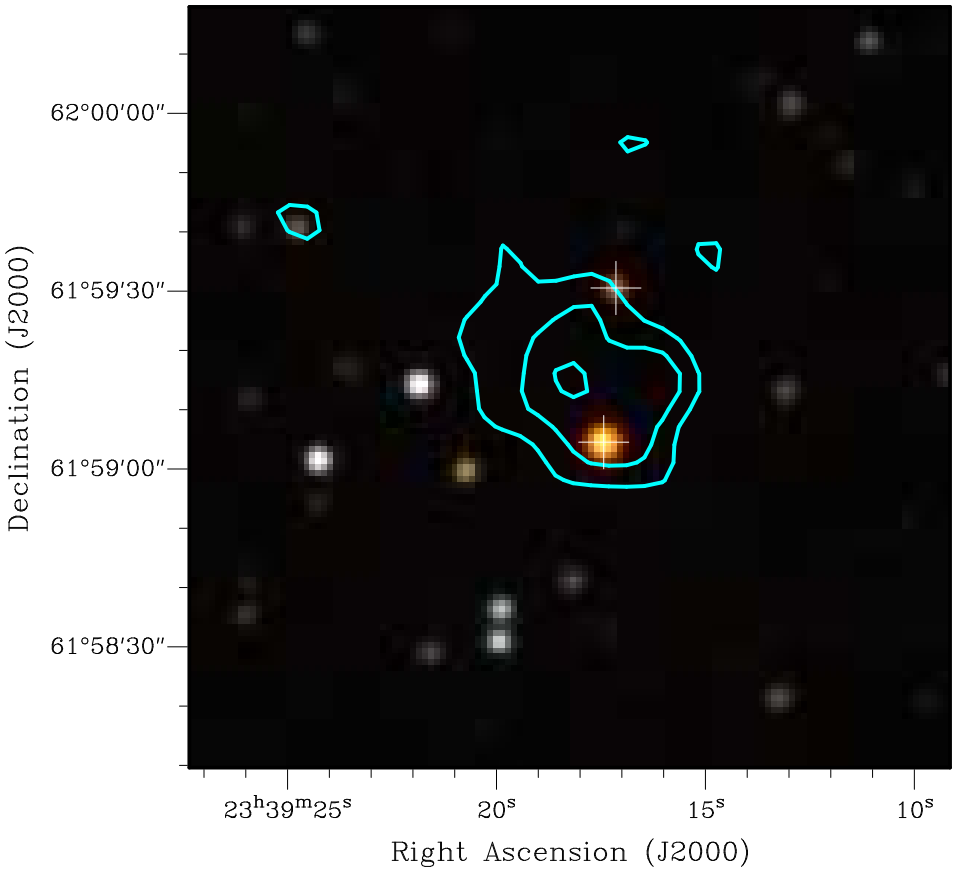

Figure 4.15 Close-up RGB composite of 2MASS J-band (Blue), H-band (Green) and K-band (Red) images of KR 81. The contours correspond to 850 μm brightness levels of 0.15, 0.3 and 0.45 Jy beam^{-1}. The crosses are the two possible background giant stars, labeled "2" and "3" in Figure 4.16 and Figure 4.17.

quality, and the source is detected in all *MSX* bands. Figure 4.18 shows the spectral energy distribution (SED) of this source from 8.3 to 850 μm, like Figure 4.11. *IRAS* PSC values are squares, *MSX6C* PSC values are diamonds and the 850 μm cross is the 1.2 ± 0.1 Jy found in this work.

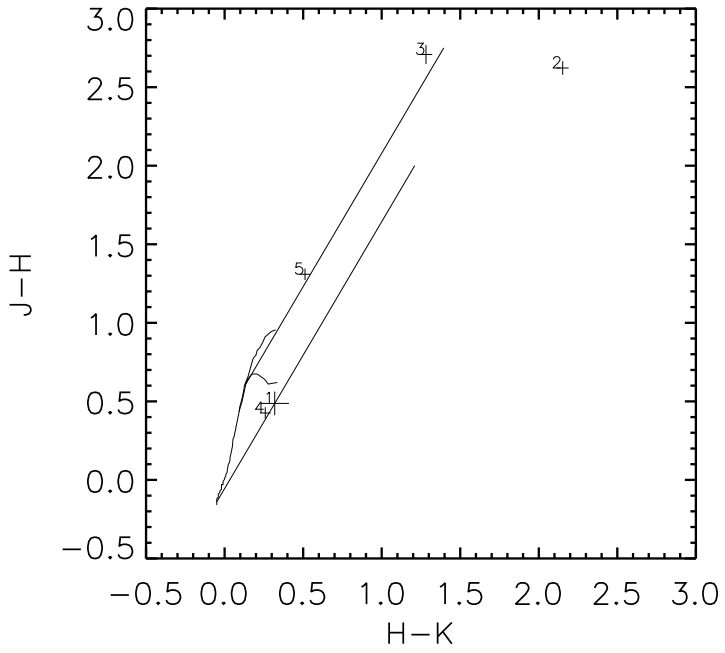

Figure 4.16 Color-color diagram for the 2MASS sources within a radius of 0.5′ of the KR 81 850 μm source.

4.4.3 KR 120

For KR 120, the CO emission associated with the halo H II region has its peak around -15 km s^{-1} and is mainly concentrated on the Galactic east side (larger Galactic longitude), stretching on the outside of the region demarcated by the *MSX* emission and further up toward the Galactic north above the halo H II region. There is also a smaller concentration of CO emission to the Galactic Southwest (smaller Galactic longitude). The left panel of Figure 4.20 shows integrated CO emission from ^{12}CO (integrated between $-18.0 < V_{\rm LSR} < -8.0$ km s^{-1}) and the right panel shows ^{13}CO (integrated between $-18.0 < V_{\rm LSR} < -10.0$ km s^{-1}) overlaid with *MSX* A-band contours corresponding to the feature seen in Figure 4.3. Evidently, even though ^{12}CO and ^{13}CO follow each other fairly well on large scales, the correlation appears to break down for the dense region close to the sub-mm source, where ^{12}CO does not have a peak but ^{13}CO and C^{18}O does. The ^{13}CO and C^{18}O have peaks in the same location as the KR 120 sub-mm

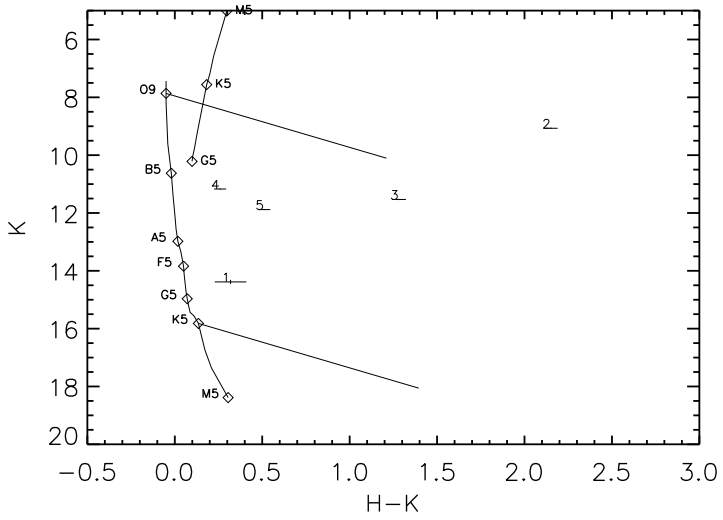

Figure 4.17 Color-magnitude diagram for the 2MASS sources within a radius of 0.5′ of the KR 81 850 μm source.

source. Figure 4.21, which shows integrated $C^{18}O$ contours overlaid on the 850 μm image. The $I_{\rm peak}$ of the integrated ^{13}CO emission at the location of the sub-mm source has a value of 39.6 K km s^{-1}, corresponding to a ^{13}CO-based $N(H_2) = (2.9 \pm 0.05) \times 10^{22}$ cm^{-2} or $N(M) = 0.131 \pm 0.002$ g cm^{-2}. Similarly, the $C^{18}O$-based column density is $N(H_2) = (6.1 \pm 0.2) \times 10^{22}$ cm^{-2} or $N(M) = 0.28 \pm 0.01$ g cm^{-2}, fairly close to the estimate from ^{13}CO. By summing over the entire ^{12}CO feature seen in Figure 4.20, the mass of the molecular material surrounding KR 120 is estimated to be ~ 7600 M$_\odot$.

The KR 120 sub-mm source (JCMTSF J012332.0+614849) has a flux density of 1.6 ± 0.2 Jy within an aperture of 18″ around the peak. The deconvolved radius is $\sim 16''$ and corresponds to a physical diameter of 0.2 pc at a distance of 1.44 ± 0.26 kpc. $F_{\rm peak}$ is 1.5 Jy beam^{-1} (S/N ratio of ~ 23). This corresponds to a dust-derived peak column density of $N(H_2) = (7.0 \pm 0.3) \times 10^{22}$ cm^{-2} or $N(M) = 0.33 \pm 0.02$ g cm^{-2}. This dust-based column density is greater than the CO-based column density for the same location, again a possible opacity effect. The mass of the sub-mm source is 21 ± 8 M$_\odot$. If the dust temperature was instead assumed to be $T_d = 10$ K, the column density would in-

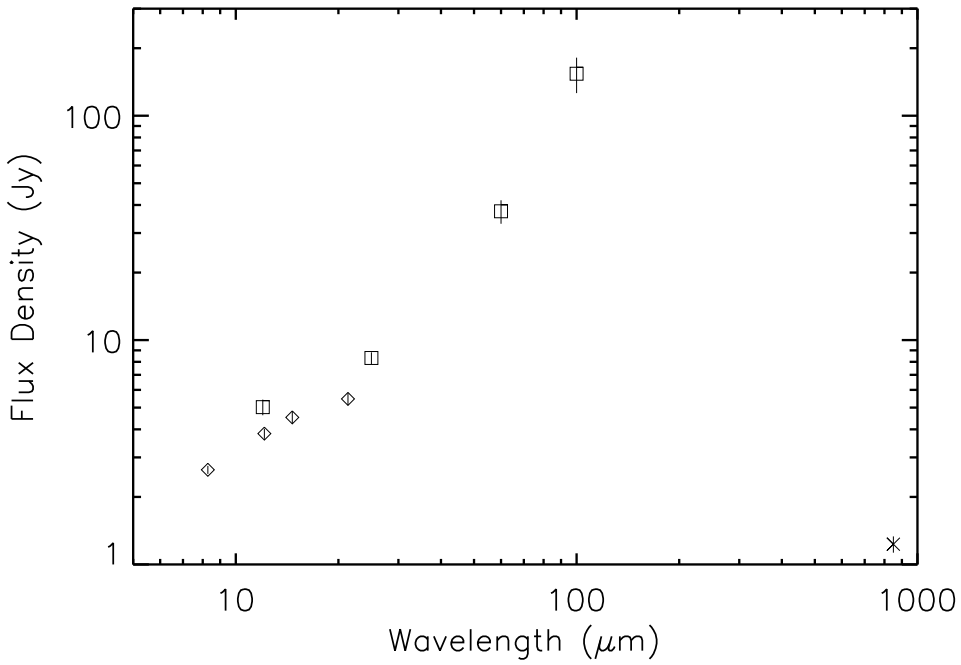

Figure 4.18 Spectral energy distribution for the KR 81 850 μm source.

crease to 2.0×10^{23} cm^{-2} or $N(M) = 0.95$ g cm^{-2} and the mass would increase to 80 M$_{\odot}$.

In Kerton (2006) KR 120 is listed an 6′ diameter 1420 MHz radio continuum source. The catalogued 1420 MHz flux density is 928 ± 28 mJy. The estimated flux of ionizing photons, $\log N_L = 47.2$ corresponds to <B0.5 V star (Schaerer & de Koter, 1997; Vacca et al., 1996). This agrees well with the observation of a B2.5 V star possibly being the exciting star for KR 120 (Russeil et al., 2007).

Figure 4.22 shows an RGB composite image of the region located at the location of the KR 120 850 μm source, made from 2MASS J-band (Blue), H-band (Green) and K-band (Red) images. The contours are 850 μm brightness levels of 0.2, 0.8 and 1.4 Jy beam^{-1}, and indicates the very central part of the sub-mm source, seen as the darkest small "blob" in Figures 4.19 and 4.21. A cluster of 2MASS sources are seen within the 850 μm contours, along with fuzzy NIR emission. The 2MASS catalog is searched

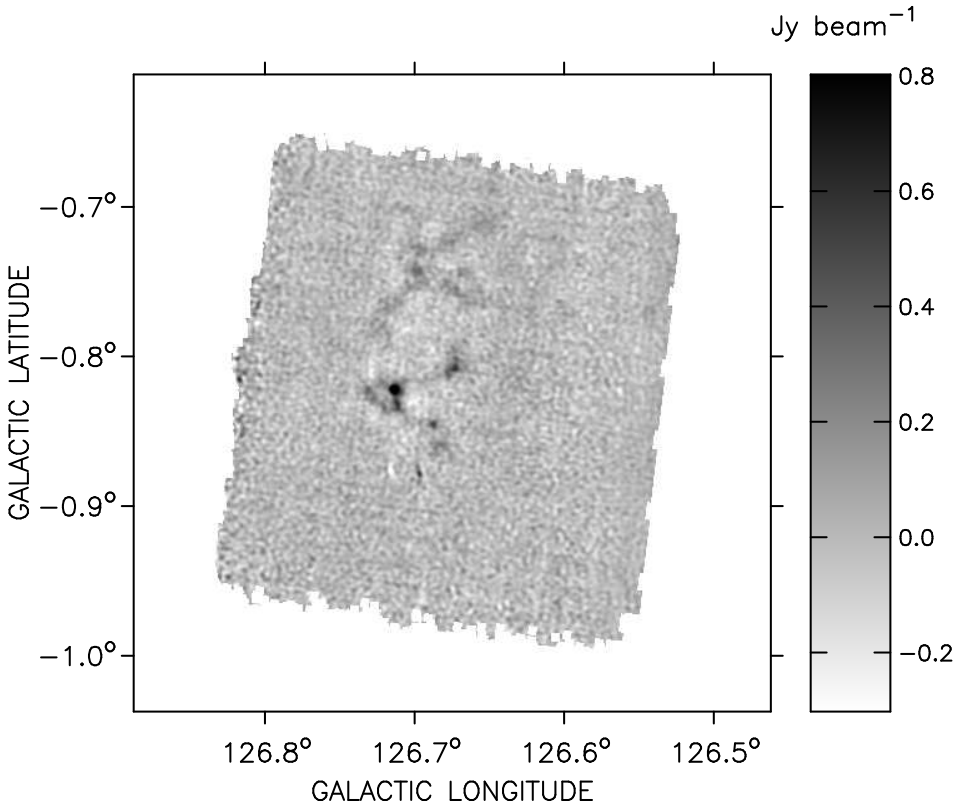

Figure 4.19 Final 850 μm image of KR 120

within a radius of $\sim 0.25'$ from the location of $F_{\rm peak}$, an area roughly corresponding to the extent of the 850 μm 0.2 Jy beam^{-1} contour. Within that area, eight 2MASS sources are found, all of which only have upper limit detections in the J-band. Figure 4.23 shows these sources plotted in a 2MASS color-color diagram, like Figure 4.9. All of the 2MASS sources in the color-color diagram have uncertain locations due to high uncertainty in 2MASS magnitudes, but at least almost all of them have to have $\mathrm{H}-\mathrm{K} \geq 2$. Figure 4.24 shows the 2MASS sources plotted in a color-magnitude diagram for a distance of 1.44 kpc. In Figure 4.24, the sources populate a region where highly embedded intermediate-mass YSOs would be. These sources are likely to be a cluster of YSOs.

The KR 120 850 μm source is spatially associated with *IRAS* 01202+6133 and *MSX6C* G126.7144-00.8220. In the *IRAS* PSC, 12, 25 and 60 μm flux densities are

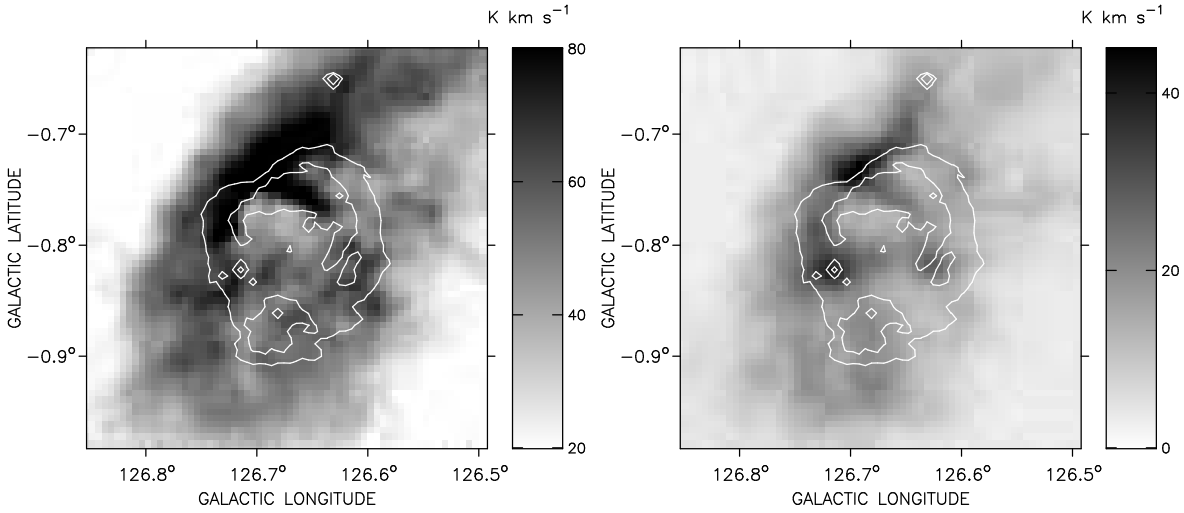

Figure 4.20 Integrated ^{12}CO (left) and ^{13}CO (right) emission around KR 120. The white contours correspond to *MSX* brightness levels of 3×10^{-6}, 1×10^{-5} and 5×10^{-5} W m^{-2} sr^{-1} from Figure 4.3.

listed as being good quality flux densities, while the 100 μm flux density only is an upper limit. The source is detected in all *MSX* bands. Figure 4.25 shows the spectral energy distribution (SED) of this source from 8.3 to 850 μm, like Figure 4.11. *IRAS* PSC values are squares, *MSX6C* PSC values are diamonds and the 850 μm cross is the 1.6 ± 0.2 Jy found in this work. The arrow indicates an upper limit.

Table 4.2 Results of sub-mm and molecular analysis of the 850 μm sources.

Region	$N(M)^a_{\rm peak}$ (g cm^{-2})	$N(M)^b_{\rm peak}$ (g cm^{-2})	$N(M)^c_{\rm peak}$ (g cm^{-2})	Mass^c (M$_\odot$)
KR 7	0.026 ± 0.001	$\cdots$	0.11 ± 0.01	51 ± 15
KR 81	0.045 ± 0.001	0.045 ± 0.002	0.10 ± 0.02	27 ± 12
KR 120	0.131 ± 0.002	0.28 ± 0.01	0.33 ± 0.02	21 ± 8

[a]Based on ^{13}CO
[b]Based on C^{18}O
[c]Based on 850 μm

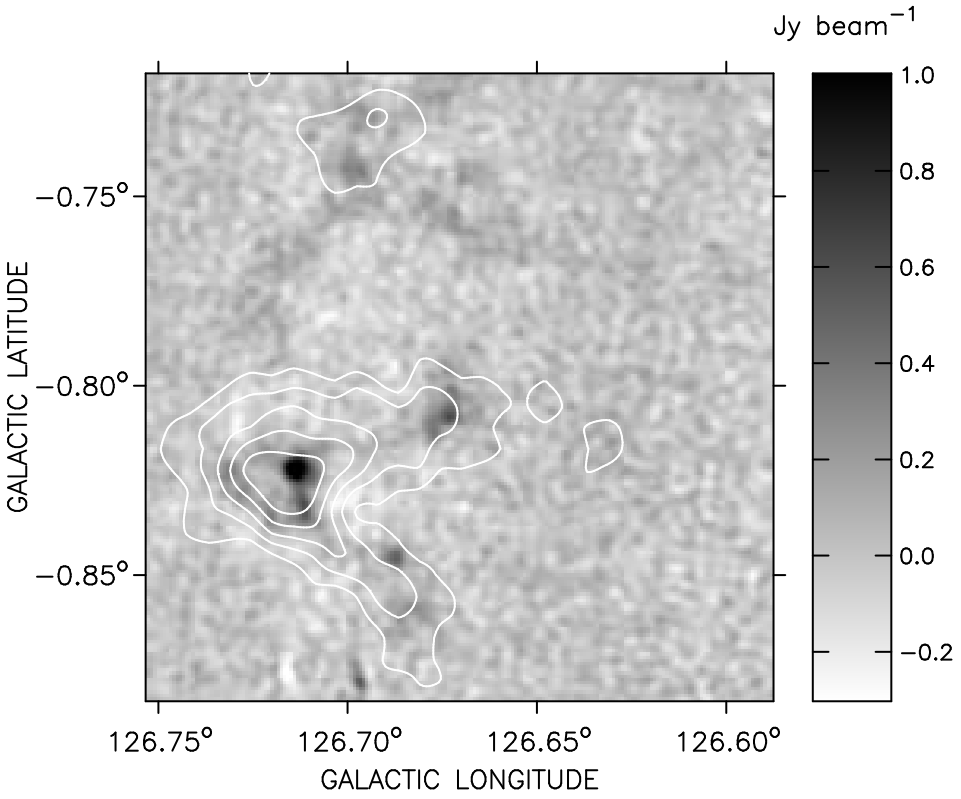

Figure 4.21 Close up view of KR 120 in 850 μm. The white contours correspond to integrated $C^{18}O$ brightness levels of 3, 4, 5, 6 and 7 K km s^{-1}.

4.5 Discussion

The halo H II regions investigated in this study each have one dominant 850 μm source located in the interface region between the H II region and the surrounding material. Beside the dominant source, there are not very many other sub-mm sources. This is in contrast to KR 140, where as many as 22 sub-mm sources where found (Kerton et al., 2001). Thus, it appears KR 7, KR 81 and KR 120 are not as populated with sub-mm sources as KR 140. The masses found in this study, 51, 27 and 21 $M_\odot$ fall within the range of masses from Kerton et al. (2001), $0.5 - 130$ $M_\odot$. Given the noise level in the sub-mm images and the distances, a 3σ source detection would correspond to a minimum mass sensitivity of $2 - 4$ $M_\odot$. Only 3 out of 22 sub-mm objects (14%)

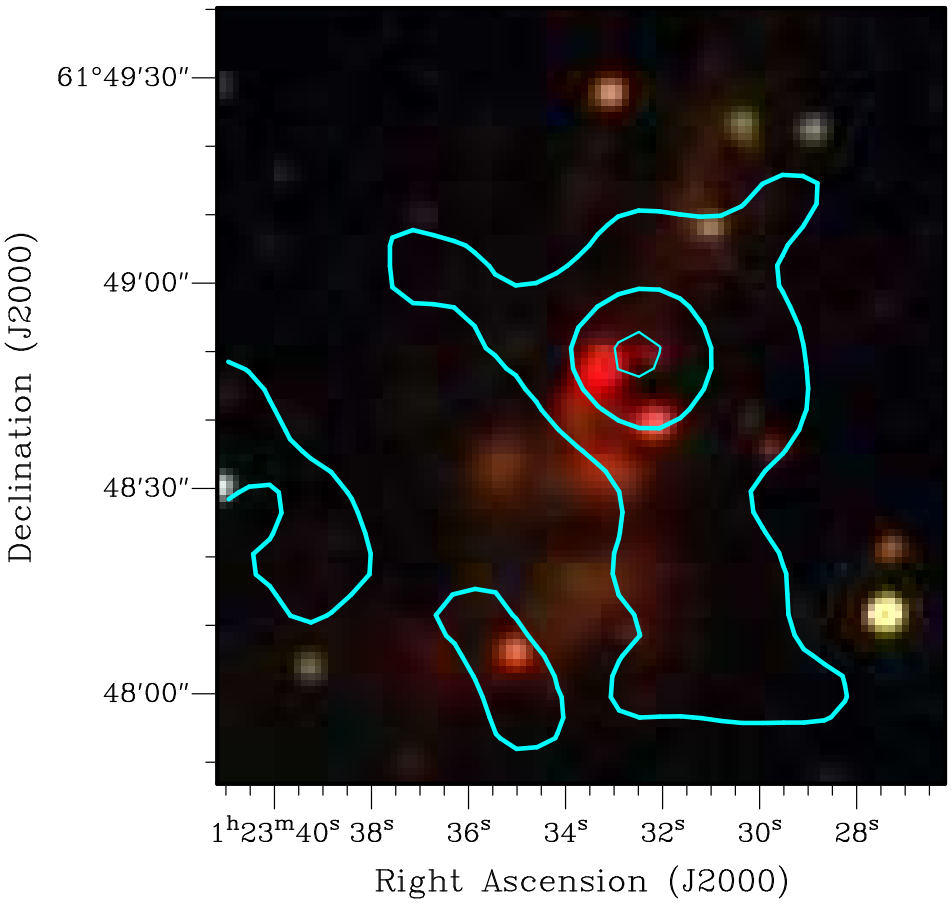

Figure 4.22 Close-up RGB composite of 2MASS J-band (Blue), H-band (Green) and K-band (Red) images of KR 120. The contours correspond to 850 μm brightness levels of 0.2, 0.8 and 1.4 Jy beam^{-1}.

in Kerton et al. (2001) has a mass < 2 M$_\odot$, so a large population of sub-mm sources is likely not missed in KR 7, KR 81 and KR 120. The sizes found, 0.6, 0.4 and 0.2 pc, fall within the range $0.2 - 0.7$ pc found in Kerton et al. (2001).

The respective masses for the surrounding molecular material is 3600 M$_\odot$ (KR 7), 1900 M$_\odot$ (KR 81) and 7600 M$_\odot$ (KR 120). Ballantyne et al. (2000) found that the molecular cloud surrounding KR 140 contained about 5000 M$_\odot$. Data from the ^{12}CO FCRAO Outer Galaxy Survey (OGS; Heyer et al., 1998) with a spectral resolution of

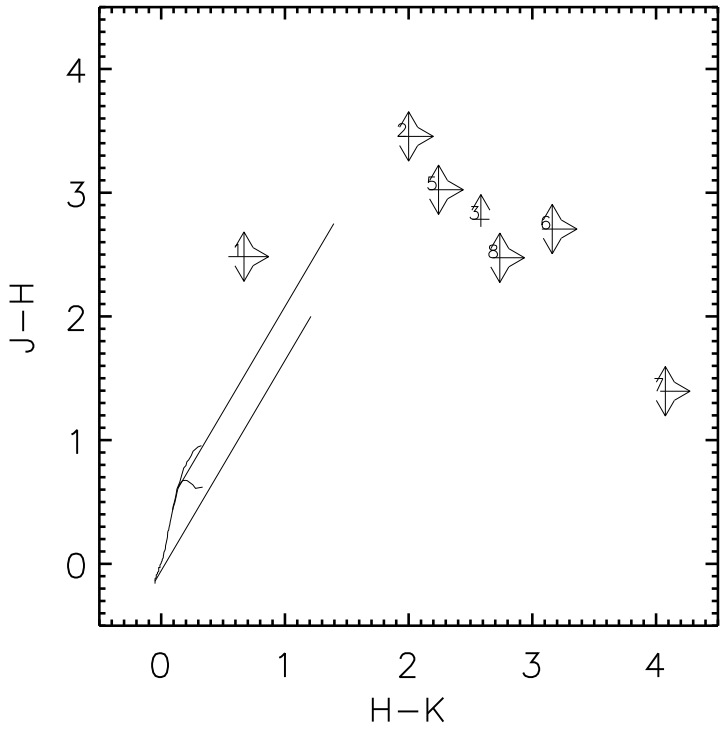

Figure 4.23 Color-color diagram for the 2MASS sources within a radius of 0.25′ of the KR 120 850 μm source.

0.98 km s^{-1} and an angular resolution of 46″ show that the molecular material seen around KR 120 and KR 140 is likely part of larger molecular clouds. The material around KR 7 and KR 81 does not show connections to larger molecular clouds. This makes at least two examples of massive stars forming in clouds with masses $< 10^4$ M$_\odot$, which is quite unexpected. Massive stars are expected to form in GMCs in the range $10^4 - 10^6$ M$_\odot$.

Moore et al. (2007) investigated the W3 GMC, a high-mass star-forming region located in the outer Galaxy with SCUBA. The result in Moore et al. (2007) in a list of 316 850 μm clumps. For this study, that list was searched based on position for sources to obtain a subset of sources that are located in the so-called high-density layer (HDL). This layer of the W3 GMC runs parallel to the W4 H II region and contains luminous,

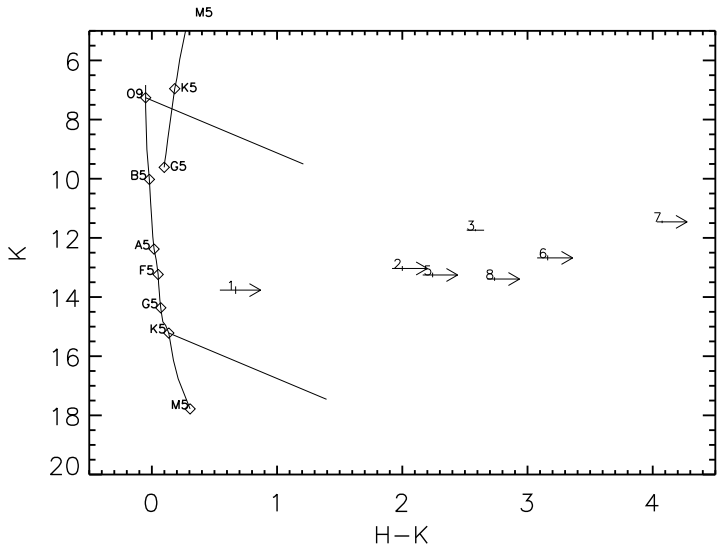

Figure 4.24 Color-magnitude diagram for the 2MASS sources within a radius of 0.25′ of the KR 120 850 μm source.

massive star-forming regions (W3 Main, W3 (OH) and AFGL 333) that are likely to be examples of triggered star formation. Within the HDL, 220 sub-mm sources were found. Using the same dust temperature assumption as above in Section 4.4 ($T_d = 20$ K) and a distance to W3 of 2.0 kpc, the peak mass column densities and sub-mm clump masses are computed. The peak mass column densities for the 220 HDL sub-mm sources range between 0.009 g cm^{-2} and 3.1 g cm^{-2}, with a median of 0.02 g cm^{-2} and an average of 0.07 g cm^{-2}. The values found for the KR objects in this study, $0.10 - 0.33$ g cm^{-2}, appear to land above both the median and the average of the peak mass column densities associated with the HDL. As the values in this study represent the maxima for their respective halo H II regions, it seems likely that the peak mass column densities associated with massive star-forming regions forming multiple massive stars in the HDL could have a range that overlaps the values for mass column densities associated with massive star-forming regions formed by a single ionizing late O-early B star. However, the maximum peak mass column density for the HDL is about an order of magnitude higher than those found in this study. The masses of the 220 sub-mm sources range

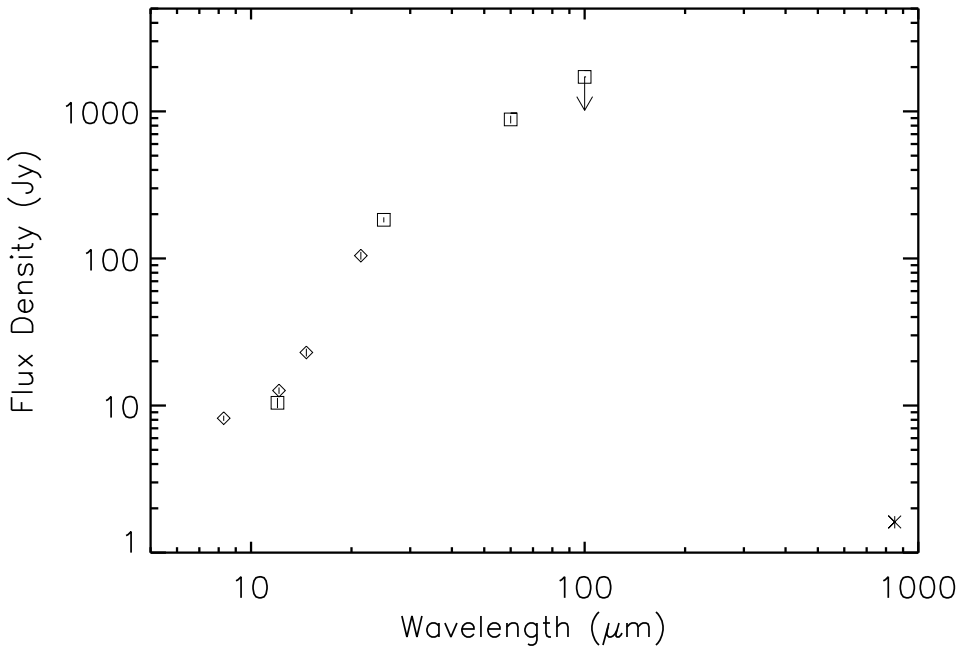

Figure 4.25 Spectral energy distribution for the KR 120 850 μm source.

between $7 - 4900$ $M_\odot$, with a median of 31 and an average of 123 $M_\odot$. The sub-mm masses found in this study fall within the range of masses and around the median of masses associated with the HDL, but the maximum masses found within the HDL are at least an order of magnitude higher than found in this study.

The peak mass column densities found in this study are comparable to the IM SFR peak mass column densities found in Section 2.5.2, and thus an order of magnitude less than the UCH II peak mass column densities from Section 2.6.2. However, the masses found are smaller by at least an order of magnitude compared to the IM SFR masses found using the BGPS catalog and roughly smaller by two orders of magnitude compared to UCH II regions. This could simply be an effect of the sub-mm sources in this study being smaller in angular extent compared to the BGPS sources. Given the large uncertainties in the mass column densities and masses coming from the large uncertainty in dust temperature and dust opacity, it is not clear if the difference in masses between

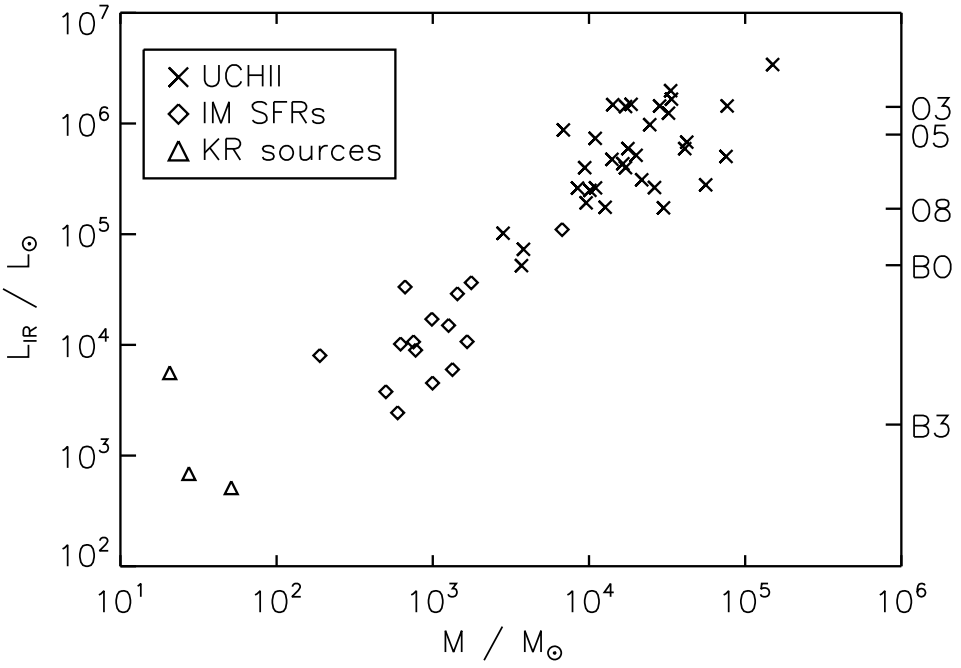

Figure 4.26 Luminosity versus associated mass. IM SFRs (15 objects) are diamonds. UCH II regions (33 objects) are crosses. The three KR sub-mm sources are triangles. The scale on the right is spectral type of a single class V star.

sub-mm in this study and IM SFRs found represents some real physical difference.

The method of Emerson (1988) was used to calculate the infrared luminosity ($L_{\rm IR}$) from the IRAS PSC values for the three sub-mm sources. Figure 4.26 adds these three data points to the left hand panel of Figure 2.26. Figure 4.26 now shows UCH II regions, IM SFRs and KR sub-mm sources as triangles. It still shows a correlation between luminosity and associated clump mass for IM SFRs, UCH II regions and KR sub-mm sources. The data are fit by $L \propto M^{1.02\pm0.06}$ which largely agrees with the value found in Section 2.7 and by Chini et al. (1987). This relationship probably holds holds over four orders of magnitude, another order of magnitude less than found in Section 2.7. This is significant because a constant ratio of luminosity to associated mass is what is expected if star formation follows the same Initial Mass Function (IMF) in all star forming regions

and that the star formation efficiency for converting gas into stars is the same over many orders of magnitude in associated mass.

KR 120 has been the subject of previous studies. Joncas et al. (1992) conducted a multiwavelength study of KR 120 in the optical, IR and radio, and found that KR 120 is an H II region of age $\sim 2 \times 10^5$ years that is still enshrouded in the parental cloud. Zavagno et al. (1994) discovered through spectroscopy a pre-main-sequence object (S 187Hα) near the *IRAS* 01202+6133 source. Salas et al. (1998) imaged the region near *IRAS* 01202+6133 in the NIR and discovered a curved molecular hydrogen outflow that extends over a region of 76′ (0.55 pc at 1.44 kpc) that is probably due to a jet from a solar mass YSO. Furthermore, the *MSX* source is listed as being associated with an OH maser, a bright signpost for a recently formed massive star (Argon et al., 2000). This presence of a pre-main-sequence object indicates that the investigated sub-mm clump is likely the site for ongoing star formation, something that agrees with the possible presence of an embedded cluster hinted at in Figures 4.22, 4.23 and 4.24.

4.6 Conclusions

Three halo H II regions have been investigated using SCUBA 850 μm observations and molecular line observations (^{12}CO, ^{13}CO and C^{18}O). They are found to each have one dominant 850 μm source, located in the interface region between the H II region and the surrounding molecular material. These three H II regions are less populated with sub-mm sources than the previously studied H II region KR 140. At the same location as the dominant 850 μm source, peaks are found in the integrated molecular maps, confirming these as locations of cold, dense material. Estimating the peak mass column density toward the sources results in values $0.1 - 0.3$ g cm^{-2}, comparable to the IM SFRs studied in Chapter 2. The masses found, 51, 27 and 21 M$_\odot$ fall within the

range of masses previously found for KR 140 by Kerton et al. (2001). The same is true for the sizes, 0.6, 0.4 and 0.2 pc, that fall within the range $0.2 - 0.7$ pc. Using 2MASS photometry, a possible embedded cluster of YSOs are found within the dominant sub-mm source of KR 120, consistent with earlier studies that found signatures of a jet from a pre-main-sequence object. This is likely a site for ongoing star formation. Candidates for embedded YSOs within the sub-mm sources are found for KR 7, while sources toward KR 81 can be explained as either foreground or background objects.

CHAPTER 5. SUMMARY AND FUTURE WORK

5.1 Summary

A sample of 50 intermediate-mass star-forming regions in the inner Galaxy has been identified and investigated for the first time through infrared and radio observations. They were found to share some basic properties. They have typical luminosities of $\sim 10^4$ $L_\odot$ and the photo dissociation regions that demarcate the IM SFRs have typical diameters of $\sim$ 1 pc. These properties are consistent with these objects being regions containing stars in the $2 - 8$ $M_\odot$ range with associated clusters of low-mass stars. IM SFRs do show some similarities with high-mass star-forming regions. On parsec-scales IM SFRs are typically associated with molecular clumps of mass $\sim 10^3$ $M_\odot$ and on larger scales they are found within GMCs with masses between $10^4 - 10^5$ $M_\odot$. The conclusion drawn is that massive star formation in GMCs in that mass range is not inevitable. IM SFRs are also distinct from regions of more massive star formation, forming in clumps with masses as low as $\sim 10^2$ $M_\odot$ and not being found in the most massive GMCs ($\geq 10^6$ $M_\odot$).

The IM SFRs, compared to a sample of UCH II regions taken from the literature, turn out typically have an order of magnitude less luminosity than UCH II regions. The molecular material associated with IM SFRs typically have an order of magnitude smaller peak mass column density and clump mass compared to UCH II regions. The lack of IM SFRs found with associated peak mass column densities > 0.5 g cm^{-2} supports the

idea that there is a threshold in mass column density above which only massive star formation occurs. A strong correlation between luminosity and associated molecular mass in star-forming regions is found to apply over three orders of magnitude encompassing both IM SFRs and UCH II regions.

For the first time, an investigation into the enormous H II region CTB 102 was carried out. Through a combination of new radio recombination line observations and available archival data, analysis shows that the filamentary structure surrounding the central region is physically associated with the central region. The first ever distance estimate for this H II region is provided, 4.3 kpc. The overall morphology and size of CTB 102 indicates that it is likely a large H II region combined with a wind-blown interstellar bubble/chimney structure, powerful enough to disrupt the interstellar medium and clear out a $\sim 100 - 130$ pc region. The size and structure of CTB 102 makes it comparable to the W4 superbubble in the Perseus arm, one of the largest H II regions in the Galaxy.

Three halo H II regions, KR 7, KR 81 and KR 120, have been investigated using SCUBA 850 μm observations and molecular line observations as possible sites of triggered star formation. They were found to each have one dominant 850 μm source, corresponding to cold, dense material, located in the interface region between the H II region and the surrounding molecular material. They were also found to be less populated with sub-mm sources than the previously studied H II region of similar size, KR 140. The peak mass column density toward the sub-mm sources were found to be $0.1 - 0.3$ g cm^{-2}, comparable to the IM SFRs studied in Chapter 2. The masses found, 51, 27 and 21 M$_\odot$ fall within the range of masses previously found for KR 140. The same is true for the sizes found, 0.6, 0.4 and 0.2 pc. A possible embedded cluster of young stellar objects are found within the dominant sub-mm source of KR 120, consistent with earlier studies

that found signatures of a jet from a pre-main-sequence object. This is likely a site for ongoing star formation. Candidates for embedded YSOs within the sub-mm sources are found for KR 7, while sources toward KR 81 can be explained as either foreground or background objects.

5.2 Future work

5.2.1 Intermediate-Mass Star-Forming Regions

Infrared luminosity can be a rather poor proxy for the mass of the most massive stars present. Cluster effects, an intrinsic luminosity range and the cover factor (how much of the radiation is being captured by the surroundings) all effect the observed infrared luminosity. Are the most massive stars formed really mid-B to early A stars? To address this, an infrared spectroscopy proposal has been submitted to use the multi-slit FLAMINGOS IR spectrometer at the NOAO Kitt Peak 4-m telescope to determine the spectral type of the most massive stars.

Another issue is, what is the young stellar content in IM SFRs? How large are the associated clusters? *Spitzer* images often lack point sources within the IM SFRs, likely due the sensitivity not being good enough to detect the point sources over the bright extended emission from the PDR. A *Chandra* proposal has been submitted to obtain X-ray observations of the young pre- or early-main-sequence stars that are luminous in X-rays (Wang et al., 2009). Coupled with deeper NIR photometry from UKIDSS and *Spitzer* imaging, cluster members can be identified and the stellar mass content measured.

To properly investigate if the threshold of 1 g cm^{-2} proposed by Krumholz & McKee (2008) is by itself a necessary and sufficient criterion for high-mass star formation, the

large uncertainty in the analysis of clump mass and column density stemming from the dust temperature needs to be addressed. High resolution observations with the *Herschel* SPIRE instrument at 250, 350 and 500 μm of these IM SFR associated molecular clumps would help nail down the dust temperature structure and thereby constrain the column densities and masses.

Are there really no objects in the lower right part of the left panel of Figure 2.26, i.e., objects with high associated mass but low luminosity? To check, a systematic search of the BGPS catalog for sources that have high dust-based mass would yield a subset of sources that can then be compared to near- and mid-IR images to ascertain the associated luminosity.

5.2.2 CTB 102

Filament 10 (Section 3.6.2) looks strikingly circular in the 1420 MHz continuum image. The rapid fall-off at the edge strongly suggests the region is ionization bound. Could this be an example of a completely unstudied Strömgren sphere? What is the type of ionizing star (or cluster of stars) at the center of the nebula, and is it consistent with a Strömgren sphere? To answer this question, recently obtained GLIMPSE360 images could determine what type of star is powering the nebula. GLIMPSE360 is the continuation of the GLIMPSE survey to cover the outer Galactic plane in the two shortest IRAC bands, 3.6 and 4.5 μm. Further investigation could possibly reveal triggered stars around the small nebula. Similarly, GLIMPSE360 could be used to determine what star or stars power the enormous H II region.

5.2.3 Star Formation around Halo H II regions

Using the Wide-field InfraRed Camera[1] (WIRCam) on the 3.6 meter Canada France Hawaii Telescope[2] (CFHT), deep J-, H- and K-band photometry has been obtained for the regions KR 7, KR 81, KR 120 and KR 140. WIRCam is an imaging instrument that consists of four 2048 × 2048 pixel detectors, and covers a $20' \times 20'$ field-of-view with a sampling of $0.3''$ per pixel.

The observations were planned with the goal of obtaining reliable photometry as deep as K-magnitude 18, an improvement of two magnitudes over 2MASS. This should be sufficient to detect the YSO content down to masses of ~ 1 $M_{\odot}$ in all three bands. The large WIRCam field-of-view should allow for sampling of the YSO population not only immediately surrounding the H II regions, but also in the surrounding molecular material (e.g., YSOs outside of the KR 140 H II region of influence were found in Kerton et al., 2008) beyond what is currently possible with 2MASS. Based on comparing 2MASS source counts in typical star-forming regions to UKIDSS catalog source counts where available, the number of sources found is expected to increase by at least a factor of 5 compared to 2MASS.

Thus, in the future, more sources with better photometry will be obtained for all four KR H II regions and their molecular surroundings. Each of the KR regions in this study has one significant sub-mm source worth investigating in depth with deep NIR photometry. For example, are there more than just two possibly embedded YSOs located near the center of the sub-mm source associated with KR 7? Does KR 81 really have no YSOs near the center of the sub-mm source (starless core), or is it a case of any possible YSOs there having too poor photometry in 2MASS? Is the most massive YSO in the

[1] http://www.cfht.hawaii.edu/Instruments/Imaging/WIRCam/
[2] http://www.cfht.hawaii.edu/

KR 120 cluster possibly more massive than the star powering the H II region? Furthermore, comparisons of YSO distributions could be made between the KR objects, and also between the YSOs located in the PDRs and the YSOs located in the surrounding molecular cloud. Is there a difference in mass or evolutionary stage? GLIMPSE360 will eventually cover these regions. That will allow for J, H, K, 3.6 and 4.5 μm photometry, which gives a better tool for distinguishing stars from YSOs.

There are also other fainter sub-mm clumps in the 850 μm images that were ignored in this study, but that could be explored in a future project for possible signs of star formation. The new instrument SCUBA-2 on JCMT, with its increased speed and sensitivity compared to SCUBA, will survey the Galactic plane and might detect a population of currently undetected sub-mm clumps around these halo H II regions.

5.3 Concluding remarks

The future of research into star-forming regions is looking very bright and data-rich. The future millimeter interferometer the Atacama Large Millimeter Array (ALMA), science ready in 2012 and having a $0.02''$ resolution, will allow for great advances in star formation research. For example, the structure of the coldest, densest material inside of an IM SFR or a sub-mm clump would be resolved. Current space telescopes like *Herschel* in the FIR/sub-mm and a future one like James Webb Space Telescope (JWST) in the near- to mid-IR would provide similar advancements in their wavelength regimes.

APPENDIX A. CODE USED TO ESTIMATE RRL PARAMETER UNCERTAINTIES

Description

This IDL script aims to take observed radio recombination lines, extract line parameters (specifically amplitude, center and line width) and the total uncertainties for those parameters. This script was made for dealing with radio recombination line observations using the Green Bank Telescope (GBT), so it is fairly specific. None the less, using the comments and changing certain numbers which are not input options, this script could be used to obtain line parameters and their total uncertainties for any line that has a single Gaussian shape.

The script imports the spectrum as two arrays, one containing the velocities (x-axis) and one the intensity values (y-axis). A Gaussian is fit to the noisy spectrum, the parameter values and the fit uncertainties of the parameter values are stored. The noise in the ingoing spectrum is characterized (in the region of no line) by the standard deviation in a normal distribution. A new normal distribution is generated, having the same standard deviation as the ingoing spectrum. This "new noise" is added to the Gaussian line profile obtained in the earlier fit. A *new* Gaussian line profile is fitted to the generated noisy spectrum, its parameters and fit uncertainties are stored. This is then repeated a desired number of times, each time with different noise of the same magnitude. Statistics on the arrays containing the stored parameters and stored fit uncertainties gives the to-

tal uncertainties. The standard deviations of the three generated fit parameters is taken as the uncertainty from the noise. The mean values of the generated fit uncertainties is taken as the uncertainty from the fit itself. These two contributions are squared, added together, and the square root then represents the total uncertainty (noise+fit) of the extracted line parameters. A summary of the parameters and uncertainties is printed to the screen and to a file.

The script contains commands to display the distributions of the fitted parameters and their fit uncertainties as histograms. To use these commands, the routine *plothist.pro* from The IDL Astronomy User's Library must be present on the computer used to run the script.

Necessary preparation

1. The ingoing files obviously need to be formatted so that IDL can read them.
2. The baseline of the ingoing spectrum needs to be 0 (intensity unit).
3. The number of elements in the ingoing spectrum files must be known, this is input to the routine.
4. The line parameters must be roughly known, since the fitting routine needs an input vector.
5. A region of the spectrum without line structure must be specified, so the noise can be properly characterized. That region is initially set to look at both sides of the line.

The code

```
PRO rrl,a,b,c,d,e
```

`a` is the velocity file 'vel.dat', the ' ' in the file name is needed.

`b` is the spectrum 'name.dat'.

`c` is the number of elements in the ingoing files.

`d` is the number of iterations.

`e` is the output file for the results, for example 'output.dat'.

Create double precision arrays of given size to put the velocity (vel) and spectrum (ave1, in antenna temperature) into.

```
vel=dblarr(c)
ave1=dblarr(c)
```

Open files for reading and put the data into the arrays.

```
openr,1,a
readf,1,vel
close,1
openr,1,b
readf,1,ave1
close,1
```

Account for the beam efficiency of the telescope, 0.92 for the GBT, and put the corrected spectrum into array ave.

```
ave=ave1/0.92
```

Create array containing the line free region for computing statistics, called totalstats.

```
totalstats=where((vel GT -160 and vel LT -110) OR (vel GT 10 and vel LT 110))
```

Compute 1 sigma noise for the region.

```
sigma=stddev(ave(totalstats))
```

Construct gaussian fit. A is the vector containing initial parameters [amplitude,center,width].

```
A=[max(ave),-60,10]
```

Perform the fit, B is now the vector containing the fit uncertainties of the fitted parameters, which will be put in A. The resulting fit is put into array yfit.

```
yfit=gaussfit(vel,ave,A,NTERMS=3,SIGMA=B)
```

Save the fitted parameters and uncertainties in arrays fitresult and uncertresult.

```
fitresult=A
uncertresult=B
```

Create storage arrays of size d.

```
amplitudes=dblarr(d)
velocities=dblarr(d)
widths=dblarr(d)
ampuncert=dblarr(d)
veluncert=dblarr(d)
widuncert=dblarr(d)
```

Start the loop.

```
FOR i=0,d-1 DO BEGIN
```

Create 1 by c array of randomly distributed numbers with mean 0 and standard deviation of 1.

```
random = randomn(seed,1,c,/double)
```

Scaling the random array down so that it matches the real noise level, so multiplied by the previously obtained sigma.

```
scaledrandom=sigma*random
```

Add the scaled random array to the yfit array, thereby generating a new spectrum.

```
generated=yfit+scaledrandom
```

Fit a gaussian to the generated spectrum, use the old array A as input.

```
fittogenerated=gaussfit(vel,generated,A,NTERMS=3,SIGMA=B)
```

Put the results from each fit into an element in the storage arrays.

```
amplitudes[i]=A[0]
velocities[i]=A[1]
widths[i]=A[2]
ampuncert[i]=B[0]
veluncert[i]=B[1]
widuncert[i]=B[2]
END
```

Extract results from the arrays and compute the statistics on all the fits, ignore any blank data by using /nan.

```
ampfits=moment(amplitudes,/nan)
```

```
velfits=moment(velocities,/nan)
widfits=moment(widths,/nan)
```

Calculate the standard deviation of the FWHM, not the Gaussian width.

```
fwhmsigma=SQRT(2*SQRT(ALOG(2))*widfits[1])
```

Plot histograms if desired, note that the FWHM histogram is plotted, not the Gaussian width.

```
plothist,amplitudes,bin=0.01
plothist,velocities,bin=0.1
plothist,2*SQRT(ALOG(2))*widths,bin=0.1
```

Measure of statistics on the collection of individual fit uncertainties.

```
ampunc=moment(ampuncert,/nan)
velunc=moment(veluncert,/nan)
widunc=moment(widuncert,/nan)
```

Plot histograms on the collection of fit uncertainties if desired, note that the FWHM uncertainty histogram is plotted, not the Gaussian width.

```
plothist,ampuncert,bin=0.000001
plothist,veluncert,bin=0.001
plothist,2*SQRT(ALOG(2))*widuncert,bin=0.01
```

Start printing the results to the screen.

```
print,'RESULT FROM INITIAL FIT TO ORIGINAL SPECTRUM (IN BRIGHTNESS TEMPERATURE)'
print,'Amplitude (mK):',fitresult[0]*1000
print,'Sigma (mK):',sigma*1000
```

```
print,'Velocity (km/s):',fitresult[1]
print,'FWHM (km/s):',2*SQRT(ALOG(2))*fitresult[2]

print,'UNCERTAINTY IN LINE PARAMETERS FROM DISTRIBUTION OF SIMULATED SPECTRA'
print,'NUMBER OF REPETITIONS:',d
```

Take the uncertainties to be the standard deviation of the distribution of line amplitudes from all the fits made.

```
print,'Amplitude uncertainty (mK):',SQRT(ampfits[1])*1000
print,'Velocity uncertainty (km/s):',SQRT(velfits[1])
print,'FWHM uncertainty (km/s):',fwhmsigma

print,'UNCERTAINTY IN LINE PARAMETERS FROM THE FIT UNCERTAINTIES THEMSELVES'
print,'Amplitude uncertainty (mK):',ampunc[0]*1000
print,'Velocity uncertainty (km/s):',velunc[0]
print,'FWHM uncertainty (km/s):',2*SQRT(ALOG(2))*widunc[0]
```

Calculate total uncertainties.

```
totalampuncert=SQRT(ampunc[0]^2+ampfits[1])
totalveluncert=SQRT(velunc[0]^2+velfits[1])
totalwiduncert=SQRT(widunc[0]^2+widfits[1])

print,'TOTAL UNCERTAINTY IN LINE PARAMETERS'
print,'Total amplitude uncertainty (mK):',totalampuncert*1000
print,'Total velocity uncertainty (km/s):',totalveluncert
print,'Total FWHM uncertainty (km/s):',2*SQRT(ALOG(2))*totalwiduncert
END
```

BIBLIOGRAPHY

Aguirre, J., et al. 2009, ApJ, submitted

Argon, A. L., Reid, M. J., & Menten, K. M. 2000, ApJS, 129, 159

Ballantyne, D. R., Kerton, C. R., & Martin, P. G. 2000, ApJ, 539, 283

Barnes, P. J., & Myers, P. C. 1993, Massive Stars: Their Lives in the Interstellar Medium, 35, 102

Basu, S., Johnstone, D. & Martin, P. G. 1999, ApJ, 516, 843

Benjamin, R. A., et al. 2003, PASP, 115, 953

Bessell, M. S., & Brett, J. M. 1988, PASP, 100, 1134

Bonatto, C., Santos, J. F. C., Jr., & Bica, E. 2006, A&A, 445, 567

Carey, S. J., et al. 2005, BAAS, 37, 1252

Castor, J., McCray, R. & Weaver, R., 1975, ApJ, 200, L107

Chapin, E. L., et al. 2008, ApJ, 681, 428

Chini, R., Kruegel, E., & Wargau, W. 1987, A&A, 181, 378

Condon, J. J., Cotton, W. D., Greisen, E. W., Yin, Q. F., Perley, R. A., Taylor, G. B., & Broderick, J. J. 1998, AJ, 115, 1693

Clemens, D. P. 1985, ApJ, 295, 422

Deharveng, L., Zavagno, A., & Caplan, J. 2005, A&A, 433, 565

Diaz-Miller, R. I., Franco, J., & Shore, S. N. 1998, ApJ, 501, 192

Di Francesco, J., Johnstone, D., Kirk, H., MacKenzie, T., & Ledwosinska, E. 2008, ApJS, 175, 277

Eisenhauer, F., et al. 2005, ApJ, 628, 246

Elmegreen, B. G. 1998, Origins, 148, 150

Emerson, J. P. 1988, NATO ASIC Proc. 241: Formation and Evolution of Low Mass Stars, 193

Engelbracht, C. W., et al. 2007, PASP, 119, 994

Fazio, G. G., et al. 2004, ApJS, 154, 10

Fich, M., & Terebey, S. 1996, ApJ, 472, 624

Foster, T. & MacWilliams, J. 2006, ApJ, 644, 214

Foster, T., & Routledge, D. 2003, ApJ, 598, 1005

Giard, M., Bernard, J. P., Lacombe, F., Normand, P., & Rouan, D. 1994, A&A, 291, 239

Heyer, M. H., Brunt, C., Snell, R. L., Howe, J. E., Schloerb, F. P., & Carpenter, J. M. 1998, ApJS, 115, 241

Higgs, L. A., & Tapping, K. F. 2000, AJ, 120, 2471

Hughes, V. A., & MacLeod, G. C. 1989, AJ, 97, 786

Jackson, J. M., et al. 2006, ApJS, 163, 145

Joncas, G., Durand, D., & Roger, R. S. 1992, ApJ, 387, 591

Kallas, E. & Reich, W. 1980, A&AS, 42, 227

Kauffmann, J., Bertoldi, F., Bourke, T. L., Evans, N. J., II, & Lee, C. W. 2008, A&A, 487, 993

Kerton, C. R. 2000, Ph.D. Thesis

Kerton, C. R. 2002, AJ, 124, 3449

Kerton, C. R. 2006, MNRAS, 373, 1203

Kerton, C. R., Arvidsson, K., Knee, L. B. G., & Brunt, C. 2008, MNRAS, 385, 995

Kerton, C. R., Ballantyne, D. R., & Martin, P. G. 1999, AJ, 117, 2485

Kerton, C. R., Martin, P. G., Johnstone, D., & Ballantyne, D. R. 2001, ApJ, 552, 601

Koornneef, J. 1983, A&A, 128, 84

Krumholz, M. R., & McKee, C. F. 2005, ApJ, 630, 250

Krumholz, M. R., & McKee, C. F. 2008, Nature, 451, 1082

Kwok, S. 2007, Physics and Chemistry of the Interstellar Medium (University Science Books)

Lada, C. J., & Lada, E. A. 2003, ARA&A, 41, 57

Lahulla, J. F. 1985, A&AS, 61, 537

Lawrence, A., et al. 2007, MNRAS, 379, 1599

Levine, E. S., Heiles, C., & Blitz, L. 2008, ApJ, 679, 1288

Lequeux, J. 2005, The interstellar medium, Translation from the French language edition of: Le Milieu Interstellaire by James Lequeux, EDP Sciences, 2003 Edited by J. Lequeux. Astronomy and astrophysics library, Berlin: Springer, 2005

Lockman, F. J. 1989, ApJS, 71, 469

McKee, C. F., & Ostriker, E. C. 2007, ARA&A, 45, 565

Martos, M., Hernandez, X., Yáñez, M., Moreno, E., & Pichardo B. 2004, MNRAS, 350, L47

Moore, T. J. T., Bretherton, D. E., Fujiyoshi, T., Ridge, N. A., Allsopp, J., Hoare, M. G., Lumsden, S. L., & Richer, J. S. 2007, MNRAS, 379, 663

Normandeau, M., Taylor, A. R. & Dewdney, P. E. 1996, Nature, 380, 687

Panagia, N. 1973, AJ, 78, 929

Price, S. D., Egan, M. P., Carey, S. J., Mizuno, D. R., & Kuchar, T. A. 2001, AJ, 121, 2819

Rathborne, J. M., Johnson, A. M., Jackson, J. M., Shah, R. Y., & Simon, R. 2009, ApJS, 182, 131

Reach, W. T., et al. 2005, PASP, 117, 978

Rieke, G. H., & Lebofsky, M. J. 1985, ApJ, 288, 618

Rieke, G. H., et al. 2004, ApJS, 154, 25

Roberts, W. W. Jr. 1972, ApJ, 173, 259

Robitaille, T. P., Whitney, B. A., Indebetouw, R., Wood, K., & Denzmore, P. 2006, ApJS, 167, 256

Rohlfs, K., & Wilson, T. L. 2004, Tools of Radio Astronomy (4th ed.; New York: Springer)

Roman-Duval, J., Jackson, J. M., Heyer, M., Johnson, A., Rathborne, J., Shah, R., & Simon, R. 2009, ApJ, 699, 1153

Rosolowsky, E., et al. 2010, ApJS, 188, 123

Rudolph, A. L., Brand, J., de Geus, E. J., & Wouterloot, J. G. A. 1996, ApJ, 458, 653

Russeil, D., Adami, C., & Georgelin, Y. M. 2007, A&A, 470, 161

Salas, L., Cruz-Gonzalez, I., & Porras, A. 1998, ApJ, 500, 853

Schaerer, D., & de Koter, A. 1997, A&A, 322, 598

Schaller, G., Schaerer, D., Meynet, G. & Maeder, A. 1992, A&AS, 96, 269

Sharpless, S. 1959, ApJS, 4, 257

Shu, F. H., Adams, F. C., & Lizano, S. 1987, ARA&A, 25, 23

Simon, R., Jackson, J. M., Clemens, D. P., Bania, T. M., & Heyer, M. H. 2001, ApJ, 551, 747

Simon, R., Rathborne, J. M., Shah, R. Y., Jackson, J. M., & Chambers, E. T. 2006, ApJ, 653, 1325

Skrutskie, M. F., et al. 2006, AJ, 131, 1163

Taylor, A. R., Gibson, S. J., Peracaula, M., Martin, P. G., Landecker, T. L., Brunt, C. M., Dewdney, P. E., Dougherty, S. M., Gray, A. D., Higgs, L. A., Kerton, C. R., Knee, L. B. G., Kothes, R., Purton, C. R., Uyaniker, B., Wallace, B. J., Willis, A. G., & Durand, D. 2003, AJ, 125, 3145

Tenorio-Tagle, G. 1982, in Regions of Recent Star Formation, ed. R. S. Roger & P. E. Dewdney (Dordrecht: Reidel), 1

Vacca, W. D., Garmany, C. D. & Shull, J. M. 1996, ApJ, 460, 914

Walker, H. J., Volk, K., Wainscoat, R. J., Schwartz, D. E., & Cohen, M. 1989, AJ, 98, 2163

Wang, J., Feigelson, E. D., Townsley, L. K., Román-Zúñiga, C. G., Lada, E., & Garmire, G. 2009, ApJ, 696, 47

Warren, S. J., et al. 2007, arXiv:astro-ph/0703037

Weintraub, D. A. 1990, ApJS, 74, 575

Whitney, B. A. 2005, Nature, 437, 37

Wilson, R. W. & Bolton, J. G., 1960, PASP, 72, 331

Wood, D. O. S., & Churchwell, E. 1989a, ApJS, 69, 831

Wood, D. O. S., & Churchwell, E. 1989b, ApJ, 340, 265

Zavagno, A., Deharveng, L., & Caplan, J. 1994, A&A, 281, 491

Zinnecker, H. & Yorke, H. W. 2007, ARA&A, 45, 481